


2018

Study on Electrolyte-gated Graphene Nanoelectronic Biosensors for Biomarker Detection

Jianbo Sun

Follow this and additional works at: <https://researchrepository.wvu.edu/etd>

 Part of the [Bioelectrical and Neuroengineering Commons](#), and the [Electrical and Computer Engineering Commons](#)

Recommended Citation

Sun, Jianbo, "Study on Electrolyte-gated Graphene Nanoelectronic Biosensors for Biomarker Detection" (2018). *Graduate Theses, Dissertations, and Problem Reports*. 6741.
<https://researchrepository.wvu.edu/etd/6741>

This Dissertation is protected by copyright and/or related rights. It has been brought to you by the The Research Repository @ WVU with permission from the rights-holder(s). You are free to use this Dissertation in any way that is permitted by the copyright and related rights legislation that applies to your use. For other uses you must obtain permission from the rights-holder(s) directly, unless additional rights are indicated by a Creative Commons license in the record and/ or on the work itself. This Dissertation has been accepted for inclusion in WVU Graduate Theses, Dissertations, and Problem Reports collection by an authorized administrator of The Research Repository @ WVU. For more information, please contact researchrepository@mail.wvu.edu.

Study on Electrolyte-gated Graphene Nanoelectronic Biosensors for Biomarker Detection

Jianbo Sun

Dissertation submitted to
the Statler College of Engineering and Mineral Resources
at West Virginia University
in partial fulfillment of the requirements for the degree of
Doctor of Philosophy in
Electrical Engineering

Yuxin Liu, PhD, Chair
Thirimachos Bourlai, PhD
Jeremy M. Dawson, PhD
Harry O. Finklea, PhD
Larry A. Hornak, PhD

Lane Department of Computer Science and Electrical Engineering
Morgantown, West Virginia, United States of America
2018

Keywords: electrolyte-gated field effect transistor, graphene, biosensors, biomarker detection

Copyright 2018 Jianbo Sun

Abstract

Study on Electrolyte-gated Graphene Biosensors for Biomarker Detection

Jianbo Sun

Biosensors are called upon to provide valuable benefits for human society in vital fields such as disease diagnosis, food inspection, environment monitoring, etc. Among the various biosensor architectures, the field effect transistor (FET) biosensors are promising as the next generation nanoelectronic biosensors, particularly attractive for point-of-care biomedical applications. The FET biosensors typically operate by measuring the conductance change of the semiconducting channel induced by the adsorption of the target biomolecules on it. The superior properties of graphene, including the unique electronic characteristics, facile functionalization and good biocompatibility, etc., make it an ideal building block for the FET biosensors. In this dissertation, we present studies on the electrolyte-gated graphene field effect transistor (EGGFET) biosensor and its application for the label-free detection of biomarkers.

Poly(methyl methacrylate) (PMMA) residues have long been a critical challenge for the transfer of the chemical vapor deposited (CVD) graphene, which is critical to obtain reliable devices. To address this issue, we first studied the degradation of the PMMA residues upon thermal annealing using Raman spectroscopy. An electrolytic cleaning method is shown to be effective to remove these post-annealing residues, resulting in a clean, residue-free graphene surface.

The performance of the EGGFET biosensor is demonstrated by the successful detection of human immunoglobulin G (IgG) using IgG-aptamer as the bioreceptor. The gate voltage with the minimum conductivity (V_{Dirac}) in the transfer curve of the EGGFET biosensor is used for the quantitative measurement of IgG concentration. In EGGFET biosensors, the graphene channels are directly exposed to the electrolytes, of which the composition, concentration and pH may vary during the testing. The response of the EGGFET biosensors is found to be susceptible to these variations which might lead to high uncertainty or even false results. We present an EGGFET immunoassay which allows well regulation over the matrix effect. The performance is demonstrated by the detection of human IgG from serum. The detection range of the EGGFET immunoassay for IgG detection is estimated to be around 2-50 nM with a coefficient of variation (CV) of less than 20%. The limit of detection (LOD) is around 0.7 nM.

Different from the metal-oxide-semiconductor field effect transistors (MOSFET), the gate voltage is applied on the electrolyte and the electrical double layer (EDL) at the electrolyte-graphene interface serves as the gate dielectric in EGGFET. We studied the capacitance behavior of the electrolyte-graphene interface; the results suggest that the electrolyte-graphene interface exhibits a complex constant phase element (CPE) behavior ($\frac{1}{Z} = Q_0(j\omega)^\alpha$) with both Q_0 and α varying as functions of the gate voltage. The EDL capacitance and the quantum capacitance are determined which allows us to extract the carrier density and mobility in graphene. This study give insight into the device physics of the EGGFET biosensor and is instructive for the design of the EGGFET biosensors on the device level.

Acknowledgement

I would like to express my sincere gratitude to my advisor, Dr. Yuxin Liu, for her patient guidance, intellectual inspiration, and amiable encouragement throughout my time as his student. I am extremely lucky to be given the opportunity to join her group and pursue my PhD degree under her mentorship. As an advisor, she showed me the path and prospects of being a scientific researcher with constant passion, curiosity and dedication, which motivates me to complete this phase of my professional development.

I gratefully acknowledge the members of my advisory committee: Dr. Thirimacho Bourlai, Dr. Jeremy Dawson, Dr. Harry O. Finklea and Dr. Larry A. Hornak, for their guidance on my research work and constructive feedback on this dissertation. Special thanks goes to Dr. Harry O. Finklea, for sharing with me his expertise in scientific research and the valuable suggestions for my research work.

I owe a great debt of gratitude to my family for their consistent support and encouragement throughout my PhD study in USA. Their generous love is the source of power for me to persist on my study and life far away from home. I could not imagine the fulfillment of this dissertation without their support.

Last but not the least, I am very thankful to my labmates: Dr. Xiang Li, Veronica Betancur Calle and Peng Zhang. I am also grateful to my friends, Peng Zheng, Xiaorui Tong, Dr. Zhengjun Wang, etc., in WVU for mutual support on academic practice and daily life.

Sincerely,

Jianbo Sun

April 2018

Table of Contents

Acknowledgement	iii
Table of Contents	iv
List of Figures.....	viii
List of Tables	xvi
Chapter 1. Dissertation overview	1
1.1. Background and Motivations	1
1.2. Objectives	3
1.3. Significance and novelty.....	5
1.4. Structure of the dissertation	6
Chapter 2. Literature Review	7
2.1. Graphene: properties, synthesis and functionalization	7
2.2. Development of graphene-based field effect transistor biosensors	12
2.2.1. The detecting targets of GFET biosensors.....	12
2.2.2. The type of graphene used in GFET biosensors	15
2.2.3. Efforts to improve the performance of the EGGFET biosensors	16
2.3. Comments	18
Chapter 3. Fabrication of the EGGFET biosensor.....	20
3.1. Structure of the Devices	20
3.2. Fabrication of the devices	20

3.2.1. Graphene transfer and electrolytic cleaning	20
3.2.2. Fabrication of the electrodes and the graphene channels.....	23
3.2.3. Functionalization of the graphene channel for IgG detection.....	25
Chapter 4. Characterization and Electrolytic Cleaning of PMMA Residues	27
4.1. Introduction.....	27
4.2. Experiments	30
4.3. Degradation of PMMA residue upon thermal annealing	30
4.4. Electrolytic cleaning of the post-annealing residues	34
4.5. Impact of PMMA residue removal on the transport properties of graphene	40
4.6. Conclusion	42
Chapter 5. Detection of IgG using EGGFET biosensor	44
5.1. Introduction.....	44
5.2. Experiments	46
5.3. Detection of IgG using EGGFET biosensor	48
5.4. Selectivity of the EGGFET biosensor.....	51
5.5. Conclusion	51
Chapter 6. Matrix Effect Study and Immunoassay Detection Using EGGFET biosensor ..	53
6.1. Introduction.....	53
6.2. Experiments	55
6.2.1. Design of the EGGFET immunoassay.....	55

6.2.2. Electrical measurement	56
6.3. Matrix effect on the EGGFET biosensor	57
6.3.1. Matrix effect on the V_{Dirac} of the EGGFET biosensors.....	57
6.3.2. Matrix effect on the potential of the gate electrode	60
6.3.3. Matrix effect on the sensitivity of the EGGFET biosensors.....	62
6.4. EGGFET immunoassay	64
6.4.1. Standard Operation Protocol of the EGGFET immunoassay	64
6.4.2. Spike-and-recovery test	65
6.5. Conclusion	72
Chapter 7. Capacitance Behavior of the Electrolyte-graphene Interface and the Carrier Statistics in Graphene.....	73
7.1. Introduction.....	73
7.1.1. Interfacial capacitance at the electrolyte-graphene interface.....	73
7.1.2. Carrier statistics in the graphene channel	76
7.2. Experiments	77
7.2.1. EIS measurement	77
7.2.2. Transfer curve measurement and C-V profiling	79
7.3. Capacitance behavior of the electrolyte-graphene interface.....	81
7.4. Determination of C_{EDL} and C_Q	86
7.5. Carrier mobility in graphene.....	92

7.6. Conclusion	98
Chapter 8. Conclusion and Outlook.....	100
Appendix.....	105
Appendix 1. Characterization of the functionalization of graphene	105
Appendix.2 Determination of the Dirac Voltage	107
Appendix 3. Optimization of the operation parameters	109
Appendix 4. Determination of the detection range	111
Determination of LOD	111
Detection range	113
Appendix 5 Quantum capacitance of graphene	115
BIBLIOGRAPHY	119

List of Figures

Figure 2.1 Lattice structure and energy dispersion of graphene. (a) the honeycomb lattice structure, (b) the Brillouin zone and (c) electronic dispersion of graphene with zoom in of the energy bands close to one of the Dirac points. (Reprinted from [36]).....	7
Figure 2.2 The ambipolar electrical field effect of graphene with schematics showing the band filling structure (Reprinted from [39]).....	8
Figure 2.3 The techniques for the synthesis of graphene with respect to their quality and price for mass production. Reprinted from [75].	11
Figure 3.1 Basic structure of the EGGFET biosensor	20
Figure 3.2 Schematic of the transfer process of CVD graphene and the experimental setup for the electrolytic cleaning. (Reprinted from [65])	21
Figure 3.3 XPS spectrum of the as-transferred graphene	22
Figure 3.4 Schematics of the fabrication process of the gate/source/drain electrodes and the patterning of the graphene channel.	23
Figure 3.5 Schematic diagram (a) and experimental setup (b) for the fabrication of the Ag/AgCl pseudo-reference electrode.	24
Figure 3.6 Schematics for the functionalization of the graphene channel for IgG detection. (Reprinted from [177]).....	25
Figure 4.1 The samples for the study of the PMMA residues and the electrolytic cleaning. The red dashed box indicates the coverage of the transferred graphene.....	30
Figure 4.2 Evolution of the PMMA residue as a function of annealing temperature. Raman Spectra (black curves) of the as-transferred graphene after annealing in N ₂ atmosphere for 1 h at 100 °C,	

150 °C, 200 °C, 300 °C, and 500 °C. The blue and red fitting curves are attributed to the G peak of graphene and new peak at 1590 cm⁻¹, respectively. (Reprinted from [65]) 31

Figure 4.3 Raman spectra of the as-transferred graphene after annealing in a N₂ atmosphere at 150 °C for 1 h, 2 h, 5 h, and 10 h, respectively. The blue and red fitting curves are attributed to the G peak of graphene and new peak at 1590 cm⁻¹, respectively. (Reprinted from [65])..... 32

Figure 4.4 Infrared spectra of the PMMA char. The inset shows the elimination of the methoxycarbonyl side chains in PMMA and the formation of the conjugated systems. Reprinted form [148]. 33

Figure 4.5 Raman spectroscopy study of the electrolytic cleaning at different reduction voltages. a) Raman spectra and b) intensity at 1480 cm⁻¹ of graphene that is 1) as-transferred, 2) after annealing in N₂ atmosphere at 250 °C for 3 h and after electrolytic cleaning at 3) -1 V, 4) -3 V and 5) -5 V vs Ag/AgCl in 0.5 M sulfuric acid for 1 h. (Reprinted from [65])..... 35

Figure 4.6 Raman spectroscopy study of the electrolytic cleaning as a functional of time. a) Raman spectra and b) intensity at 1480 cm⁻¹ of graphene that is 1) as transferred, 2) after annealing in N₂ atmosphere at 250 °C for 3 h and after electrolytic cleaning at -5 V vs Ag/AgCl in 0.5 M sulfuric acid for 3) 10 min, 4) 20 min and 5) 30 min. (Reprinted from [65])..... 36

Figure 4.7 Raman mapping of the graphene that is a) as transferred, b) after thermal annealing in N₂ atmosphere at 250 °C for 3 h and c) after electrolytic cleaning at -5 V vs Ag/AgCl in 0.5 M sulfuric acid for 30 min. (Reprinted from [65])..... 37

Figure 4.8 Histogram of G peak position, 2D peak position and I_{2D}/I_G of graphene that is a,b,c) as-transferred, d,e,f) after annealing in N₂ atmosphere at 250 °C for 3 hours and g,h,i) after electrolytic cleaning at -5 V vs Ag/AgCl in 0.5 M sulfuric acid for 3 hours. (Reprinted from [65]) 38

Figure 4.9 Characterization of thermal removal of the PMMA residues and electrolytic cleaning of the post-annealing residues. Representative AFM images of the graphene that is a) as transferred, b) after annealing in N₂ atmosphere at 250 °C for 3 h, and c) after electrolytic cleaning at -5 V vs Ag/AgCl in 0.5 M sulfuric acid for 30 min. The corresponding height profiles along the blue dashed line in the AFM images are shown in the bottom panel. The number in the left bottom of each image corresponds to the RMS roughness. (Reprinted from [65])..... 39

Figure 4.10 (a) Representative transfer curves, (b) Dirac voltage distribution, and (c) electron and hole mobilities derived of the graphene based SGFET that is as-transferred, after annealing in a N₂ atmosphere at 250 °C for 3 h and after electrolytic cleaning at -5 V versus Ag/AgCl in 0.5M sulfuric acid for 30 min. The error bars correspond to the standard error in (b). Reprinted from [65]..... 41

Figure 5.1 Operation principle of the EGGFET biosensor for IgG detection. (a) the modulation of the Fermi level in the graphene channel upon the adsorption of IgG molecules. (b) the negative shift of the transfer curve upon the adsorption of the IgG molecules. (Reprinted from [177]).... 45

Figure 5.2 Device and experimental setup for IgG detection. (a) The EGGFET biosensor integrated with a standard Ag/AgCl reference electrode and a PDMS well for sample containing. (b) The enlarged view of the graphene channel. (c) The schematic diagram of the circuit connection for the detection of IgG using EGGFET biosensor. 47

Figure 5.3 The responses of an EGGFET immunosensor to IgG. a) The continuous shifts of the transfer curves of the EGGEFT immunosensor upon the addition of IgG with different concentrations (0, 0.1, 0.5, 1.0, 5.0, 10, 50, 100, 500 nM). The transfer curves are stacked vertically with offsets of 0.1 μ A with the arrow indicating the increasing of IgG concentrations. b) ΔV_{Dirac}

with respect to the concentrations of IgG. The uncertainties of the fitting parameters indicate the standard errors of the estimates for the fitting. (Reprinted from [177]). 48

Figure 5.4 The response of the EGGFET biosensor to IgG and its fitting using the full Hill equation. 49

Figure 5.5 The real-time measurement of IgG using the EGGFET immunosensor. **(a)** The change of I_d upon successive addition of IgG with increasing concentrations from 0.1 nM to 500 nM. **(b)** ΔI_d with respect to the concentrations of IgG. The uncertainties of the fitting parameters indicate the standard errors of the estimates for the fitting. (Reprinted from [177]). 50

Figure 5.6 The selectivity of the EGGFET immunosensor for IgG detection. **(a)** Responses of the EGGFET immunosensor to the successive addition of IgA, IgM and IgG. **(b)** ΔI_d of the EGGFET immunosensor as responses to IgA, IgM and IgG. (Reprinted from [177]). 51

Figure 6.1 EGGFET immunoassay chip. **(a)** The prototype of the EGGFET immunoassay chip with the sample delivery channels filled with red food dye. The numbers indicate the 7 immunosensor sets with their function assignment as specified on the right. **(b)** An enlarged view of the EGGFET immunosensor set that was fabricated on SiO_2/Si substrate for the visualization of graphene (as indicated by the white dashed frames). The sample delivery channel is indicated by the brown dashed line. (Reprinted from [177]). 56

Figure 6.2 The V_{Dirac} of the EGGFET biosensors in **(a)** different electrolytes (all concentrations are 1 M except for Na_2SO_4 , K_2SO_4 and H_2SO_4 , which are 0.5 M); **(b)** mixture of KCl (1 M) and NaCl (1 M) with different mixing ratios (horizontal axis); **(c)** NaCl and KCl solution with different ionic strength and **(d)** KCl solution (1 M) that was titrated with different pH. The schematics in **(d)** show the possible orientation of the H_3O^+ and OH^- on the graphene. The error bars indicate the

standard deviation of the measured results of the five parallel channels. (Reprinted from [177]).

..... 58

Figure 6.3 The transfer curves of the EGGFET in KCl with different concentrations 60

Figure 6.4 The impact of the gate electrode potential on EGGFET biosensors. (a) The potential distribution in EGGFET biosensors. (b) The V_{Dirac} of the EGGFET biosensors with Ag/AgCl pseudo-reference electrode as the gate in different PBS diluents and the OCP between the Ag/AgCl pseudo-reference electrode and the standard Ag/AgCl reference electrode. The error bars indicate the standard deviation of the measurement results of the five parallel channels. (Reprinted from [177])..... 62

Figure 6.5 The impact of the ionic strength on the sensitivity of an EGGFET biosensor. (a) The response of the EGGFET biosensor to IgG under different diluents; (b) The maximum response ($\Delta V_{Diracmax}$) of the EGGFET biosensor in different PBS diluents and the corresponding Debye length. The error bars indicate the standard errors of the estimates for the fitting. (Reprinted from [177])..... 63

Figure 6.6 Standard operation protocol of the EGGFET immunoassay for IgG measurement. (Reprinted from [177])..... 64

Figure 6.7 Evaluation of the EGGFET immunoassay. (a) The spike-and-recovery test of the EGGFET immunoassay for IgG detection. The error bars refer to the standard deviations of measurement results of the five parallel channels. (b) The linearity-of-dilution assessment of the EGGFET immunoassay. 66

Figure 7.1 The device and the schematic diagram of the experimental setup for EIS measurement.

a) A picture of the graphene electrode for EIS measurement; b) The zoom-in view of the graphene

electrode as marked by the red dashed box in a); c) The cross-section schematic (not scaled) of the graphene electrode and the EIS measurement setup.	78
Figure 7.2 The device and the schematic diagram of the experimental setup for transfer curve measurement and C-V profiling. a) A picture of the graphene electrode for EIS measurement; b) The zoom-in view of the graphene electrode as marked by the red dashed box in a); c) The cross-section schematic (not scaled) of the graphene electrode and the EIS measurement setup.	80
Figure 7.3 Representative Bode plot of the graphene electrode and the fitting curve using the Randles circuit shown in the inset of (b).	81
Figure 7.4 Fitting results using the Randles circuit model.	82
Figure 7.5 A representative plot showing $\log(-Z'')$ with respect to $\log(f)$. The inset shows the Rs-CPE circuit model.	83
Figure 7.6 Fitting results using the Rs-CPE circuit model as a function of the gate voltage	84
Figure 7.7 Schematic diagram showing the impact of the imperfection sites on the capacitance behavior of the electrolyte-graphene interface.	85
Figure 7.8 A representative plot showing $\log(-Z'')$ with respect to $\log(f)$ at different gate voltages.	86
Figure 7.9 The C-V profiling of the EGGFET at different frequencies.	87
Figure 7.10 Fitting results based on the C-V profiling.	88
Figure 7.11 Fitting results based on the model as shown in the inset.	89
Figure 7.12 Fitting results based on the model 2 which includes a compensating capacitance. .	90
Figure 7.13 Transmission line measurement of the sheet conductivity of graphene and the access resistance. (a) The device for TLM study. (b) The transfer curves of each channel with different	

aspect ratio. (c). The linear regression analysis of the resistance measurement with respect to the aspect ratio. (d) The extracted sheet resistivity of graphene and the access resistance.	94
Figure 7.14 The transfer curve of the EGGFET and the extracted sheet conductivity of the graphene channel	95
Figure 7.15 The extracted carrier density based on the fitting results obtained in Figure 7.12...	96
Figure 7.16 The extracted carrier mobility with respect to the carrier density.	96
Figure 7.17 Carrier mobility in graphene reported in previous reports. (a) The carrier mobility extracted based on the back-gated graphene FET structure [224]. (b) The measurement results based on Hall effect [223]. (c) The measurement results based on EGGFET structure and theoretically predicted carrier density [165].	97
Figure 8.1 Computed electron mobility in graphene on different substrates.	102
Figure 8.2 (A) Schematic diagram of the assembled lateral flow device (LFD) for blood separation and flow control. (B) Schematic diagram shows the interfacial layer and the microfluidics capillary pump. (C) A picture shows the fabricated LFD.....	103
Figure 8.3 Real-time detection of IgG using nanoelectronics sensor integrated with the LFD. (A) A representative picture shows a fabricated LFD integrated with a nanoelectronics biosensor; (B) Continuous measurement of the drain current as responding to the addition of IgG with increasing concentrations; (C) The detection of IgG directly from human plasma.	104
Figure A1. Characterization of graphene upon functionalization. (a) C1s and N1s XPS spectrum. (b) Raman spectrum. (c) Transfer curves measured in 0.01X PBS with $V_{ds}=0.01$ V.	106
Figure A2 Derivation of the V_{Dirac} from the transfer curves. a) the original transfer curve (I_d vs V_g). b) the slope of I_d vs V_g . c) V_g vs slope and the linear regression near. d) Enlarge view of the transfer cure as indicated by the box in a).	107

Figure A3 Optimization of the operation parameters of the EGGFET biosensor. a) Hysteresis of the forward and backward transfer curves measured with scan rate of 100 mV/s. b) The V_{Dirac} and I_{Dirac} (minimum drain current) of the forward and backward transfer curves at different scan rates. c) The transfer curve (I_d), leakage current (I_g) and transconductance (g_m) of the EGGFET measured in 0.01X PBS.....	109
Figure A4 The determination of the LOD.....	112
Figure A5 Determination of the detection range of the EGGFET biosensor for IgG detection. a) the fitting curve of the measurement results; b) the slope of the fitting curve; c) the SD of the concentration estimates; d) the RSD of the concentration estimated with respect to the concentration.....	113
Figure A6 The plot showing $-Li_2(-e^\eta) \cong 2 \times \eta^2$	117

List of Tables

Table 6-1 Summary of the fitting parameters and the measured results	67
Table 6-2 Summary of the biosensors for IgG detection	69
Table 7-1 Comparison of the fitting result based on the two models	91

Chapter 1. Dissertation overview

1.1. Background and Motivations

The specific detection of biomolecules is of critical importance in a variety of fields, such as disease diagnosis, food quality inspection, environment monitoring, etc. Traditional analytical techniques rely on complicated instruments and complex operations, e.g. high performance liquid chromatography - mass spectrometry (HPLC-MS) and enzyme-linked immunosorbent assay (ELISA) [1,2]. These techniques are expensive, time-consuming, demanding on operation skills and cannot meet the expanding demands of the fast developing society [3,4]. Biosensors are easy to use, capable for rapid detection with high sensitivity and selectivity, feasible for mass production and thus are speculated as a ubiquitous technology of the future for human health and wellbeing [5–7].

Biosensor is a device that uses specific biochemical reactions mediated by isolated enzymes, immunesystems, tissues, organelles or whole cells to detect chemical compounds usually by electrical, thermal or optical signals [8]. The first biosensor can be dated back to 1962, as reported by Leland C. Clark Jr. [9]. Since then various types of biosensors have been developed, including electrochemical, optical, piezoelectric, thermometric, magnetic or acoustic ones, etc., classified by the transducing mechanism [5,7,10]. Successful detection of various analytes has been reported, such as metabolites [11,12], nucleic acids [13,14], proteins [15,16], etc. However, despite the wide prospect, till now the practical application of biosensors is still quite limited [5,6]. The challenges include the unsatisfactory performance, impracticability for real sample analysis, lack of corollary equipment, etc. [5,6]. In recent years, the rapid development of the nanotechnologies opens up new opportunities to promote the development of the biosensors [4,17–20]. On one hand, the performance of the biosensors were significantly improved by the introduction of nanomaterials;

on the other hand, new biosensing mechanisms are being discovered in nanoscale, such as surface enhanced Raman spectroscopy (SERS) [21].

Among the various types of biosensors, field effect transistor (FET) biosensors are of particular interest due to their high sensitivity, simple configuration and cost-effective mass producibility, which make them highly promising as the next generation nanoelectronics biosensors for point-of-care biomedical applications [19,22–24]. FET biosensors typically operate by measuring the conductance change of the channel induced by the specific adsorption of target molecules on it. The first FET biosensor (ion-selective field effect transistor, ISFET) was invented by Bergveld in 1970 using silicon semiconductor [25]. Over the recent years, the development of the FET biosensors has been significantly boosted by the introduction of the nanomaterials, such as silicon nanowire (SiNW) [26–28], carbon nanotube (CNT) [19,20,29] and graphene [19,30]. Among them, the single-atom-layer structure and the superior properties of graphene, including the unique electronic characteristics, facile functionalization and good biocompatibility, etc., make it an attractive candidate for the building block of FET biosensors [22,31,32]. Significant progress has been made on the development of the electrolyte-gated graphene field effect transistor (EGGFET) biosensors over the last decades [22]. The outstanding properties of graphene and relatively simple preparation make EGGFET biosensor a latecomer outperforming biosensors based on SiNW and CNT on performance and mass producibility [33,34].

However, till now the development of the EGGFET biosensors is still in the stage of proof-of-concept and challenges still exist for their practical applications. Firstly, the one-atom-layer structure of graphene makes it vulnerable to material imperfections, such as lattice defects, contaminations, etc., which are still difficult to avoid with the current preparation and fabrication techniques [33]. The significant device-to-device heterogeneity leads to poor reliability and could

be fatal to the usability of EGGFET biosensors [19,35]. Secondly, in EGGFET, the gate voltage is applied on the electrolyte and the electrical double layer (EDL) at the electrolyte-graphene interface serves as the gate dielectric, which makes it much more complicated compared with the traditional metal-oxide-semiconductor field effect transistors (MOSFET). Detailed understanding on the electrolyte-graphene interface and its impact on the electronic transport in graphene are still lacking, while critical for the design, development and operation of the EGGFET biosensors [19]. Lastly, despite outstanding performance have been reported, almost all of the results were based on experiments using simplified samples in laboratory settings [5,19,22]. The reliability of the EGGFET biosensors is still to be studied to deal with the complicated physiological samples and strategies to enable their practical application are still to be devised. These issues must be addressed to bring the development of the EGGFET biosensors forward.

1.2. Objectives

The main objective of this dissertation is to develop a novel nanoelectronic biosensor based on the EGGFET structure for the label-free detection of biomarkers. The performance of the EGGFET biosensor is to be demonstrated by the detection of human immunoglobulin G (IgG) with high specificity. Specifically, this dissertation focuses on:

1) Improving the fabrication process of the EGGFET biosensors. To obtain reliable device with high performance, efforts were taken to address the issues caused by the PMMA residues on the graphene surface that was introduced during the transfer of the CVD graphene. The thermal degradation of the PMMA residues was studied based on the analysis of the evolution of the Raman spectrum upon annealing at different temperature and for different durations. An electrolytic cleaning method was developed to effectively remove the post-annealing residue, resulting in a clean graphene surface, which is critical to obtain working devices.

2) Test the performance of the as-developed EGGFET biosensor by the demonstrative detection of human IgG. The underlying biosensing mechanism is confirmed based on the measurement of the transfer curve of the EGGFET biosensor upon IgG adsorption. The selectivity of the EGGFET biosensor is tested by introducing possible interfering analytes.

3) Study the electrolyte matrix effect on the EGGFET biosensor to validate its utility for real sample analysis. The response of the EGGFET biosensor to the variation in the electrolyte matrices was studied by varying the composition, ionic strength and pH of the electrolyte. The electrolyte matrix effect on the gate potential and the sensitivity of the EGGFET biosensor were also studied. The study should provide guidance for the practical applications of the EGGFET biosensor which is challenged by the complexity of the physiological samples.

4) Develop a novel point-of-care immunoanalytical device based on the EGGFET biosensor. An EGGFET immunoassay is presented and the performance is demonstrated by the detection of IgG from serum. The EGGFET immunoassay allows well regulation of the matrix effect and statistical validation of the measurement results by duplicate channel design. The developed EGGFET immunoassay is easy to use, ready to be integrated with microfluidics sensor platform, suggesting its great prospect for practical applications.

5) Study the capacitance behavior of the electrolyte-graphene interface and the carrier statistics in graphene. The frequency response of the electrolyte-graphene interface is studied, which provides a more accurate understanding on the capacitance behavior. The electrical double layer (EDL) capacitance and the quantum capacitance were determined, which allows us to extract the carrier mobility in the graphene. The study should be instructive for the future improvement of the EGGFET biosensor from the aspect of the device design.

1.3. Significance and novelty

The work in this dissertation should contribute to the development of the EGGFET biosensors from the following aspects:

- 1) The study on the formation of the post-annealing residues leads to a more in-depth understanding on the degradation of the PMMA residues upon thermal annealing. The electrolytic cleaning method provides a novel strategy to remove the post-annealing residues, resulting in a clean graphene surface, which is critical to obtain working devices. The study would be instructive for the development of the CVD graphene transfer techniques which is important for its applications in not only the EGGFET biosensors but also many other fields [34].
- 2) The development of the EGGFET biosensor provides a novel biosensing platform for the label-free detection of biomarkers. The performance of the EGGFET biosensor is demonstrated by the successful detection of human IgG.
- 3) The study on the electrolyte matrix effect on the EGGFET biosensor addresses critical issues that challenge its usability to deal with complex physiological samples.
- 4) The EGGFET immunoassay allows well regulation over the matrix effect and is demonstrated to be able to detect IgG from serum. The multichannel design allows duplicate measurements and on-site calibration with negative control, and thus statistical validation of the results. Compared with traditional immunoassay techniques, the EGGFET immunoassay is label-free and ready to be integrated with electronic devices, showing great potential as the next-generation immunoassay technique. The EGGFET immunoassay provides a general strategy which accommodates with the state-of-the-art development of the EGGFET biosensors and is promising to make the breakthrough for its practical applications.
- 5) The study on the device physics of the EGGFET provides an in-depth understanding on the capacitance behavior of the electrolyte-graphene interface. The EDL capacitance and the quantum

capacitance are determined based on the capacitance-voltage profiling measurement, which allows us to extract the carrier mobility in the graphene. The study should be instructive for the future design of the EGGFET biosensor and the improvement of its performance.

1.4. Structure of the dissertation

The following chapters are covered in this dissertation. It is initiated with an overview of the dissertation in **Chapter 1**, in which the background and motivations, the objectives, and the significance are introduced. In **Chapter 2**, the properties, synthesis technique and functionalization of graphene are introduced; the state-of-the-art development of the graphene-based biosensors is reviewed. In **Chapter 3**, the fabrication processes of the EGGFET biosensors were demonstrated. In **Chapter 4**, we present a study on the thermal degradation of the PMMA residue on the transferred graphene and its removal with an electrolytic cleaning method, which is critical to obtain working devices. In **Chapter 5**, the performance of the EGGFET biosensor is demonstrated by the detection of the human immunoglobulin G (IgG). In **Chapter 6**, the impact of the electrolyte matrix on the operation of the EGGFET biosensor is studied and an EGGFET immunoassay is demonstrated to be able to detect analytes from real physiological samples. In **Chapter 7**, we present studies on the device physics of the EGGFET, including 1) the capacitance behavior of the electrolyte-graphene interface; 2) the determination of electrical double layer (EDL) capacitance and the quantum capacitance; and 3) the extraction of the carrier mobilities in the graphene channel. In the end, I will conclude my dissertation with an outlook on the future development of the EGGFET biosensors. **Chapter 8** summarizes the conclusions and provide an outlook on the future development of the EGGFET biosensor.

Chapter 2. Literature Review

In this chapter, the basics about graphene are introduced, including its properties, synthesis methods and functionalization approaches. The state-of-the-art development of the EGGFET biosensors is reviewed with respect to 1) the targets that have been detected using EGGFET biosensors; 2) the types of graphene that have been employed for the fabrication of the EGGFET biosensors; and 3) the efforts to improve the performance of the EGGFET biosensors. In the end, we remark the development of the EGGFET biosensors with regarding to the challenges and prospect for future development and applications.

2.1. Graphene: properties, synthesis and functionalization

Graphene is a two-dimensional one-atom-layer allotrope of carbon with sp^2 -hybridized carbon atoms arranged in honeycomb lattice (**Figure 2.1a**). The sp^2 hybridization leads to the formation of the σ bonds between carbons that are separated by 1.42 \AA and the overlap of the remaining p orbitals leads to the formation of the π bands that are half filled. The delocalized π electrons endow graphene with abundant unique physical and chemical properties. Graphene is the basic building

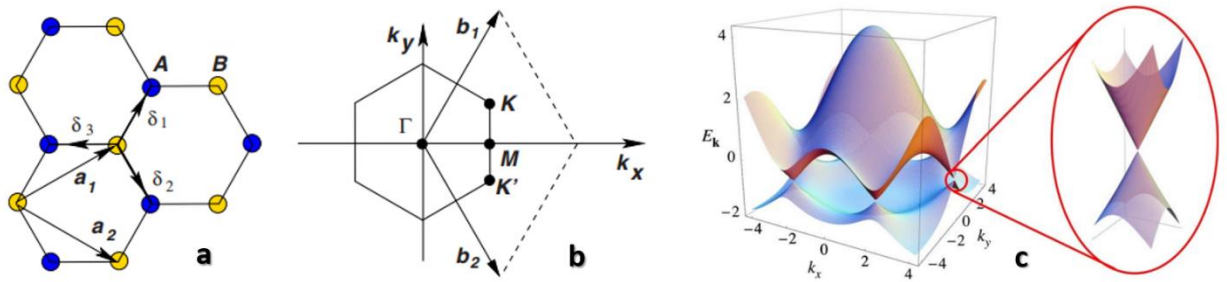


Figure 2.1 Lattice structure and energy dispersion of graphene. (a) the honeycomb lattice structure, (b) the Brillouin zone and (c) electronic dispersion of graphene with zoom in of the energy bands close to one of the Dirac points. (Reprinted from [36])

block for other carbon allotropes, including graphite (stacked graphene), CNT (rolled graphene), fullerene (wrapped graphene), etc.

Graphene is a zero bandgap semiconductor with the conduction band and the valance band meeting at the Dirac points (**Figure 1c**) [36]. The Dirac points are located at the K and K' point of the Brillouin zone of graphene (**Figure 1b**). The linear energy dispersion (**Figure 1c**) at low energy level makes electrons and holes behave as relativistic massless Dirac fermions which move with a speed of around 1/300 of the speed of light c [36,37]. Another interesting feature of the Dirac fermions is the ballistic transport with a mean free path of micrometers [36,38,39]. As a result, graphene exhibits remarkable charge carrier mobility at room temperature. Theoretical studies indicate that the intrinsic mobility in single layer graphene can be as high as $2 \times 10^5 \text{ cm}^2\text{V}^{-1}\text{s}^{-1}$ at a carrier density of $1 \times 10^{12} \text{ cm}^{-2}$ (limited by the scattering of graphene's acoustic photons), the highest among all the existing materials [40]. Graphene exhibits ambipolar electric field effect due to the symmetric band structure (**Figure 2.2**) [39].

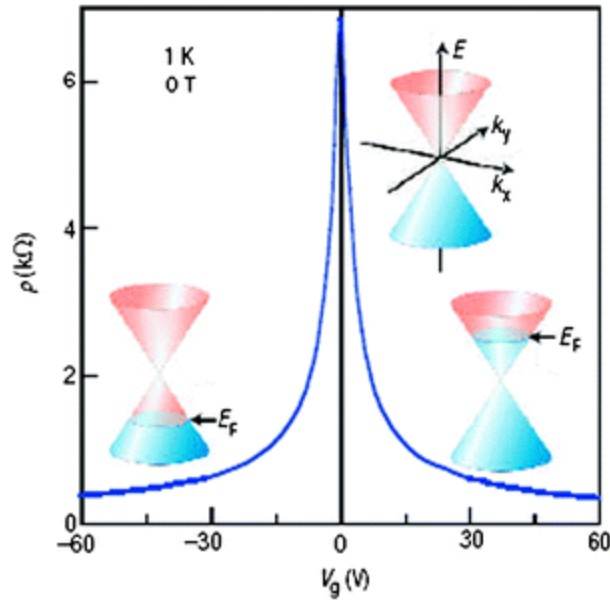


Figure 2.2 The ambipolar electrical field effect of graphene with schematics showing the band filling structure (Reprinted from [39]).

Single layer graphene absorbs around 2.3% of white light, which is rather opaque when considering that it is only one atom thick [41]. The high opacity is attributed to the aforementioned electronic characteristics and can be used for the location of the graphene during the fabrication of graphene-based devices. Graphene is the strongest material ever tested, with an intrinsic tensile strength of 130.5 GPa and a Young's modulus of 1 TPa [42].

While the theoretical study on graphene has been for decades [43], few layer graphene had not been achieved or rather being recognized to exist till 2004 [39]. Before that graphene was considered unstable and would roll up in order to reduce the surface energy [44,45]. The first few layer graphene was obtained by repeating exfoliation of highly ordered pyrolytic graphite (HOPG) with scotch tape [39]. The interlayer van der Waal's force is much smaller comparing with the intralayer covalent bond and easy to overcome which enables the mechanical exfoliation of graphene [37,39,46]. Single layer graphene of several hundred microns in dimension was obtained by an improved exfoliation process which involves oxygen plasma cleaning of the substrates and additional heat treatment [47]. The graphene obtained by mechanical exfoliation can be single crystal and provides the best electrical properties. It has enabled a large number of researches on both the intrinsic properties and also the applications of graphene in various fields. Many other preparation methods were derived from the mechanical exfoliation, such as using polydimethylsiloxane (PDMS) stamps [48], liquid-phase exfoliation assisted by sonication [49], ball milling [50], etc. A review on the exfoliation-based preparation methods for graphene can be found in [46]. However, the mechanical exfoliation methods are themselves limited and cannot be used for large-scale mass production.

An alternative to the mechanical exfoliation of graphene is the chemical vapor deposition (CVD) of graphene on nickel [51] and copper [52], which were reported in 2008 and 2009, respectively.

Due to the extremely low solubility of carbon in these metals, the carbon atoms that were absorbed at high temperature (around 1100 °C) tend to precipitate during the cooling process and rearrange into graphene [52–54]. Monolayer CVD graphene as large as 30 inch was grown on copper using roll-to-roll stacking [55]. It is important to note that electrical properties of the CVD graphene are significantly dependent on the amount of crystalline boundaries [53,54]. Significant efforts have been taken to realize the CVD growth of single crystal graphene by either adjusting the process parameters or changing the precursors and catalysts [56–60]. For example, fast growth of meter-sized single-crystal graphene was obtained using single crystal copper foil as substrate [61]. For electronic application, CVD graphene must to be transferred to insulating substrates from the metal substrates on which it is grown. Various methods have been developed for the graphene transfer, including the dry methods and wet methods [62–64]. Among them the poly(methyl methacrylate) (PMMA)-assisted transfer of graphene is the most widely used. One problem that has been bothering the PMMA-assisted graphene transfer is the PMMA residue on graphene [34,65]. Many attempts have been made by researchers to remove the PMMA residues [66–68], among them thermal annealing in high vacuum or protective atmosphere is generally considered as the most efficient approach. Our study indicates that there is still residues left on graphene after thermal annealing and an electrolytic cleaning method was proposed and tested to be effective in removing the post-annealing residues [65].

Another method for graphene synthesis is epitaxial growth on silicon carbide (SiC) [69,70]. This method is based on that silicon atoms sublimes faster than carbon from the surface of SiC and the carbon left can be rearranged to form graphene layer. Epitaxial graphene can be used directly without transfer and the corresponding polymer contamination and is promising for industrial application [71]. Besides, graphene can also be obtained by reduction of graphene oxide (GO) using thermal, chemical or electrochemical methods [72–74]. Reduced graphene oxide (RGO) consists a lot of oxygen-containing groups and thus has good chemical activity which can be used in certain fields, such as electrochemical biosensors. A comparison between the different synthesis techniques with regarding to the quality and cost for mass production is shown in **Figure 2.3** [75].

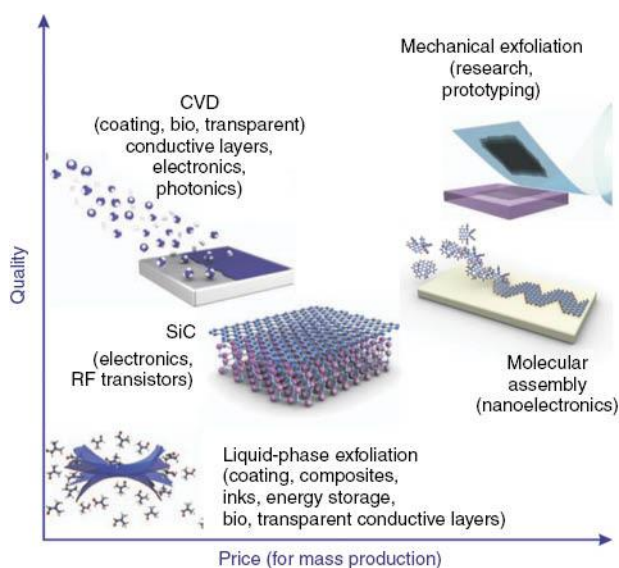


Figure 2.3 The techniques for the synthesis of graphene with respect to their quality and price for mass production. Reprinted from [75].

To realize the specific detection of analytes, graphene needs to be functionalized with corresponding biorecognition groups, otherwise known as bioreceptors. Various methods have been evolved for the graphene functionalization using either covalent or non-covalent binding [76–78]. The covalent functionalization of graphene involves two general routes: the formation of

covalent bonds with C=C bonds in graphene and the oxygen groups on GO [77]. The covalent functionalization has an advantage in terms of stability and reproducibility, however, it will cause the degradation of the conductivity of graphene which limits its application [76,77,79]. In contrast, non-covalent approaches allow the immobilization of biomolecules on graphene via electrostatic interactions, e.g. π - π stacking, entrapment or van der Waals force, without interfering the sp² structure of graphene and thus will not damage its electrical properties. It's worth noting that the π - π stacking is an efficient approach for non-covalent functionalization of graphene due to the wide existence of benzene groups in natural and synthesized molecules.

2.2. Development of graphene-based field effect transistor biosensors

The first GFET biosensor was reported by Mohanty in 2008 using chemically modified graphene (CMG) for DNA hybridization [80]. Since then the research on this field has enormously increased due to its significance in future healthcare and other fields. In this section, the development of GFET biosensors is reviewed with respect to the following aspects: 1) the targets that have been detected using the graphene-based FET biosensors, 2) the types of graphene that have been used for the fabrication of the graphene biosensors, 3) the efforts that have been taken to improve their performances.

2.2.1. The detecting targets of GFET biosensors

Various targets have been detected using GFET biosensors, including nucleic acids, proteins, and other biologically relevant species. The detection of nucleic acids, e.g. DNA, RNA, is considered important for physiological study, disease diagnosis, genetic screening, etc. [81,82]. The high negative charges on the phosphate backbones and high matching efficiency enable the successful detection of nucleic acids with high sensitivity [18,80,83]. As mentioned above, the first GFET biosensor for DNA detection was demonstrated by Mohanty in 2008 [80]. Later, Dong et al.

reported detection of DNA hybridization with high specificity of 0.01 nM and the capability of identifying single base mismatches [83]. DNA detection with sensitivity down to 1 pM was achieved by Chen using single layer graphene FET [84]. The sensing mechanism of GFET DNA biosensors was investigated by Lin et al. using Hall effect and found the hole carriers density increases upon the binding of complementary DNA strands [85]. Recently ultrasensitive detection of DNA with detection limit as low as 100 fM was reported using peptide nucleic acid (PNA) modified reduced graphene oxide (rGO) [86]. The sensitivity was further improved to 10 fM using PNA modified single layer CVD graphene by the same group in 2015 [87]. A robust DNA array yield – seven out of eight transistors – was reported with a 100 fM sensitivity by Xu [88]. A scalable and reproducible (> 90% yield) fabrication process for label-free DNA biosensors was reported in 2016 [89]. In general, the detection of DNA with GFET biosensor exhibits high sensitivity and reproducibility due to the abundant charge and unique structure of DNA chains and is highly promising for practical applications.

The rapid detection of proteins is of critical importance for disease diagnosis, drug development and physiological research [90]. The detection of proteins by FET biosensors is based on the surface charge on proteins and high affinity and specificity of the antibody with respect to corresponding antigen [22,91]. The biosensors for proteins are therefore also called immunosensor. Given the rapid increasing demand for disease diagnosis and huge promises of EGGFET immunosensors, the development of EGGFET has long been a hot research area. In 2009, Ohno et al. reported the detection of bovine serum albumin (BSA) using non-functionalized EGGFET [92]. The EGGFET biosensor that was functionalized with antibody Fab fragment and aptamer for the detection of immunoglobulin E (IgE) was reported by the same group [93,94]. Chen and co-workers reported a graphene-gold nanoparticle hybrid sensor for protein detection [95,96]. An all

rGO device was fabricated on a transparent and flexible substrate and shown to detect fibronectin at concentrations as low as 0.5 nM [97]. An epitaxial graphene immunosensor for the detection of human chorionic gonadotropin (hCG), which is a key diagnostic biomarker of pregnancy and also cited as an importance biomarker in relation to cancerous tumors found in prostate, ovaries and bladder was reported by Teixeira [98]. Lei and coworkers reported the successful detection of brain natriuretic peptide (BNP) in whole blood, which is specific to heart failure, using a platinum nanoparticle (PtNP) decorated rGO-FET immunosensor [99]. In 2017, Zhou et al. demonstrated the development of a GFET for the real time monitoring of carcinoembryonic antigen (CET) detection with detection limit of 0.5 pM, far exceeding that of the clinical diagnostic cut-off value [100].

EGGFET immunosensor features simplicity for use and production, portability, high sensitivity, utilizes a small amount of sample, enables real-time analyte detection and quantification [101]. However, compared with DNA, the reliability of proteins is inferior, and the charge is dependent on the specific structure. As a result, the performance of the EGGFET immunosensors are relatively lower than that of DNA biosensors.

EGGFET biosensors have also been developed to detect other biologically relevant species. Chen and his coworkers used GFET to detect glucose and glutamate, with a limit of detection (LOD) of 0.1 mM and 5 μ M, respectively [102]. The detection is mediated by surface-functionalized glucose oxidase and glutamate dehydrogenase which serve as catalysts to produce H_2O_2 molecules. As a strong electron withdrawing molecule, H_2O_2 acts as a p-dopant for the graphene channel. In 2010, He et al. demonstrated that rGO devices can be applied for the detection of dynamic secretion from living cells [97]. Real time monitoring of nitric oxide (NO) using EGGFET biosensors based on the charge transfer between NO and the surface-functionalizing porphyrin were reported [103,104].

In addition, EGGFET biosensors are also reported to be effective in detecting bacteria [80,105], viruses [106], and cells [107].

2.2.2. The type of graphene used in GFET biosensors

The development of the EGGFET biosensor was also promoted by the maturing of the preparation technique of graphene. Reduced graphene oxide (rGO) was first applied before the laboratory synthesis of graphene in 2004 [39,80] and have been continuously developed after then [95,108–110]. Even though the electrical properties are inferior with respect to the graphene prepared by mechanical exfoliation and chemical vapor deposition (CVD), the surface oxide-containing groups in rGO make it promising for biosensing due to the diverse routes for chemical functionalization. The preparation of few layer graphene in lab using mechanical exfoliation triggered the application of “true” graphene in the biosensors [39]. The theoretical studies on the electronic characteristic of graphene were verified [36,39] and many GFET biosensors were developed using the mechanically exfoliated graphene [92,94]. However, the mechanical exfoliation of graphene is itself limited and cannot be used for practical applications. The development of the preparation of graphene by chemical vapor deposition (CVD) opened up new opportunities to realize the real applications of GFET biosensors and were proven to be capable for mass production owing to its compatibility with surface microfabrication techniques [83,84,87,102,111]. In recent years, GFET biosensors based on epitaxial graphene was reported which exhibits higher homogenous performance due to the single crystal feature [112,113].

The development of the graphene preparation techniques make GFET an latecomer outperforming the existing FET biosensors based on SiNW and CNT [31]. The poor reproducibility and difficulties of large-scale integrated processing of SiNW and CNT pose major obstacles for the practical applications. For example, the electrical properties of CNT are dependent on the

crystalline orientations, such as armchair, zigzag and chiral, which bring significant challenge to the reliable preparation of CNT. In contrast, the electrical properties of graphene are isotropic which could significantly simplify the fabrication process and reduce the mass-production cost [114,115].

2.2.3. Efforts to improve the performance of the EGGFET biosensors

The Debye screening limit is considered as one of the fundamental challenges for FET biosensors [24]. In physiological liquid with high ionic strength, the electrostatic effect of charge is screened which exhibits weak modulation capability and thus cannot be detected [116]. During the past few years, considerable efforts have been directed to overcome this physical limitation of FET biosensors. To reduce the Debye screening effect, diluted electrolytes were used in which the Debye length is increased [110,117]. This strategy cannot be used for the real-time detection from physiological solutions, which is one of the most promising advantage of FET biosensors over other biosensing architectures. Bioreceptors of smaller size were used for the functionalization of EGGFET biosensor, such as utilizing antigen binding fragment (Fab) [93] and aptamers [94,118] as alternatives for whole antibodies. Ping [119] reported the study on quantifying the effect of ionic screening with protein-decorated graphene transistors. Other strategies were also developed to overcome the Debye screening and enable the operation of EGGFET biosensors in physiological solutions. Kulkarni [120] demonstrated that the fundamental ionic screening effect can be mitigated by operation FET biosensors in high-frequency mode. The nonlinear mixing between the alternating current excitation field and the molecular dipole field can generate mixing current sensitive to the surface-bound molecules. Fu [121] reported a frequency-doubling biosensor based on the ambipolar electrical field behavior of the EGGFET. By biasing the ambipolar GFETs in a common-source configuration, an input sinusoidal voltage at frequency f applied to the electrolyte

gate can be rectified to a sinusoidal wave at frequency $2f$ at the drain electrode. Gao [122,123] demonstrated a general strategy to overcome the Debye screening effect by incorporating a biomolecule-permeable polymer layer on the surface of SiNW FET biosensors EGGFET biosensors. The studies indicate that EGGFET biosensor that is coated with polyethylene glycol (PEG) exhibits detection capability in physiological liquids.

The performance of the EGGFET biosensors is further improved by decoration with metal nanoparticles, which serves to increase the surface area and bioreceptor density [22]. Mao reported the IgG detection using thermally reduced graphene oxide (TRGO) sheet decorated with gold nanoparticle (AuNP)-antibody conjugates [95,96]. Chan demonstrated the signal amplification by directly assembling AuNP conjugated reporter probes on graphene for the detection of avian influenza A virus subtype H7 gene [124]. A novel mechanism of metal nanoparticle formation on graphene by galvanic displacement was developed by Gutes [125] and its integration onto a gas sensing transducer was presented as proof of concept. Lei [99] reported the detection of heart failure-related biomarker brain natriuretic peptide (BNP) in whole blood with platinum nanoparticle (PtNP) decorated GFET biosensors. The sensor was integrated with a custom-made microfilter and exhibited capability of working in a complex sample matrix. AuNP-decorated EGGFET was also used to measure the binding affinity of specific protein-antibody interactions [126].

Microfluidics is a technology featured by the engineered manipulation of fluids at the micrometer scale [127,128]. There have been a number of reports that integrate microfluidics with FET biosensors based on Si [129,130], AlGa_N [131], SiNW [132], etc. The integration of the high sensitivity of FET biosensors and the sample processing capabilities of the microfluidics, such as flow control, separation, concentration, etc., has shown considerable promise for improving

diagnostics and biology research [133,134]. Stern [135] integrated an silicon nanoribbon detector with a microfluidic purification system which can be used for the label-free detection of biomarkers from whole blood. Given the superior performance of GFET biosensors and good compatibility, the integration between GFET biosensors and microfluidics would be of great significance.

2.3. Comments

Compared with other biosensing techniques, FET biosensors are particularly favored for potentials in portable and point-of-care applications due to their high sensitivity, simple configuration and cost-effective mass productivity [22]. It is clear that graphene has many superior qualities compared with other nanomaterials which makes EGGFET biosensors highly attractive as the next generation bioelectronics [19,22,31]. Significant progress has been made on the development of the EGGFET biosensors during the last decade, however almost all the results were obtained using samples with the highest quality within a laboratory setting. Similar with other biosensors, the EGGFET biosensors are still in the stage of proof-of-concept and challenges still exist for its practical applications.

Firstly, the reliability of the EGGFET biosensors is still inferior to meet the requirement for practical applications, which is one of the bottle-necks that hindering the further development of almost all the nanomaterial-based biosensors. Till now, the performance of EGGFET biosensors is still suffering from the significant device-to-device heterogeneity, which leads to poor reliability and could be fatal to the usability of the EGGFET biosensors [19,35]. The development of the reliable and reproducible fabrication techniques are critical issues to be addressed in future.

Secondly, except for a few cases, most of the currently existing reports were carried out in ideal media such as pure buffer solutions. The real physiological samples are far more complex and will

definitely introduce certain interfering and fouling effects. The usability of the EGGFET biosensor for practical application is still to be validated. On the other hand, strategies that can reduce or eliminate these effects are to be put forward to realize the practical application of the EGGFET biosensors.

Furthermore, the in-depth understanding on the device physics of the EGGFET biosensors is still lacking, which is critical for the further improvement of the EGGFET biosensors. Although EGGFET biosensors have been demonstrated to be capable of detecting various targets, very limited efforts have been directed to improve the design of the EGGFET on the device level. For example, silicon dioxide (SiO_2) is typically used as the substrate for graphene in EGGFET. However, the carrier mobility of graphene is significantly limited by scattering of the charged impurities on the SiO_2 surface, which could cause the deterioration of the sensitivity of the EGGFET. Improving the device design is promising to further improve the performance of the EGGFET biosensors.

Chapter 3. Fabrication of the EGGFET biosensor

3.1. Structure of the Devices

A schematic diagram of the EGGFET structure is shown in **Figure 3.1**. It consists of a gate electrode and a graphene channel that is connected by the source/drain electrodes. Here a basic structure is shown for the illustration of the fabrication process. Specific configurations of the devices are presented in the corresponding chapters.

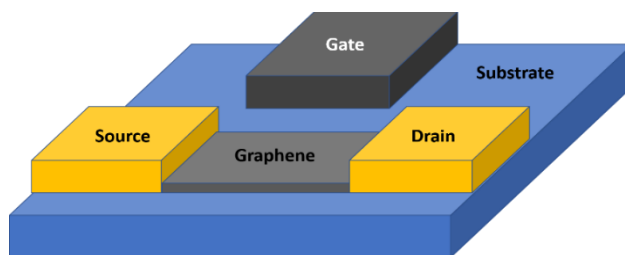


Figure 3.1 Basic structure of the EGGFET biosensor

3.2. Fabrication of the devices

3.2.1. Graphene transfer and electrolytic cleaning

The fabrication of the EGGFET biosensor starts with the transfer of the CVD graphene. In this work, the graphene was transferred using the PMMA-assisted method followed by thermal annealing and electrolytic cleaning to remove the polymer residues. The schematic process of transferring the CVD graphene and the experimental setup for the electrolytic cleaning is shown in **Figure 3.2**. The CVD graphene grown on copper foil was purchased from Graphene Supermarket and transferred onto glass slides (or silicon wafers with oxide layer) with the following procedures. First, PMMA (950 kDa, 4% in anisole, MicroChem) was spin-coated on the graphene on copper foil at a spin speed of 2000 rpm for 45 s, and then allowed to cure on a hotplate at 120 °C for 1 min. After curing, the graphene on the backside of the copper foil was removed by oxygen plasma (30 W) for 90s. The samples were then placed floating on an iron (III) nitrate

solution (0.7 M, Sigma Aldrich) with the copper-side facing downward for 3 h to etch the copper off, followed by rinsing by transferring onto deionized (DI) water for 3 times. The resulting PMMA/graphene films were lifted up with glass slides (or oxide silicon wafer) and allowed to dry

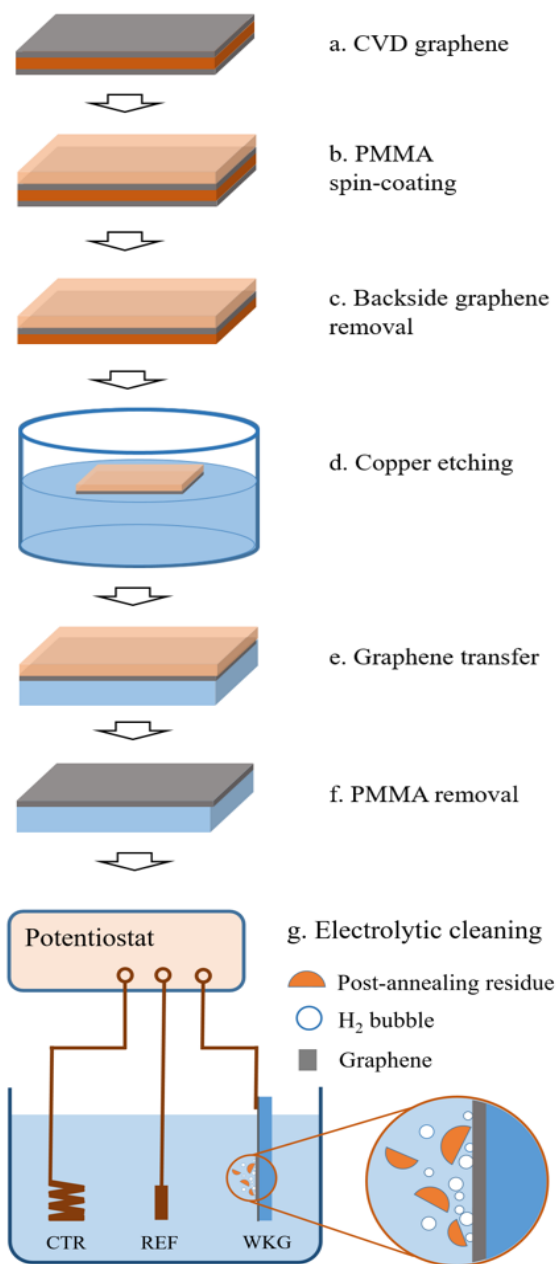


Figure 3.2 Schematic of the transfer process of CVD graphene and the experimental setup for the electrolytic cleaning. (Reprinted from [65])

at room temperature for 1 h. The samples were then heated at 75 °C for 30 min to improve the contact between graphene and the substrates. The PMMA was removed by immersing in acetone for 10 min and then rinsed with IPA and DI water. The samples were then annealed at 250 °C in N₂ atmosphere with a flow rate of 1000 sccm to remove the PMMA residue. Thermal annealing was performed with an AS-Micro rapid thermal annealer. To confirm that the copper has been completely removed and no iron contamination was introduced during the transfer process, we used XPS to characterize the as-transferred graphene. As shown in **Figure 3.3**, no significant XPS peaks for copper and iron can be observed, which suggests that clean transfer of the graphene.

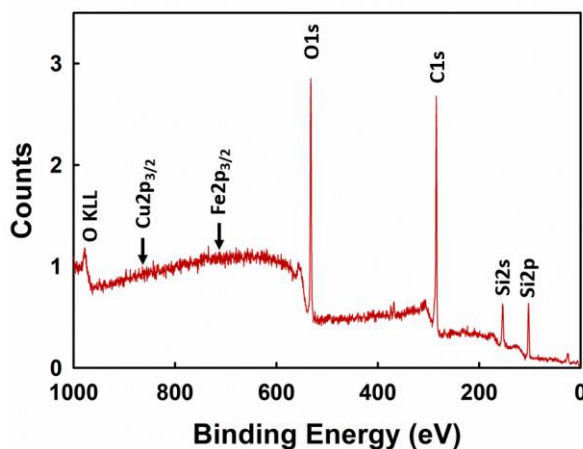


Figure 3.3 XPS spectrum of the as-transferred graphene

Electrolytic cleaning of graphene was conducted with a Gamry Interface 1000T potentiostat in the chronoamperometry mode. The three-electrode electrochemical cell was comprised of the graphene sample as the working electrode, a Ag/AgCl reference electrode (Aldrich), and a platinum wire counter electrode. 0.5 M sulfuric acid (H₂SO₄, Sigma Aldrich, 95%~98%, 20 mL) was used as the electrolyte because it is conducive to hydrogen evolution and can neutralize the OH⁻ generated close to the graphene surface to prevent etching the underlying silicon dioxide substrate. The electrolyte was used as prepared without purge and no stirring was applied throughout the electrolytic cleaning process. To ensure reliable electrical connection, a copper tape

was applied on the transferred graphene. The sample was then covered with a piece of Scotch tape with a round opening of 4 mm in diameter which serves to 1) isolate the copper tape from the electrolyte and 2) confine the area of graphene for electrolysis. To remove the post-annealing residue, the graphene was cleaned with the electrolytic method at -5 V vs Ag/AgCl for 30 min. The sample was then rinsed by DI water thoroughly and blown dry with N₂.

3.2.2. Fabrication of the electrodes and the graphene channels

The schematic of the fabrication process of the source/drain electrodes is shown in **Figure 3.4**. After washing with acetone and IPA and drying at 75 °C for 30 min, 5 nm nickel and 45 nm gold were deposited on the sample using e-beam evaporation. The electrodes were patterned by photolithography using AZ5214E photoresist (MicroChemicals) followed by etching in gold etchant (Gold Etch TFA, Transene) for 10 s. A second photolithography process was applied to create a shielding photoresist layer on the graphene channel. The exposed nickel was then etched using nickel etchant (Nickel Etchant, TFB, Transene, 10s). The graphene channel was patterned by oxygen plasma etching (100 W for 90 s with oxygen flow at 49 sccm) and the shielding photoresist layer was then removed using acetone followed by rinsing with IPA and DI water. A

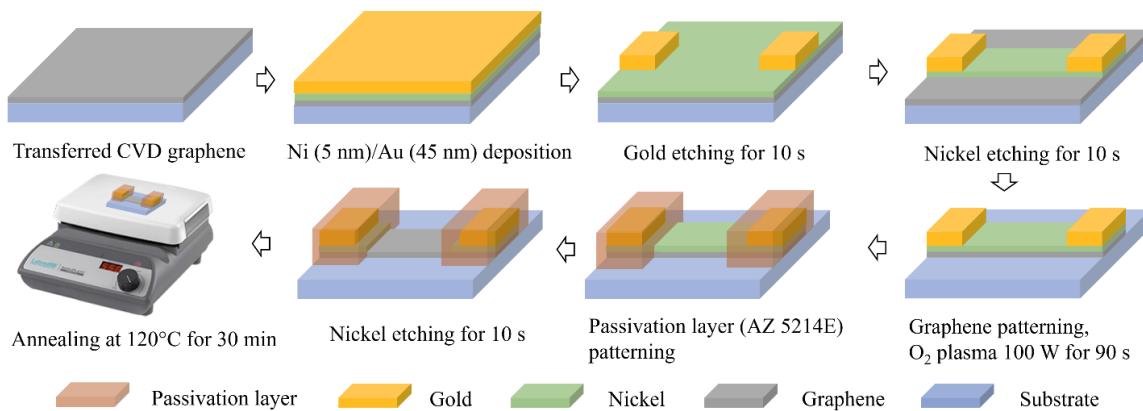


Figure 3.4 Schematics of the fabrication process of the gate/source/drain electrodes and the patterning of the graphene channel.

third photolithography process was implemented to create a passivation layer (AZ 5214, $\sim 1.5\ \mu\text{m}$ thick) on the source/drain electrodes. The remaining nickel on the graphene was finally removed using nickel etchant (10 s). The devices were then annealed at $120\ ^\circ\text{C}$ on a hot plate to for 30 min to 1) improve the contact between graphene and the source/drain electrodes; 2) strengthen the passivating photoresist layer.

For the fabrication of the EGGFET immunoassay, Ag/AgCl pseudo-reference electrodes were fabricated using electroplating methods. A three-electrode cell with a standard Ag/AgCl reference electrode, a gold wire coil counter electrode was used for the electroplating of Ag/AgCl on the as-fabricated gold electrode. The schematic and experimental setup are shown in **Figure 3.5**. The electroplating was conducted using a Camry Interface 1000T potentiostat. For the electroplating of silver, 0.3 M silver nitrate (AgNO_3) and 1 M ammonia (NH_3 , aq) solution was injected into the chamber. First, an oxidative pre-treatment at $+0.95\ \text{V}$ was applied for 30 s. For better results, the sample was placed in vacuum for 30 min to remove the dissolved oxygen and the microscopic gas bubbles on the electrode surface. Then the electroplating was driven at $-0.5\ \text{mA}$ for 300 s, resulting

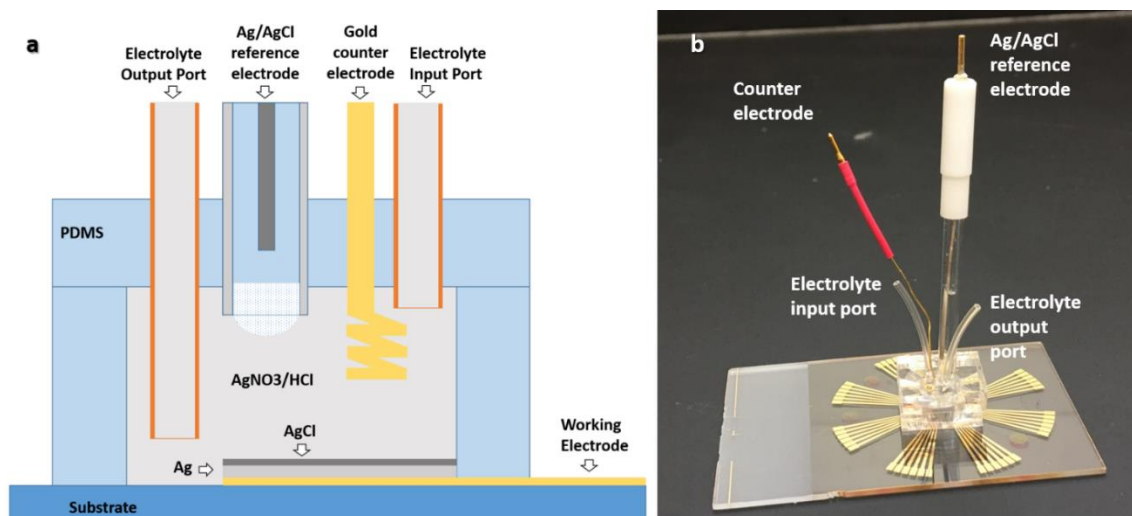


Figure 3.5 Schematic diagram (a) and experimental setup (b) for the fabrication of the Ag/AgCl pseudo-reference electrode.

in a Ag layer of around 5 μm in thickness. 0.1 M HCl solution was injected into the chamber after rinsing with DI water and the chloridization was driven at +0.2 mA for 60 s. After removing the electroplating chamber, the sample was rinsed with DI water.

The sample delivery channel was made of polydimethyl siloxane (PDMS) using soft lithography techniques. Due to the vulnerability of graphene, the conventional oxygen plasma cannot be used for the activation of the glass surface for PDMS bonding. As an alternative, the GFET chips were immersed in 0.1 M NaOH solution for 30 s and then rinsed with DI water with a layer of DI water left on the surface. The PDMS sample delivery channel was activated with oxygen plasma and then applied onto the GFET chip. The alignment of the sample delivery channel and the GFET chip was accomplished under microscope. The interfacial water layer serves as the lubricant and prevents the immediate bonding of glass and PDMS, while preserving their activity. The aligned sample was then placed in 60 $^{\circ}\text{C}$ oven for 3 h to allow the bonding.

3.2.3. Functionalization of the graphene channel for IgG detection

The functionalization process of the graphene surface for IgG detection is shown schematically in **Figure 3.6**. After rinsing the graphene surface with dimethyl sulfoxide (DMSO, VWR), 1-pyrenebutyric acid N-hydroxysuccinimide ester (PBASE, Sigma Aldrich, 10 mM dissolved in DMSO) was applied on the graphene surface and kept for 2 h. PBASE can be adsorbed on graphene

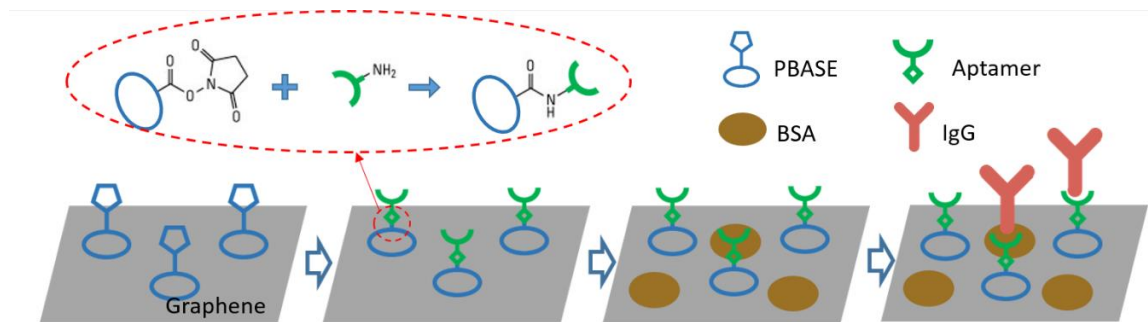


Figure 3.6 Schematics for the functionalization of the graphene channel for IgG detection. (Reprinted from [177])

through π - π interaction while causing no damage to its electrical properties and is widely used for the functionalization of graphene and carbon nanotubes [32]. After rinsing with DMSO, 5'-amino modified IgG aptamer (Base Pair Biotechnologies, 100 μ M in 1 \times PBS) was applied on the graphene surface and incubated for 3 h to allow the conjugation with PBASE. The conjugation is achieved by the amide bonding between the reactive N-hydroxysuccinimide (NHS) ester in PBASE and the amine group on the 5' end of the IgG aptamer. The remaining unconjugated sites were blocked by bovine serum albumin (BSA, 10% w/v in 1 \times PBS, Sigma Aldrich) after rinsing with 1 \times PBS. X-ray photoelectron spectroscopy (XPS) and Raman spectroscopy were performed to study the functionalization of the graphene surface (**see Appendix 1**). The transfer curves of the EGGFET biosensors were also measured after each step of functionalization.

Chapter 4. Characterization and Electrolytic Cleaning of PMMA Residues

Poly(methyl methacrylate) (PMMA) residue has long been a critical challenge for practical applications of the transferred chemical vapor deposited (CVD) graphene. Thermal annealing is empirically used for the removal of the PMMA residue; however, experiments imply that there are still residues left after thermal annealing which are difficult to remove with conventional methods. In this chapter, the thermal degradation of the PMMA residue upon annealing was studied by Raman spectroscopy. The study reveals that post-annealing residues are generated by the elimination of methoxycarbonyl side chains in PMMA and are believed to be absorbed on graphene via the π - π interaction between the conjugated unsaturated carbon segments and graphene. The post-annealing residues are difficult to remove by further annealing in a non-oxidative atmosphere due to their thermal and chemical stability. An electrolytic cleaning method was shown to be effective in removing these post-annealing residues while preserving the underlying graphene lattice. These studies provide a more in-depth understanding on the thermal annealing process for the removal of the PMMA residues from transferred CVD graphene and a new approach to remove the post-annealing residues, resulting in a residue-free graphene.

4.1. Introduction

Chemical vapor deposited (CVD) graphene has revealed tremendous potential as an important member of the graphene family since it was developed in 2009 [52]. It is particularly promising for commercialization due to its mass producibility and compatibility with microfabrication techniques. To enable its practical applications, CVD graphene must be transferred to insulating substrates from the metal substrates on which it is grown. A variety of methods have been developed for the transfer of CVD graphene over recent years. The PMMA-assisted method is one

the most promising methods for the industrial fabrication of graphene due to its capability of realizing large scale, low-cost and high quality of transferred graphene [64]. However, a major drawback of this method is that the PMMA residues are left on the transferred graphene, which has been a critical challenge that has hindered the applications of CVD graphene for a long time [63,136–138]. Studies indicate that the PMMA residues can cause degradation of the electronic properties of graphene, such as introducing p-type doping and carrier scattering [136,139]. The residues also can be detrimental for the applications of graphene in biosensors. For instance, PMMA residues can block the sensing surface of graphene-based biosensors, leading to the deterioration of the sensors' sensitivity and reliability [96,111]. Additionally, the PMMA residues can cause significant device-to-device variation [140].

Multiple approaches have been developed for the removal of the PMMA residues from the transferred CVD graphene. Some of them focus on reducing the formation of PMMA residues, such as isolating the graphene from the metal substrates by electrochemical delamination [141], abrogating all the heat-treatment before removing PMMA with solvents [68], etc. Efforts have also been directed to the removal of PMMA residues after transfer. Different solvents were used to dissolve PMMA, e.g., acetic acid [67,142], chloroform [64], etc. None of these methods can remove PMMA residue completely. Thermal annealing in a specific atmosphere is considered to be an effective way to reduce the PMMA residue and it has been empirically used [63,142].

Recent researches indicate that thermal annealing can result in the formation of post-annealing residues that are difficult to remove by annealing in non-oxidative atmosphere. Lin reported that these residues are the radicals generated by the random scission of PMMA that are covalently bonded with the defect sites on graphene [141]. The new broad Raman D and G peaks in annealed graphene has been reported to be amorphous carbon formed by carbonized PMMA residue [143].

Gong et al attributed these residues to the dehydrogenation of PMMA and proposed that thermal annealing in a carbon dioxide atmosphere could efficiently remove those residues [144]. However, annealing in oxidative atmosphere has the potential risk to damage the integrity of the graphene or to introduce defects [63,136,142,144].

In this chapter, we explore the formation mechanism of the post-annealing residues after the PMMA removal using the Raman spectrum of the transferred CVD graphene as a function of the annealing temperature and time. Based on the results, the formation mechanism and composition of the post-annealing residues are analyzed. To remove these post-annealing residues, an electrolytic method is tested. This method is shown to be an effective tool for removal of the residues based on the characterization using Raman spectroscopy and atomic force microscopy. The study provides a more in-depth understanding on the formation and composition of the post-annealing residues. The successful removal of the PMMA residue using the electrolytic cleaning is critical to obtain reliable working biosensors.

4.2. Experiments

The samples for the study on the PMMA residues and their removal is glass slides with transferred CVD graphene on them as shown in **Figure 4.1**. The preparation of the samples is introduced in Section 3.2.1. The Raman spectra were collected using a Renishaw InVia Raman microscope with a 532 nm laser of 100 mW. Raman mapping was achieved by collecting spectra over an area of $20\ \mu\text{m} \times 20\ \mu\text{m}$ with steps of $1\ \mu\text{m}$. The graphene surface was characterized with the Asylum MFP-3D atomic force microscope (AFM) using tapping mode.

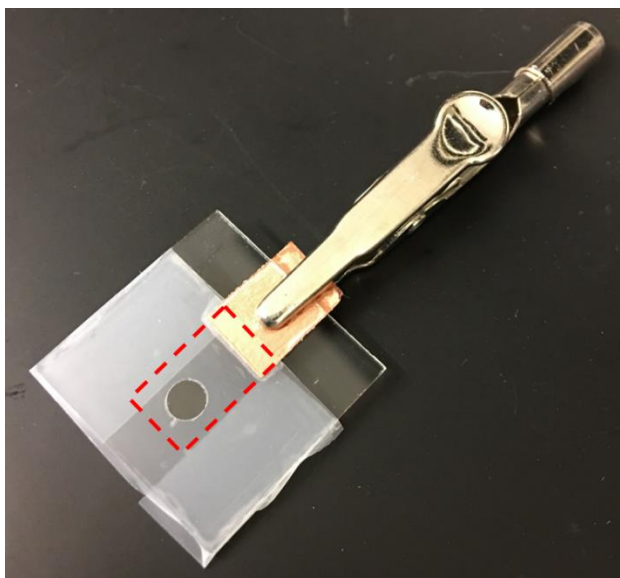


Figure 4.1 The samples for the study of the PMMA residues and the electrolytic cleaning. The red dashed box indicates the coverage of the transferred graphene

4.3. Degradation of PMMA residue upon thermal annealing

We studied the formation mechanism of the post-annealing residues using Raman spectroscopy by changing the annealing temperature and time [65]. Different from the transfer process described in Section 3.2.1, the PMMA/graphene films were baked on a hot plate at $200\ ^\circ\text{C}$ for 1 h before immersing in acetone. This prolonged heat treatment is intended to increase the amount of PMMA

residue for subsequent analysis [68]. The Raman spectra were collected at 10 points that were randomly selected on the graphene surface. **Figure 4.2** shows the evolution of the Raman spectra with respect to the annealing temperature. The main peak G at 1600 cm^{-1} corresponds to the E_{2g} phonon at Γ point arising from in-plane C-C stretching and the D peak at around 1350 cm^{-1} arises from the TO phonons near the Brillouin zone corner K that is activated by the defects [145]. During thermal annealing, as the temperature increases from $100\text{ }^{\circ}\text{C}$ to $200\text{ }^{\circ}\text{C}$, a new peak arises at 1590

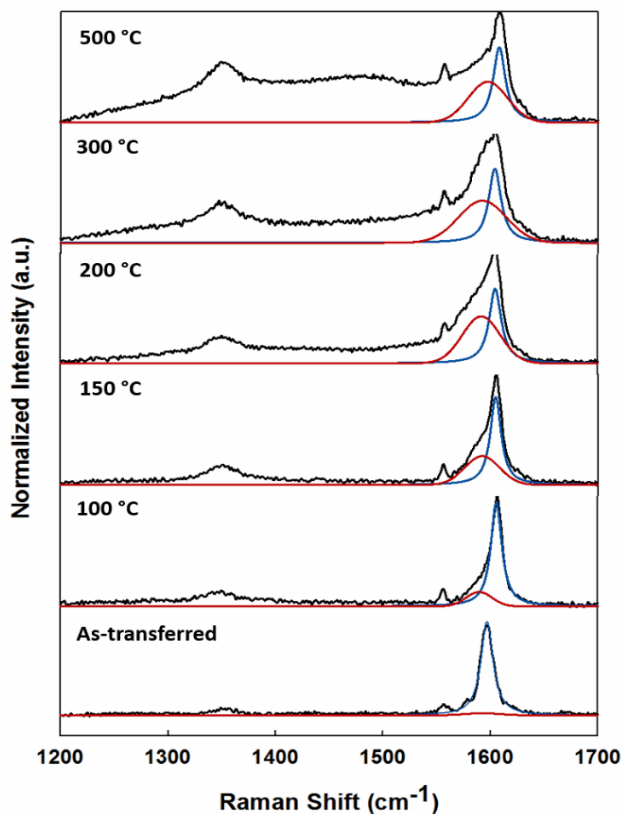


Figure 4.2 Evolution of the PMMA residue as a function of annealing temperature. Raman Spectra (black curves) of the as-transferred graphene after annealing in N_2 atmosphere for 1 h at $100\text{ }^{\circ}\text{C}$, $150\text{ }^{\circ}\text{C}$, $200\text{ }^{\circ}\text{C}$, $300\text{ }^{\circ}\text{C}$, and $500\text{ }^{\circ}\text{C}$. The blue and red fitting curves are attributed to the G peak of graphene and new peak at 1590 cm^{-1} , respectively. (Reprinted from [65])

cm^{-1} and a broad band ($1200\sim1550\text{ cm}^{-1}$) develops when further increasing the temperature. The G peak and new peak at 1590 cm^{-1} are fitted with Lorentzian and Gaussian shapes, respectively. The similar change of these new bands in the Raman spectrum of PMMA-transferred graphene upon thermal annealing has been previously reported [143,144,146]. These new bands cannot be removed by further increasing the annealing temperature and duration, indicating that a new type of carbon residues is left after the removal of PMMA residue by thermal annealing [144,146]. The new peak at 1590 cm^{-1} can be assigned to C=C stretching which normally lies in the range of $1500\sim1630\text{ cm}^{-1}$ [147]. During prolonged annealing at low temperature ($150\text{ }^{\circ}\text{C}$), we found that its intensity keeps increasing (**Figure 4.3**) while the new broad band at $1200\sim1550\text{ cm}^{-1}$ in **Figure**

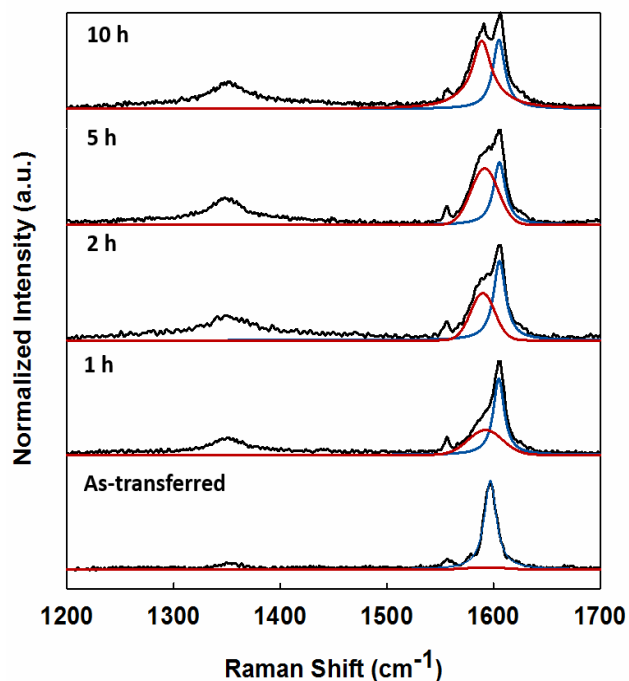


Figure 4.3 Raman spectra of the as-transferred graphene after annealing in a N₂ atmosphere at $150\text{ }^{\circ}\text{C}$ for 1 h, 2 h, 5 h, and 10 h, respectively. The blue and red fitting curves are attributed to the G peak of graphene and new peak at 1590 cm^{-1} , respectively. (Reprinted from [65])

4.2 does not appear. This suggests that some specific degradation mode of PMMA occurs at low temperature resulting in the continuous formation of C=C bonds. Previous studies indicate that the thermal degradation of PMMA leads to the formation of char by eliminating the methoxycarbonyl sidechains within it [148,149]. The infrared spectrum of the char exhibits a strong absorption band at 1550 cm^{-1} (**Figure 4.4**), suggesting the presence of conjugated unsaturated systems [148]. This band corresponds to the Raman peak at 1590 cm^{-1} in **Figure 4.2 and 4.3**. A similar Raman peak has been also reported but at a lower frequency [144], which might be due to the different environment for Raman spectra because the conjugating degree is decrease by oxidation and hydrogenation in an ambient air.

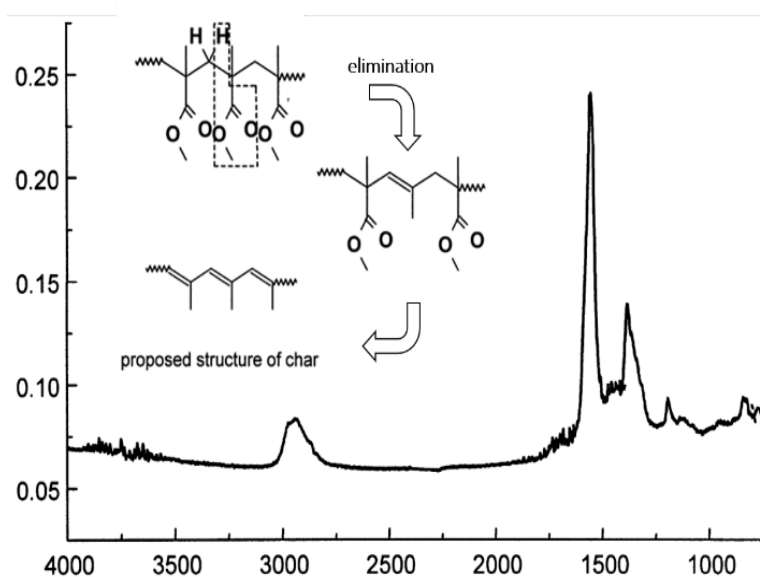


Figure 4.4 Infrared spectra of the PMMA char. The inset shows the elimination of the methoxycarbonyl side chains in PMMA and the formation of the conjugated systems. Reprinted form [148].

At a higher temperature, the depolymerization of PMMA is initiated by chain end and random chain scissions followed by depropagation. This char-forming mechanism interfere with the depolymerization process, generating carbon chains of varying lengths with randomly alternate

saturated and unsaturated carbon segments, which corresponds to the broad band at 1200~1500 cm^{-1} in **Figure 4.2**. The conjugated segments can bind non-covalently with graphene via π - π interaction and make these residues difficult to remove, resulting in the post-annealing residues. The π - π interaction can also cause the adherence of PMMA residue on graphene because the formation of these conjugated segments occurs at low temperature. It has been reported that better PMMA removal can be obtained by annealing in Ar/H₂ atmosphere [150], which is because H₂ eliminates the conjugated carbon systems by the hydrogenation of the C=C and thus weakens the absorption of the post-annealing residues on graphene.

In addition, reports have indicated that better PMMA removal can be achieved by reducing the annealing time, such as rapid thermal annealing [151] and laser irradiation [152], which is presumably due to the suppression of this abnormal degradation mechanism of PMMA. Studies have shown that alternating annealing in hydrogen and oxygen atmospheres can remove the PMMA residue substantially, which is attributed to oxygen cleavage of the C=C bonds [136,153]. These studies support our analysis on the formation and the composition of the post-annealing residues.

In summary, the special thermal degradation of PMMA, generating conjugated unsaturated carbon systems by the elimination of methoxycarbonyl side chain of PMMA, results in the formation of the post-annealed residues and its absorption on graphene.

4.4. Electrolytic cleaning of the post-annealing residues

To remove the post-annealing residues, we developed an electrolytic cleaning method which is shown to be an effective to remove the post-annealing residues. Electrolytic cleaning is a method that using electrochemically generated gas bubbles to strip off the contaminations from conductive surfaces [154]. It is typically used for the removal of rust and other contaminations from

conductive surfaces, such as cast iron. In recent years, defouling of conductive surfaces, such as graphite, carbon nanotube and stainless steel, etc., by electrochemically generated nanobubbles have been reported [155–157]. There are two modes of electrolytic cleaning: anodic electrocleaning and cathodic electrocleaning, in which oxygen and hydrogen are generated, respectively. Cathodic electrolytic cleaning provides higher efficiency for gas generation and avoids causing the oxidation of the graphene, and thus it was applied for the removal of the post-annealing residues on the transferred graphene in this work.

To study the reduction potential that is required for the removal of the post-annealing residues, the samples were cleaned at -1, -3 and -5 V versus Ag/AgCl for 1 h, and Raman spectra were collected at ten points that were randomly selected after each step. Because the broad band at 1200~1550 cm^{-1} which corresponds to the post-annealing residues was difficult to be fitted as a single peak, the intensity at 1480 cm^{-1} was selected as an indicator for the amount of the post-annealing residues.

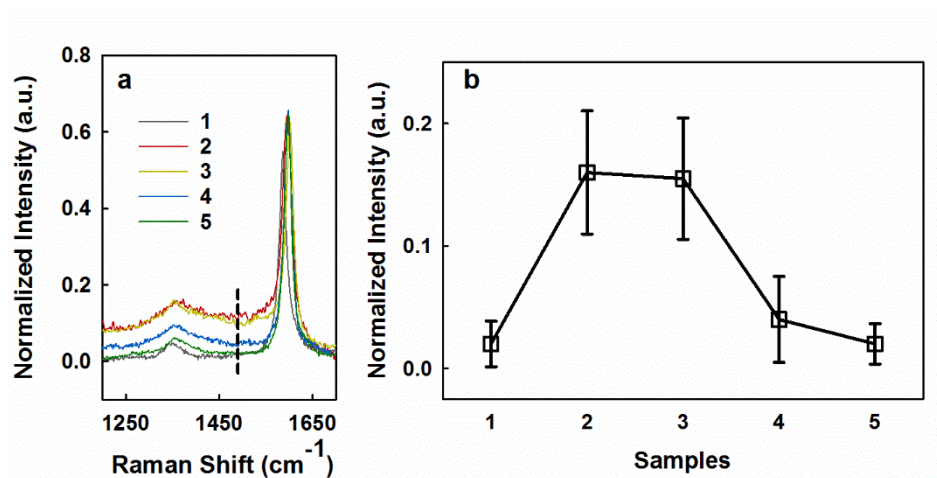


Figure 4.5 Raman spectroscopy study of the electrolytic cleaning at different reduction voltages.

a) Raman spectra and b) intensity at 1480 cm^{-1} of graphene that is 1) as-transferred, 2) after annealing in N_2 atmosphere at 250 $^{\circ}\text{C}$ for 3 h and after electrolytic cleaning at 3) -1 V, 4) -3 V and 5) -5 V vs Ag/AgCl in 0.5 M sulfuric acid for 1 h. (Reprinted from [65])

All spectra were normalized by setting the 2D peak intensity as one. As shown in **Figure 4.5**, after electrolytic cleaning at -1 V versus Ag/AgCl, no significant change of the Raman spectrum is observed; after electrolytic cleaning at -3 V versus Ag/AgCl, the broad band at 1200–1550 cm^{-1} and the peak at 1480 cm^{-1} are reduced, which indicates that the post-annealing residues are partially removed; after electrolytic cleaning at -5 V versus Ag/AgCl, the post-annealing residues have been effectively removed. The intensity ratio of the 2D and G peaks (I_{2D}/I_G) after electrolytic cleaning are around 1.5, indicating that there is no damage to the underlying graphene by the electrolytic cleaning. Other experiments show that the graphene remains intact at applied voltage up to -20 V vs Ag/AgCl.

We then studied the efficiency of the electrolytic cleaning by setting the potential at -5V vs Ag/AgCl and collecting the Raman spectrum after 10 min, 20 min, and 30 min. As shown in **Figure 4.6**, the residues are partially removed after 10 min and are almost completely removed after 20

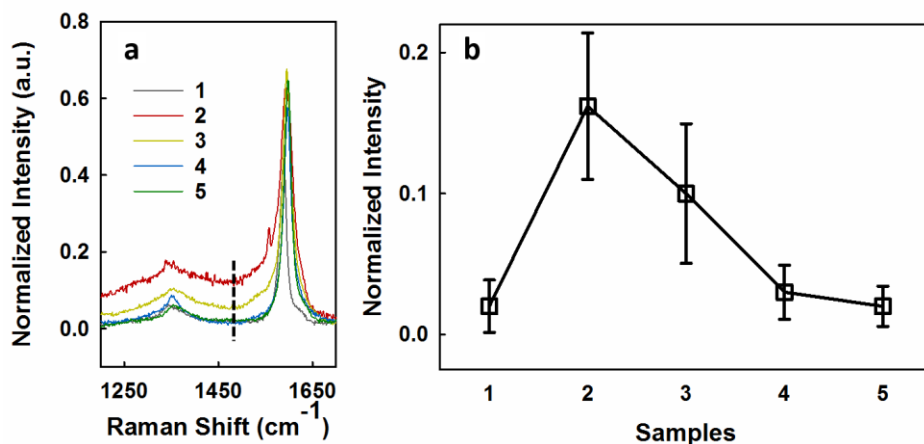


Figure 4.6 Raman spectroscopy study of the electrolytic cleaning as a functional of time. a) Raman spectra and b) intensity at 1480 cm^{-1} of graphene that is 1) as transferred, 2) after annealing in N_2 atmosphere at 250 $^{\circ}\text{C}$ for 3 h and after electrolytic cleaning at -5 V vs Ag/AgCl in 0.5 M sulfuric acid for 3) 10 min, 4) 20 min and 5) 30 min. (Reprinted from [65])

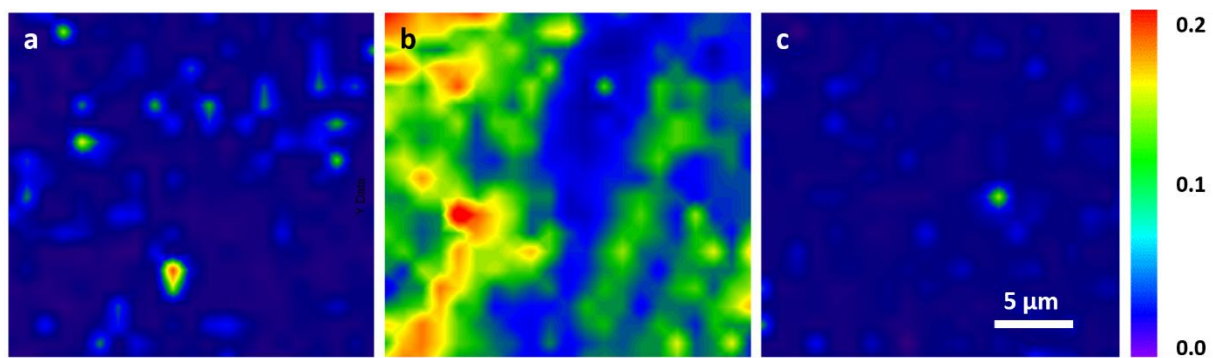


Figure 4.7 Raman mapping of the graphene that is a) as transferred, b) after thermal annealing in N_2 atmosphere at 250 °C for 3 h and c) after electrolytic cleaning at -5 V vs Ag/AgCl in 0.5 M sulfuric acid for 30 min. (Reprinted from [65])

min. It is worth noting that there was a redox couple at around +0.35 V vs Ag/AgCl which has reduced after electrolytic cleaning process. The origin of the redox couple and whether it is related with the post-annealing residues are still to be studied. One possible explanation is that the redox couple is the quinone-hydroquinone structure which was introduced during the thermal annealing process and electrochemically reduced during the electrolytic cleaning process.

Raman mapping was used to evaluate the efficiency of the electrolytic cleaning method. The maps of the Raman intensity at 1480 cm^{-1} of the graphene that is as-transferred, after annealing and after electrolytic cleaning are shown in **Figure 4.7**. A large amount of post-annealing residues was generated after thermal annealing, as indicated by the high intensity and are effectively removed after electrolytic cleaning. The peak position and intensity were also analyzed, and the histogram of the distributions are shown in **Figure 4.8**. The mean position of the G peak and 2D peak are both shifted positively after annealing and electrolytic cleaning. The blue shifts of the G peak and 2D peak, which suggest enhanced p-doping, were previously reported and attributed to the following reasons: (1) decomposition of PMMA residue; (2) oxygen and water absorption and (3) closer contact between graphene and the substrate [139,144,158]. I_{2D}/I_G reduced from around 1.9

to 1.6 after annealing but no further reduction occurred after electrolytic cleaning which suggests electrolytic cleaning causes no damage to the underlying graphene lattice.

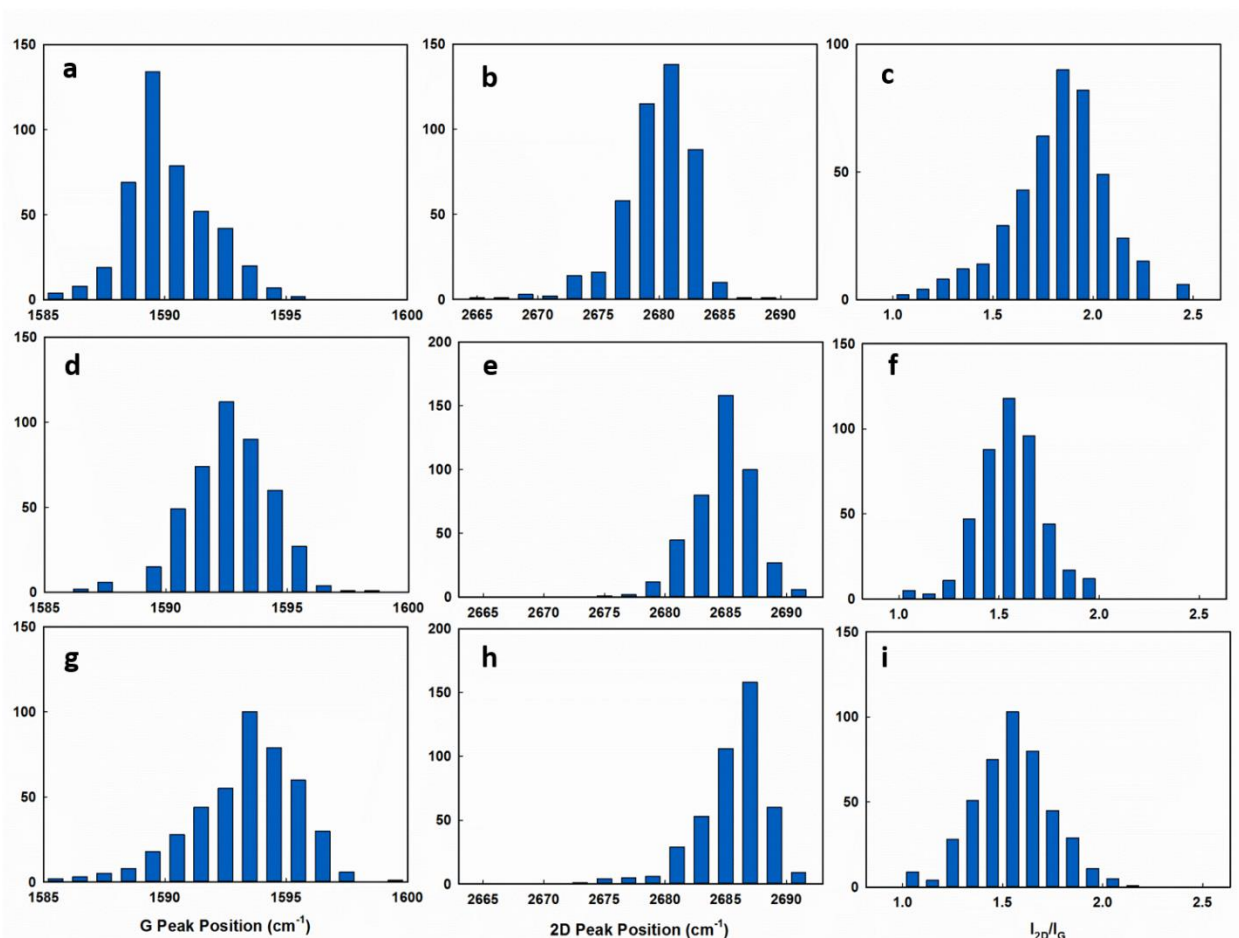


Figure 4.8 Histogram of G peak position, 2D peak position and I_{2D}/I_G of graphene that is a,b,c) as-transferred, d,e,f) after annealing in N_2 atmosphere at 250 °C for 3 hours and g,h,i) after electrolytic cleaning at -5 V vs Ag/AgCl in 0.5 M sulfuric acid for 3 hours. (Reprinted from [65])

The successful removal of the post-annealing residue was also confirmed by atomic force microscopy (AFM). As shown in **Figure 4.9**, the island-like PMMA residue is significantly eliminated after thermal annealing; however, there is still some flocculent residue left which cannot be removed by prolonged annealing. These residues exhibit lower height and a different morphology compared with the island-like PMMA residue on the as-transferred graphene. After

electrolytic cleaning, the flocculent residues disappear, and a clean, residue-free graphene is obtained. The surface roughness is significantly reduced after thermal annealing and further reduced after electrolytic cleaning.

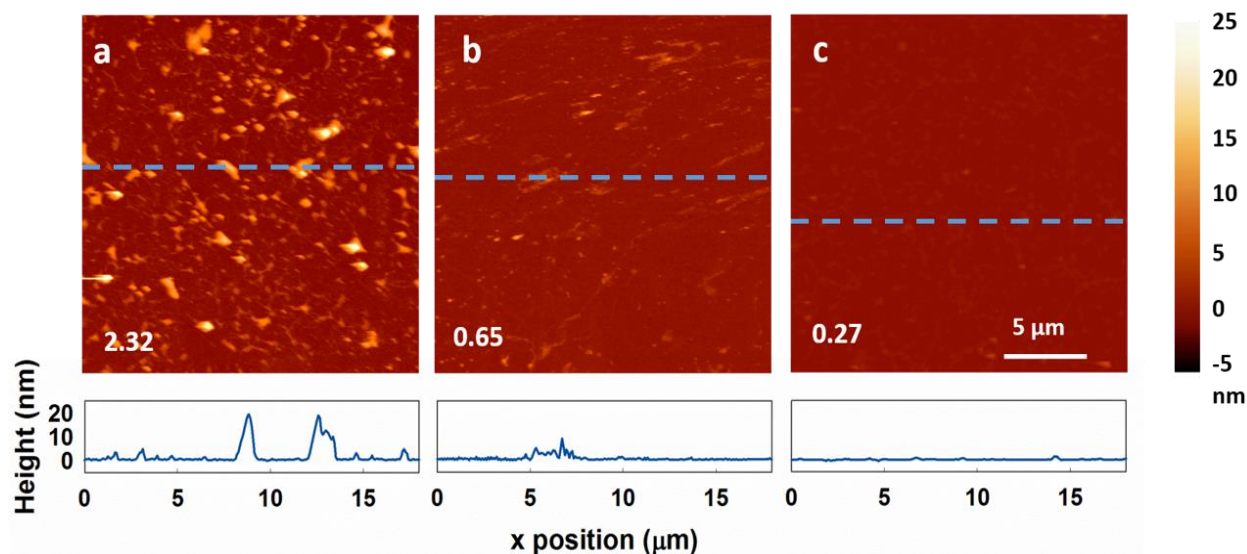


Figure 4.9 Characterization of thermal removal of the PMMA residues and electrolytic cleaning of the post-annealing residues. Representative AFM images of the graphene that is a) as transferred, b) after annealing in N₂ atmosphere at 250 °C for 3 h, and c) after electrolytic cleaning at -5 V vs Ag/AgCl in 0.5 M sulfuric acid for 30 min. The corresponding height profiles along the blue dashed line in the AFM images are shown in the bottom panel. The number in the left bottom of each image corresponds to the RMS roughness. (Reprinted from [65])

In addition to the mechanical stripping effect of the hydrogen bubbles, we speculate that the following mechanisms might also be contributing to the removal of the post-annealing residues: 1) weakening of the adsorption bonds such as π - π bonds due to the negative charging of graphene; 2) improved wetting of the graphene due to the negative charging so that water displaces weakly adsorbed residues [159].

4.5. Impact of PMMA residue removal on the transport properties of graphene

The studies on the transport properties of CVD graphene were performed using a EGGFET structure with a graphene channel of 1 mm in width and 0.1 mm in length. Typical transfer curves of the EGGFET that is as-transferred, after thermal annealing, and electrolytically cleaned are shown in **Figure 4.10A**. The gate voltages with the minimum conductivity (Dirac voltage) are shown in **Figure 4.10B**. To compare the transport parameters of the graphene, the electron mobility and hole mobility are derived symmetrically at the Dirac voltage ± 0.2 V as shown in **Figure 4.10C**. The interfacial capacitance, comprised of electrical double layer capacitance and quantum capacitance of graphene, was estimated to be around $1.8 \mu\text{F cm}^{-2}$ based on the model previously reported [31]. The results indicate that the as-transferred graphene is initially p-type doped, indicated by the positive Dirac voltages. Successive negative shifts of the Dirac voltage occur when graphene is thermally annealed and electrolytically cleaned as shown in **Figure 4.10B**. The carrier mobilities are increased from ~ 680 to $\sim 1200 \text{ cm}^2 \text{ V}^{-1} \text{ s}^{-1}$ after thermal annealing, and slightly increased to $\sim 1250 \text{ cm}^2 \text{ V}^{-1} \text{ s}^{-1}$ after electrolytic cleaning.

The electrical properties of doping in graphene can be affected by multiple factors. The p-type doping effects can be caused either by the silicon dioxide substrate [142,160,161] or PMMA [139,161], and the n-type doping effect can result from adsorbed water molecules in aqueous solutions [162,163]. In the as-transferred graphene, the PMMA residues introduce p-type doping and suppress the n-type doping effect of water, resulting in the overall p-type characteristics. The annealing process removes the PMMA residues, eliminating the p-type doping effect, and exposing graphene to water molecules leading to n-type doping. All of these processes result in the negative shift of the Dirac voltage. The electrolytic cleaning removes the post-annealing residues and causes the Dirac point to shift further near 0 V, indicating that the post-annealing

residues are also a p-type dopant for graphene. The p-type doping effect of the post-annealing residues is attributed to the charge transfer between graphene and the conjugated systems [164].

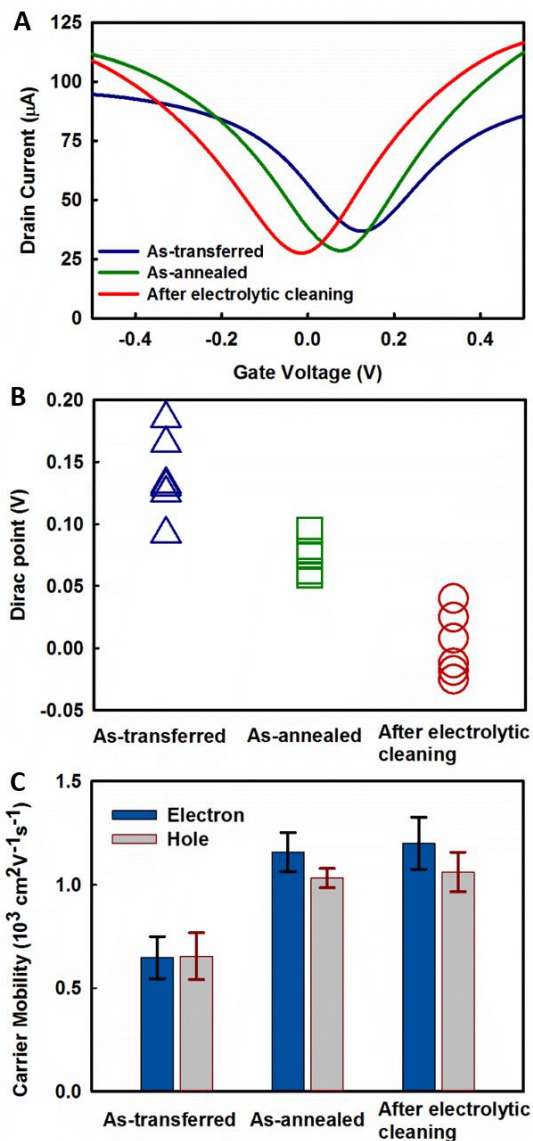


Figure 4.10 (a) Representative transfer curves, (b) Dirac voltage distribution, and (c) electron and hole mobilities derived of the graphene based SGFET that is as-transferred, after annealing in a N_2 atmosphere at 250°C for 3 h and after electrolytic cleaning at -5 V versus Ag/AgCl in 0.5M sulfuric acid for 30 min. The error bars correspond to the standard error in (b). Reprinted from [65].

The negative shift of the Dirac point, which suggests a reduced p-doping, is in controversy with the blue shifts of the G and 2D peaks in Raman spectra as mentioned previously. This is because the Raman spectroscopy was performed in air ambient where oxygen absorption introduces strong p-doping, while in SGFET the oxygen absorption and its p-doping effect are screened by water. Our results suggest that oxygen is a strong p-dopant while water has no doping effect or weak n-doping effect for graphene. Upon annealing, the carrier mobilities are significantly improved, indicating that the scattering effect of PMMA residues on graphene have been reduced or eliminated [139]. Furthermore, the removal of the post-annealing residues leads to a slight increasing in the carrier mobilities, suggesting that the scattering effect of the post-annealing residue are very weak. The carrier mobilities we obtained are at the same level as the values reported for graphene on silicon dioxide substrates, on which the carrier mobilities of graphene are mainly limited by the charged impurity scattering from silicon dioxide [160,165].

4.6. Conclusion

The formation of the post-annealing residues on PMMA-transferred CVD graphene was studied by Raman spectra and an electrolytic cleaning method was used to remove these post-annealing residues successfully. The changes of the Raman spectrum of the CVD graphene transferred with PMMA during thermal annealing reveals the formation of the post-annealing residues: the elimination of the methoxycarbonyl side chain in PMMA leads to the formation of conjugated unsaturated carbon systems, as indicated by the Raman peak at 1590 cm^{-1} . Additionally, carbon chains of varying lengths with randomly alternate saturated and unsaturated segments, corresponding to the broad band at $1200\text{--}1550\text{ cm}^{-1}$ in the Raman spectrum, are generated because of the depolymerization of PMMA during thermal annealing. These carbon residues are absorbed on graphene via $\pi\text{--}\pi$ interactions and are difficult to remove by further annealing. Transport

properties measurements with a SGFET structure indicate that the PMMA residues introduce both p-type doping and carrier scattering to the transferred CVD graphene. The post-annealing residues are also a source for p-type doping due to the charge transfer between graphene and the conjugated systems. The scattering by the post-annealing residue is much weaker compared with PMMA residue.

For practical uses of CVD graphene, it is of critical importance to remove the post-annealing residues to get a clean surface. The electrolytic method reported in this paper is shown to be effective in removing the post-annealing residues while preserving the underlying graphene lattice. This method is easy to implement and can be performed with simple equipment such as a DC power supply. In addition, the electrochemical method could also be used for the removal of many other contaminants, such as absorbed oxygen (by electrochemical reduction) and organic molecules (by cathodic stripping). Therefore, we suggest the electrochemical cleaning as an effective method for the deep-cleaning and surface-restoration of graphene.

Chapter 5. Detection of IgG using EGGFET biosensor

In this chapter, the performance of the developed EGGFET biosensor is demonstrated by the detection of human immunoglobulin G (IgG). Continuous negative shift of the transfer curve of the EGGFET biosensor was observed upon the successive addition of IgG with increasing concentrations. The detection of IgG is attributed to the modulation of the Fermi level in the graphene caused by the adsorption of the positively charged IgG molecules. The real-time detection of IgG is demonstrated by the change of the drain current at a fixed gate voltage. The selectivity of the EGGFET is studied by measuring the drain current change upon the addition of the interfering antibodies, including human immunoglobulin M (IgM) and human immunoglobulin A (IgA).

5.1. Introduction

Immunoglobulin G (IgG) is the main type of antibody found in blood and extracellular fluid and play an important role in the immune systems. IgG molecules are made of amino acids which make them generally charged [166]. The basic amino acid terminals, e.g. lysine, glutamine, asparagine, exhibit positive charges, whereas acidic amino acids residues, e.g. glutamic acid, aspartic acid, exhibit negative charges. The overall charge of a protein molecule is determined by its isoelectric point (pI) and the pH of the solution. When the pH is lower than its pI, the protein is positively charged; when the pH is higher than its pI, the protein is negatively charged. The charges of proteins play an important role in their structure formation and functioning [166,167] and can be used for the analysis of proteins, such as charge-induced chromatography and mass spectroscopy [168–170]. There are four IgG subclasses (IgG1, IgG2, IgG3 and IgG4) in human blood and IgG1 is the most abundant. IgG antibodies are large molecules of about 150 kDa made of four peptide chains: two large heavy chains and two small light chains. The Y-shaped IgG consists of two

antigen-binding fragments (Fab) for specific binding with antigen and a crystallizable fragment (Fc). Both fragments are heavily decorated with lysine groups [171]. The abundant amino terminals make the pI of the IgG fall in the range of 8.7-9.1 [172] which makes IgG positively charged in physiological pH of around 7.4.

In general, EGGFET biosensors operate by measuring the conductance change of the channel induced by the binding of the target molecules on it. The successful triggering of the conductance change is the key for its operation. Depending on the properties of the target molecules, different mechanisms can be employed, such as electron transfer [104], scattering, Schottky barrier modulation between carbon materials and metal electrodes [173] and electrostatic gating [174–176]. The charges on the IgG molecules provide opportunity for their detection with FET biosensors by electrostatic gating. The detection of IgG with EGGFET biosensors is based on the modulation of the Fermi level in the graphene channel by electrostatic gating upon the specific

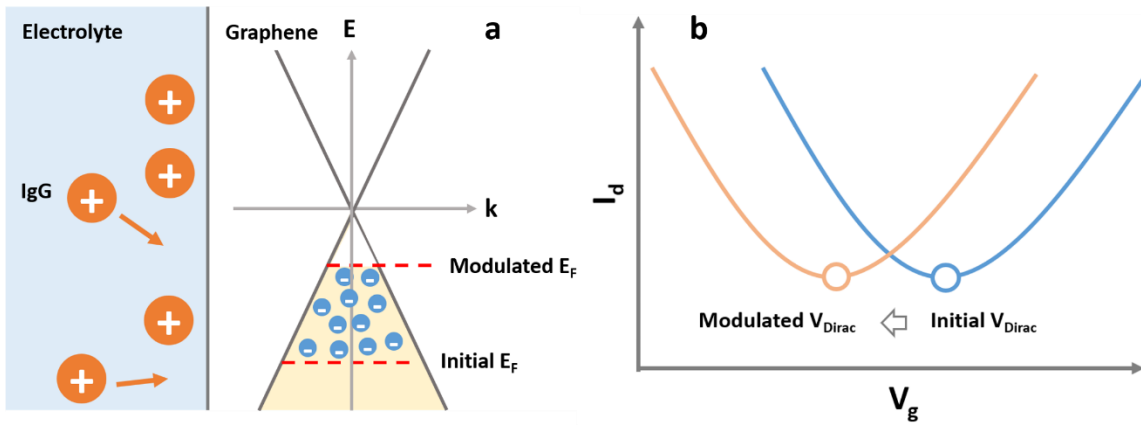


Figure 5.1 Operation principle of the EGGFET biosensor for IgG detection. (a) the modulation of the Fermi level in the graphene channel upon the adsorption of IgG molecules. (b) the negative shift of the transfer curve upon the adsorption of the IgG molecules. (Reprinted from [177]).

adsorption of the positively charged IgG molecules [177]. Owing to the low density of states at

low energy level, the Fermi level in graphene is very sensitive to the change of the carrier density, which can be modulated by the adsorption of the charged molecules. As shown in **Figure 5.1**, the specific binding of the positively charged IgG molecules will cause the accumulation of the electrons in the graphene channel, resulting in the positive shift of the Fermi level.

The transfer curve measurement allows us to locate the Fermi level. Graphene is a zero-bandgap semiconductor with the conduction band and the valance band meeting at the Dirac points with linear energy dispersion. The transfer curves of the EGGFET biosensors exhibit unique ambipolar electrical field effect behavior. As shown in **Figure 5.1**, the minimum conductivity is obtained when the Fermi level of graphene coincides with the Dirac point and the corresponding gate voltage (V_g) can be used for parameterizing the Fermi level of graphene [178]. This gate voltage is generally referred as Dirac voltage (V_{Dirac}) [179–181]. The shift of the Dirac voltage can thereby be used for the quantification of the IgG.

In this chapter, we present a proof-of-concept study on the detection of the human IgG using the EGGFET biosensor. The performance of the EGGFET biosensor is demonstrated by the detection of IgG in two different operation modes: transfer curve measurement and continuous drain current measurement. The selectivity of the EGGFET is studied by measuring the drain current change upon the addition of the interfering antibodies, including human immunoglobulin M (IgM) and human immunoglobulin A (IgA).

5.2. Experiments

The EGGFET biosensor used for IgG detection is shown in **Figure 5.2**. It consists of five parallel graphene channels. A PDMS well with an opening of 5 mm in diameter was applied on the chip for the confinement of the samples. A standard Ag/AgCl reference electrode embedded in a PDMS stamp was used as the gate. **Figure 5.2b** shows the enlarged view of the graphene channel, which

is 150 μm in length and 75 μm in width. The graphene channel was functionalized with IgG aptamer for the specific detection of human IgG. The fabrication and functionalization processes are given in Section 3.2.

The electrical measurement was conducted using a Keithley 4200 Semiconductor Characterization System (SCS) which consists of two source measure units (SMU). The experiment setup for IgG detection is schematically shown in **Figure 5.2c**. The gate voltage was applied using SMU2 and the drain current was measured by SMU1. For the transfer curve measurement, the gate voltage was swept from +0.1 V to +0.3V with steps of 1 mV and scan rate of 10 mV/s. The source-to-drain voltage was set to be 10 mV. For the continuous drain current measurement, the gate voltage was set to be 0 V and the source-to-drain voltage was set to be 10 mV.

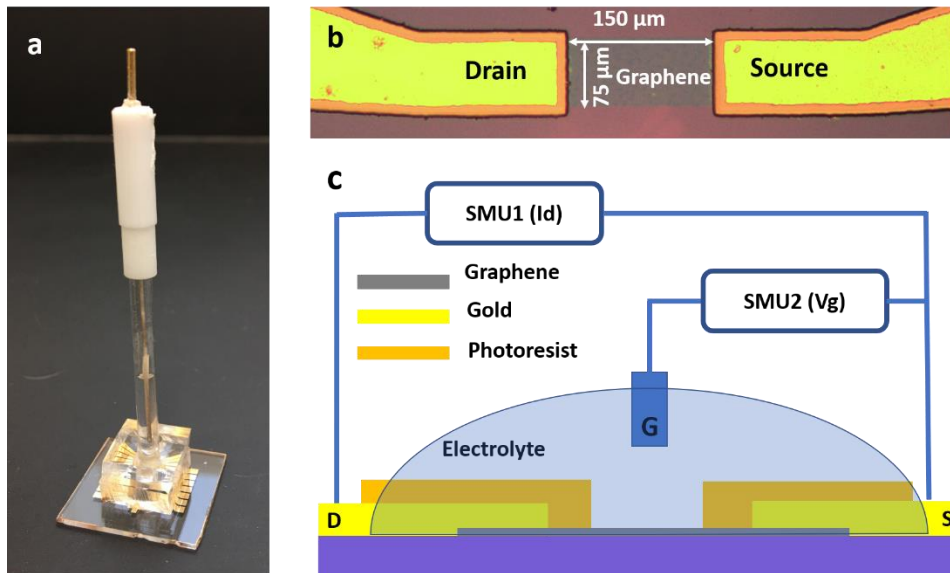


Figure 5.2 Device and experimental setup for IgG detection. (a) The EGGFET biosensor integrated with a standard Ag/AgCl reference electrode and a PDMS well for sample containing. (b) The enlarged view of the graphene channel. (c) The schematic diagram of the circuit connection for the detection of IgG using EGGFET biosensor.

5.3. Detection of IgG using EGGFET biosensor

To test the response of the EGGFET biosensors, the device was incubated in human IgG (dissolved in $1\times$ PBS) with different concentrations for 10 min successively. After each incubation, the chamber was rinsed with $0.01\times$ PBS and filled with $0.01\times$ PBS for transfer curve measurement. As shown in **Figure 5.3**, continuous negative shift of the transfer curve was observed as the concentration of the IgG increases. We extracted the Dirac voltage V_{Dirac} based on the linear regression analysis of the V_g vs the slope of the transfer curves (see Appendix 2 for details). As mentioned above, the shift of the V_{Dirac} can be used for the quantitative analysis of the measurement results. The response of the EGGFET biosensor is plotted with respect to the IgG concentrations as shown in **Figure 5.3b**. The plots are fitted with the Hill-Langmuir equation

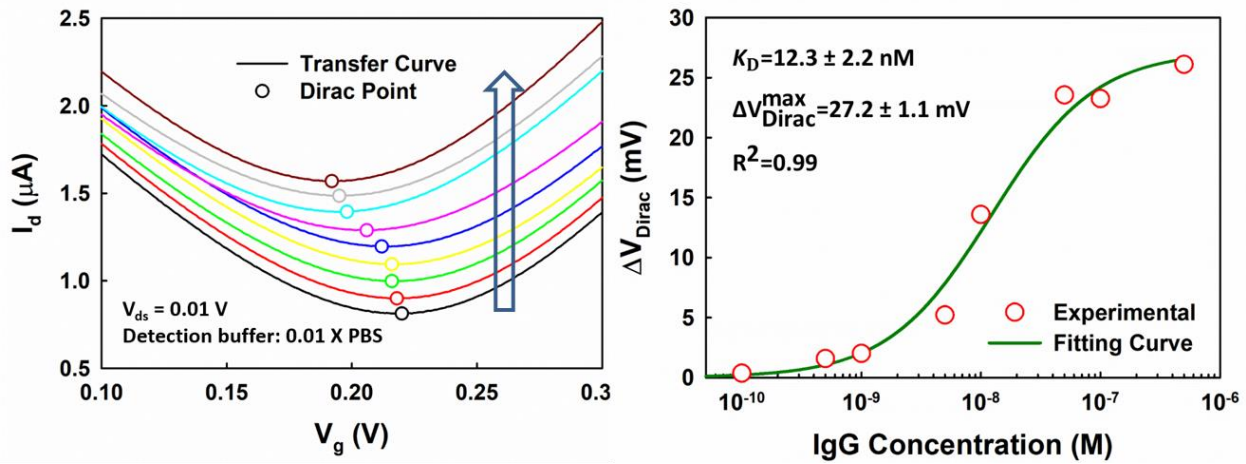


Figure 5.3 The responses of an EGGFET immunosensor to IgG. a) The continuous shifts of the transfer curves of the EGGEFT immunosensor upon the addition of IgG with different concentrations (0, 0.1, 0.5, 1.0, 5.0, 10, 50, 100, 500 nM). The transfer curves are stacked vertically with offsets of 0.1 μA with the arrow indicating the increasing of IgG concentrations. b) ΔV_{Dirac} with respect to the concentrations of IgG. The uncertainties of the fitting parameters indicate the standard errors of the estimates for the fitting. (Reprinted from [177]).

$$\Delta V_{Dirac} = \Delta V_{Dirac}^{max} \times \frac{[IgG]}{[IgG] + K_D} \quad (5-1)$$

in which K_D is the dissociation constant of the aptamer-IgG complex. The Hill-Langmuir equation is commonly used in biochemistry to estimate the binding equilibrium in ligand-receptor interaction. In its original form

$$\theta = \frac{[L]^n}{[L]^n + K_D} \quad (5-2)$$

where θ represents the fraction of the receptor sites that have been bound to the ligand; $[L]$ is the concentration of the ligands and K_D is the apparent dissociation constant derived from the law of mass action, which is equal to the ratio of the dissociation rate of the ligand-receptor complex to its association rate; n is the Hill coefficient which describes the cooperativity between ligands. The fitting indicates that the linear relation between ΔV_{Dirac} and the occupation ratio θ of the binding sites. The fitting yields K_D of 12.3 nM which is higher than the value provided by the manufacturer (8.4 nM) which can be attributed to the depressed on-rate caused by the spatial orientation of the aptamer. ΔV_{Dirac}^{max} represents the maximum response of the EGGFET biosensor and is estimated to be 27.2 mV for the device being tested. To evaluate the cooperativity between

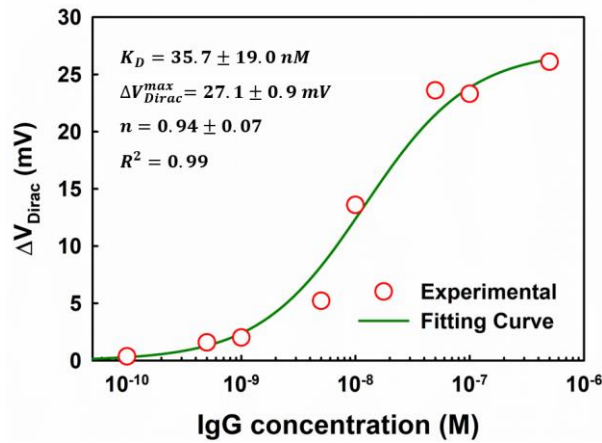


Figure 5.4 The response of the EGGFET biosensor to IgG and its fitting using the full Hill equation.

the IgG molecules, we also used the original Hill equation (equation 5-2) to fit the measured results (**Figure 5.4**). The Hill coefficient is fitted to be 0.94, which suggests a negatively cooperative binding.

The response of the EGGFET biosensor to IgG was also tested by the continuous monitoring of the drain current at a fixed gate voltage. In this case, IgG dissolved in 0.01× PBS with different concentrations were added into the detection chamber and the drain current was monitored continuously. As shown in **Figure 5.5a**, continuous decrease of the drain current was observed upon the addition of the IgG. The results are in agreement with the transfer curve measurement and previous results [182]. The decrease of the drain current is attributed to the negative shift of the transfer curves. The change of the drain current can also be well fitted with the Hill-Langmuir equation which generates a maximum response of 0.123 μA and a dissociation constant K_D of 9.6 nM.

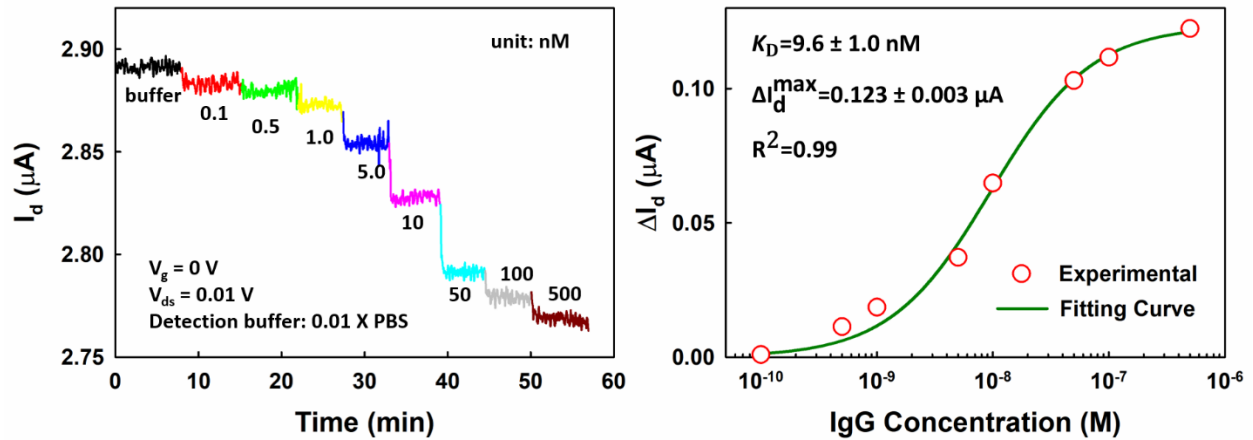


Figure 5.5 The real-time measurement of IgG using the EGGFET immunosensor. (a) The change of I_d upon successive addition of IgG with increasing concentrations from 0.1 nM to 500 nM. (b) ΔI_d with respect to the concentrations of IgG. The uncertainties of the fitting parameters indicate the standard errors of the estimates for the fitting. (Reprinted from [177]).

5.4. Selectivity of the EGGFET biosensor

Selectivity is an important benchmark for biosensors which indicates the ability of a biosensor to measure the concentration of the analytes in presence of other interfering substances. To test the selectivity, we measured the response of the EGGFET biosensor to human immunoglobulin A (IgA) and human immunoglobulin M (IgM). IgA and IgM are possible interfering substances existing in human blood. As shown in **Figure 5.6**, no significant drain current change was observed upon the addition of IgA and IgM; while significant decrease of the drain current occurred upon the addition of IgG. The results suggest the good selectivity of the EGGFET biosensor for IgG detection.

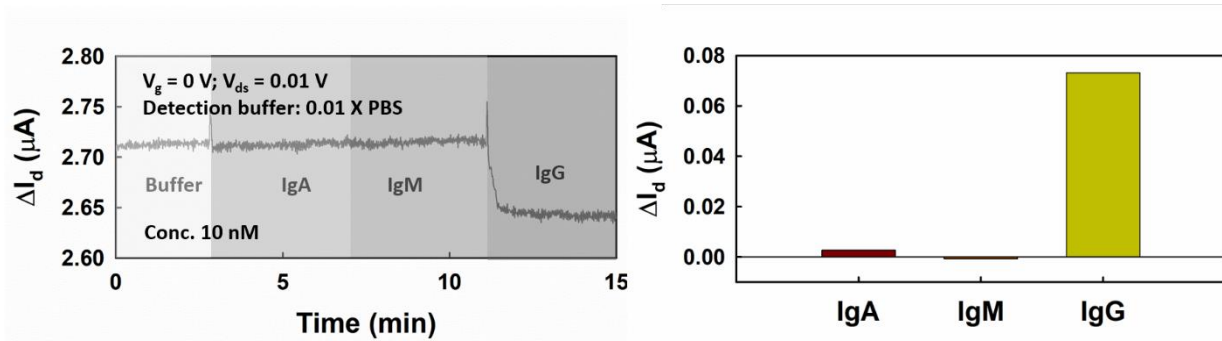


Figure 5.6 The selectivity of the EGGFET immunosensor for IgG detection. (a) Responses of the EGGFET immunosensor to the successive addition of IgA, IgM and IgG. (b) ΔI_d of the EGGFET immunosensor as responses to IgA, IgM and IgG. (Reprinted from [177]).

5.5. Conclusion

The performance of the EGGFET biosensor is demonstrated by the detection of human IgG. Upon the adsorption of the positively charged IgG, the Fermi level in the graphene channel is modulated by the electrostatic gating effect which causes the negative shift of the transfer curves. The shift of the Dirac voltage can thereby be used for the quantitative measurement of IgG. Based on the operation principle, the EGGFET biosensor is also capable for real-time for IgG detection by

monitoring the drain current change at a fixed gate voltage. The selectivity of the EGGFET biosensor is tested by measuring the drain current change upon the addition of the possible interfering antibodies, human IgA and IgM.

It's worth noting that in this proof-of-concept study, the IgG was measured in pure PBS buffer. However, the real samples, e.g. human blood, serum and plasma, are much more complex which might introduce biofouling to the measurement results. Although the EGGFET biosensor is promising for real-time detection, the variation of the sample matrices might cause significant uncertainty or even false. This point must be considered for the practical applications of the EGGFET biosensors.

Chapter 6. Matrix Effect Study and Immunoassay Detection Using EGGFET biosensor

In this chapter, we study the electrolyte matrix effects, including its composition, pH and ionic strength, and demonstrate that the variations of the electrolyte matrices have a significant impact on the Fermi level of the graphene channel and the sensitivity of the EGGFET biosensors. It is attributed to the polarization-induced interaction between the electrolyte and the graphene at the interface which can lead to considerable modulation of the Fermi level of the graphene channel. As a result, the response of the EGGFET biosensors is susceptible to the matrix effect which might lead to high uncertainty or even false results. Then an EGGFET immunoassay is presented for allowing well regulation over the matrix effect. The multichannel design allows in-situ calibration with negative control, as well as the statistical validation of the measurement results. The detection range is estimated to be around 2-50 nM with a coefficient of variation (CV) of less than 20% and the recovery rate for IgG detection from serum is around 85~95%. The limit of detection (LOD) is estimated to be around 0.7 nM. Compared with traditional immunoassay techniques, the EGGFET immunoassay is label-free, and ready to be integrated with microfluidics sensor platforms, suggesting its great prospect for point-of-care applications.

6.1. Introduction

Significant progress has been made on the development of the electrolyte-gated graphene field effect transistor (EGGFET) biosensors during the last decade [22]. Various targeting analytes were demonstrated for detection, including nucleic acids [80], proteins [92], metabolites [102] and other biologically relevant analytes [104]. The EGGFET biosensors have shown sensitivity as low as attomolar and high selectivity toward target biomolecules [183]. EGGFET biosensors have also been applied for electrophysiological measurements due to the high spatial resolution and low

noise level, such as the detection of electrical activity of electrogenic cells [184,185]. Efforts have been taken to overcome the Debye screening effect which is one of the main factors that limit the sensitivity of EGGFET biosensors [94,120,122]. Other strategies were also applied to further improve their performance, such as gold nanoparticle decoration [186]. In addition, the rapid development of the preparation techniques of graphene also contributes to the maturing of the EGGFET biosensor and makes it a latecomer outperforming SiNW and CNT on performance and mass producibility [33,34].

Despite outstanding performance have been reported, most results were based on experiments using simplified samples in laboratory setting [19,22]. In EGGFET biosensors, the graphene channels are in direct exposure to the electrolytes, which might be variant in composition, concentration and pH, etc. These variables might originate from the sample themselves and the sample handling processes and affect the operation of the EGGFET biosensors. For example, the pH of human blood is normally regulated between 7.35 and 7.45; but many conditions and diseases can interfere with the pH control and cause the blood pH to fall outside of the healthy limits, such as acidosis and alkalosis [187]. During the actual measurement, the samples are often diluted to make the analyte level fall within the detection range of the biosensors, which may also change the electrolyte matrix composition. Furthermore, in EGGFET biosensors, the gate voltage is applied on the electrolytes and the electrical double layer (EDL) at the electrolyte-graphene interface serves as the gate dielectric, therefore it's of critical importance to study if and how the variance in the electrolytes would affect the operation of the EGGFET biosensors. Till now, detailed understanding on the electrolyte-graphene interaction and its impact on the electronic transport in graphene are still lacking [19], while critical for the design and operation of the EGGFET biosensors, especially for their practical applications.

In this chapter, we studied the impact of the variance in the electrolytes on the EGGFET biosensors, namely matrix effect, by varying the composition, ionic strength and pH of the electrolytes. The underlying mechanisms were discussed with regarding to the strong polarization-induced interaction between the electrolytes and the graphene and its impact on the Fermi level of the graphene channel. The influence of the matrix effect on the gate potential and the sensitivity of the EGGFET biosensors was also studied. For the regulation of the matrix effect, we present an immunoassay based on the EGGFET immunosensors. The performance was demonstrated by the successful detection of human immunoglobulin G (IgG) from serum by spike-and-recovery experiments.

6.2. Experiments

6.2.1. Design of the EGGFET immunoassay

A prototype of the EGGFET immunoassay chip and an enlarged view of the EGGFET immunosensor configuration are shown in **Figure 6.1a and b**, respectively. The chip consists of 7 immunosensor sets that are distributed in a circular form, including five sets (number 1-5) for calibration curve (standards) measurement, one (number 6) for sample measurement, and one (number 7) for negative control. A common ring-like Ag/AgCl pseudo-reference electrode works as the gate (G). Each immunosensor set consists of 5 EGGFET immunosensors, which allows the statistical validation of the measurement results. The dimension of the graphene channels is $150\ \mu\text{m} \times 75\ \mu\text{m}$. The sample-delivery channels are filled with red food dye for demonstration.

6.2.2. Electrical measurement

The electrical measurements were conducted using Keithley 4200 SCS and a Micromanipulator probe station. The experiment setup is shown in **Figure 5.1**. For the operation of using the EGGFET immunoassay for IgG detection, the operation parameters, including the gate voltage scan rate, gate voltage setting and drain-source voltage, were optimized to minimize the hysteresis-induced deviation and maximize the transconductance (see Appendix 3). The data were collected by measuring the five parallel channels in each immunosensor set and the results were obtained by the statistical analysis of the measured results. The open circuit potential (OCP) of the Ag/AgCl pseudo-reference electrode with respect to the standard Ag/AgCl reference electrode (CHI111, CH Instruments, Inc.) was measured using a Gamry Interface 1000T potentiostat.

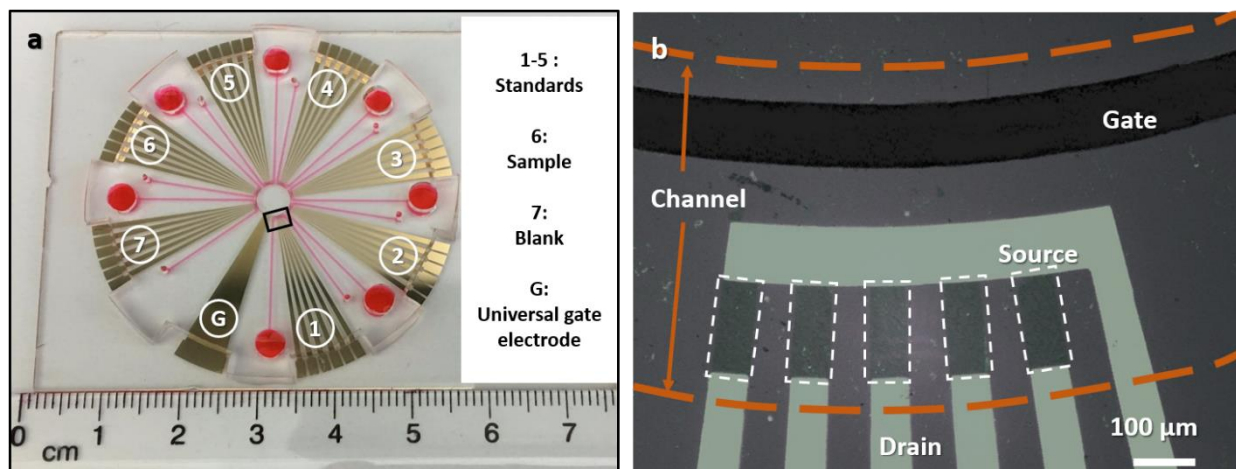


Figure 6.1 EGGFET immunoassay chip. (a) The prototype of the EGGFET immunoassay chip with the sample delivery channels filled with red food dye. The numbers indicate the 7 immunosensor sets with their function assignment as specified on the right. (b) An enlarged view of the EGGFET immunosensor set that was fabricated on SiO_2/Si substrate for the visualization of graphene (as indicated by the white dashed frames). The sample delivery channel is indicated by the brown dashed line. (Reprinted from [177]).

6.3. Matrix effect on the EGGFET biosensor

6.3.1. Matrix effect on the V_{Dirac} of the EGGFET biosensors

In EGGFET biosensors, the graphene channels are directly exposed to the electrolytes, which makes it important to learn if and how the electrolytes would affect the operation of the EGGFET biosensors. The electrolyte matrices for bioanalysis are highly variant and complex, to better understand the underlying mechanisms, we chose several simple electrolytes and studied the matrix effect as a function of the composition, pH and ionic strength. In this study, we focus on the matrix effect on the V_{Dirac} of the EGGFET which is directly related with its biosensing applications.

We measured the transfer curves of a set of EGGFET biosensors in different electrolytes using a standard Ag/AgCl reference electrode as the gate and the V_{Dirac} were extracted from the transfer curves based on the linear regression analysis of the V_g vs the slope of the transfer curves (see Appendix 2). As shown in **Figure 6.2a**, the V_{Dirac} of the EGGFET biosensors exhibit a strong dependence on the composition of the electrolytes. In particular, the V_{Dirac} of the EGGFET in potassium salt electrolytes are lower than those in the corresponding sodium salt electrolytes of the same concentration. The ion-specific dependence was also reported in Heller's report that claims Li^+ shows stronger electrostatic gating effect than K^+ [188]. Our result is in accordance with a simulation which took into account the polarization of both the graphene and the ions at the graphene-electrolyte interface and suggests that K^+ ion are more strongly absorbed onto the graphene than Na^+ ions [189]. Because both K^+ and Na^+ have one positive charge, the stronger adsorption of K^+ , which leads to a higher surface charge density on graphene, will introduce stronger n-doping in the graphene channel due to the electrostatic gating effect. The stronger n-doping effect of K^+ compared with Na^+ is further verified by the measurement of the V_{Dirac} of the

EGGFET in the mixture of NaCl and KCl solutions with different ratios. As shown in **Figure 6.2b**, the V_{Dirac} shifts negatively as the ratio of the KCl increases. In addition, the EGGFET exhibits different V_{Dirac} in NaCl, NaNO₃ and Na₂SO₄ (all containing 1 M Na⁺), respectively, suggesting that the V_{Dirac} of the EGGFET is also dependent on the type of anions.

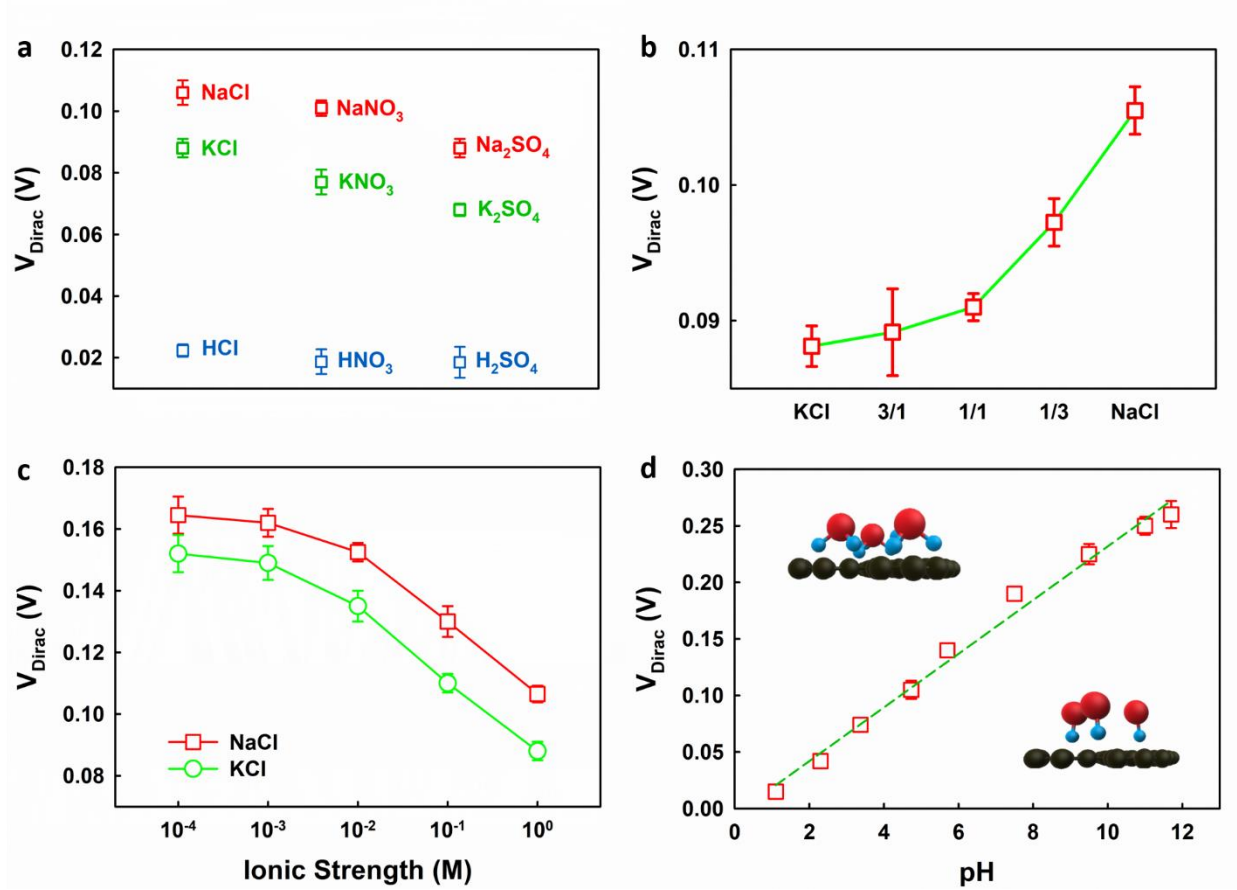


Figure 6.2 The V_{Dirac} of the EGGFET biosensors in (a) different electrolytes (all concentrations are 1 M except for Na₂SO₄, K₂SO₄ and H₂SO₄, which are 0.5 M); (b) mixture of KCl (1 M) and NaCl (1 M) with different mixing ratios (horizontal axis); (c) NaCl and KCl solution with different ionic strength and (d) KCl solution (1 M) that was titrated with different pH. The schematics in (d) show the possible orientation of the H₃O⁺ and OH⁻ on the graphene. The error bars indicate the standard deviation of the measured results of the five parallel channels. (Reprinted from [177]).

More significantly negative shift of the V_{Dirac} was observed when acids were used as the electrolytes (**Figure 6.2a**). We further extended the pH range of the electrolyte by titrating HCl (0.1 M, in 1 M KCl) with KOH (0.1 M, in 1 M KCl). The titration allows us to adjust the pH of the electrolytes while keeping the ionic strength relatively constant. The pH was monitored using a Hach pocket pro pH tester. Linear positive shift of the V_{Dirac} with respect to the pH was observed as shown in **Figure 6.2d**. The result is consistent with previous reports that proposed the application of EGGFET as pH sensors [92,113]. The pH dependence of the V_{Dirac} suggests the strong adsorption of the hydronium and hydroxide ions on graphene and their n-doping and p-doping effects, respectively. In addition to the ion- π interaction which leads to the enhanced adsorption of H_3O^+ and OH^- on graphene as discussed above, the dipole- π interaction might be a more important contributing factor [190]. Studies indicate that polar molecules tend to orient in the direction normal to the graphene with strength sufficient to overcome thermal effects [191]. Due to the strong adsorption of these polar ions, the continuous transition from the n-doping H_3O^+ to p-doping OH^- causes the continuous positive shift of V_{Dirac} as the pH increases.

Additionally, the transfer characteristics of the EGGFET were studied in electrolytes with different ionic strength. NaCl and KCl solutions with different ionic strengths were prepared by successive 10-fold dilution of the stock solutions (1 M). The ionic strengths were calculated according to $I = c(M)$ for monovalent salts, $c(M)$ represents the molar concentration. As shown in **Figure 6.2c**, the increase of the ionic strength causes the negative shift of the V_{Dirac} , which is in agreement with previous report [188]. Because the overall doping effect of the electrolytes is determined by the competitive adsorption of the cations and the anions, the result indicates that Na^+ and K^+ surpass Cl^- in the capability of doping graphene and reveals the significant impact of the ions in the electrolytes on the transfer characteristics of the EGGFET. It's worth noting in Chen's paper

[192,193], the negative shift of the V_{Dirac} is attributed to the dielectric screening of the charged impurities on the underlying SiO_2 substrate by the dissolved ions. This explanation is based on the observed transconductance improvement of the EGGFET as the concentration of the electrolyte increases. However, no significant change of the transconductance was observed in our experiments and some other papers [188,194,195]. As shown in **Figure 6.3**, the transconductance of the EGGFET is almost the same in KCl solution over a wide concentration range. Therefore, we speculate that the negative shift of the transfer curve is caused by the adsorption of the cations on the graphene, rather than the dielectric screening of the charged impurities. Our speculation can also well explain the observed ion-specific gating effect of different electrolytes.

6.3.2. Matrix effect on the potential of the gate electrode

For the application in the EGGFET biosensors, standard Ag/AgCl reference electrode is preferred due to its well-defined potential. However, standard Ag/AgCl reference electrodes are difficult to be miniaturized and integrated with microfluidics devices. Ag/AgCl pseudo-reference electrode is

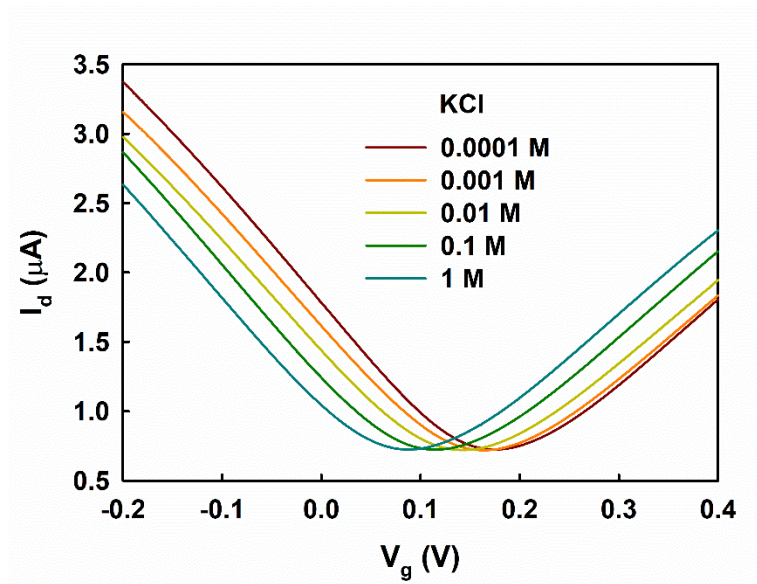


Figure 6.3 The transfer curves of the EGGFET in KCl with different concentrations

an alternative because its fabrication is compatible with the microfabrication techniques [196]. In EGGFET, the real gate voltage that modulates the graphene channel is the voltage across the electrical double layer (EDL) [31], and the potential of the reference electrode must be considered for the determination of the V_{Dirac} . The potential distribution in EGGFET with Ag/AgCl reference electrode is shown in **Figure 6.4a** and can be described as equation 6-1:

$$V_{\text{gating}} = V_{\text{Ag/AgCl}} - V_{\text{gs}} \quad (6-1)$$

in which V_{gating} is the potential across the EDL, V_{gs} is the applied gate-to-source voltage, $V_{\text{Ag/AgCl}}$ is the potential of the Ag/AgCl electrode versus the electrolyte. Different from the standard Ag/AgCl reference electrode, the potential of Ag/AgCl pseudo-reference electrode is not fixed but determined by the composition of the electrolytes. In PBS, the potential of Ag/AgCl pseudo-reference electrode can be estimated by the activity of the Cl^- using the Nernst equation 6-2:

$$E_{\text{Ag/AgCl}} = E_{\text{Ag/AgCl}}^0 - \frac{RT}{F} \ln(a_{\text{Cl}^-}) \quad (6-2)$$

in which $E_{\text{Ag/AgCl}}^0$ is the standard potential, R is the universal gas constant, T is the temperature in kelvins, F is the Faraday's constant, a_{Cl^-} is the activity of Cl^- . We measured the V_{Dirac} of the EGGFET biosensors with a Ag/AgCl pseudo-reference electrode as the gate and the open circuit potential (OCP) of the Ag/AgCl pseudo-reference electrode with respect to the standard Ag/AgCl reference electrode in PBS with different dilution factors. As shown in **Figure 6.4b**, the OCP of the Ag/AgCl pseudo-reference electrode decreases as the concentration of the PBS increases;

comparatively, the V_{Dirac} also shift downwards but with a larger amplitude and the difference can be attributed to the matrix effects of the electrolyte on graphene as discussed above.

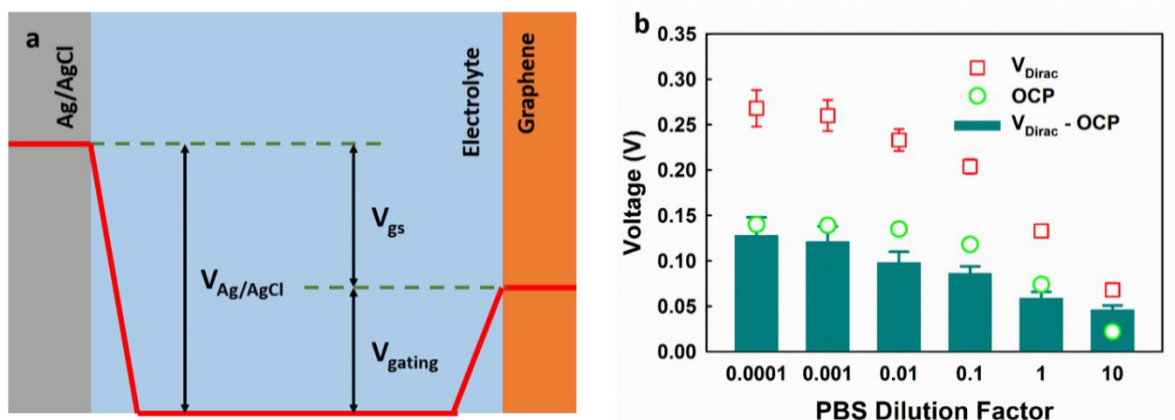


Figure 6.4 The impact of the gate electrode potential on EGGFET biosensors. (a) The potential distribution in EGGFET biosensors. (b) The V_{Dirac} of the EGGFET biosensors with Ag/AgCl pseudo-reference electrode as the gate in different PBS diluents and the OCP between the Ag/AgCl pseudo-reference electrode and the standard Ag/AgCl reference electrode. The error bars indicate the standard deviation of the measurement results of the five parallel channels. (Reprinted from [177]).

6.3.3. Matrix effect on the sensitivity of the EGGFET biosensors

In electrolytes, the electrostatic effect of charges is screened by the attraction of the opposite charges and the specific orientation of the dipoles around them. Debye length, which is dependent on the ionic strength of the electrolyte, is normally used to characterize the distance of the electrostatic effects' persistence. The sensitivity of the FET biosensors is significantly limited by the Debye screening effect [116]. **Figure 6.5a** shows the responses of one EGGFET immunosensor to IgG in PBS with different dilution factors. In $1\times$ PBS, no significant response was observed because the Debye length (around 0.7 nm) is smaller than the height of the functional layer (the linker + the receptor). As the concentration of PBS decreases, the charged molecules exhibit

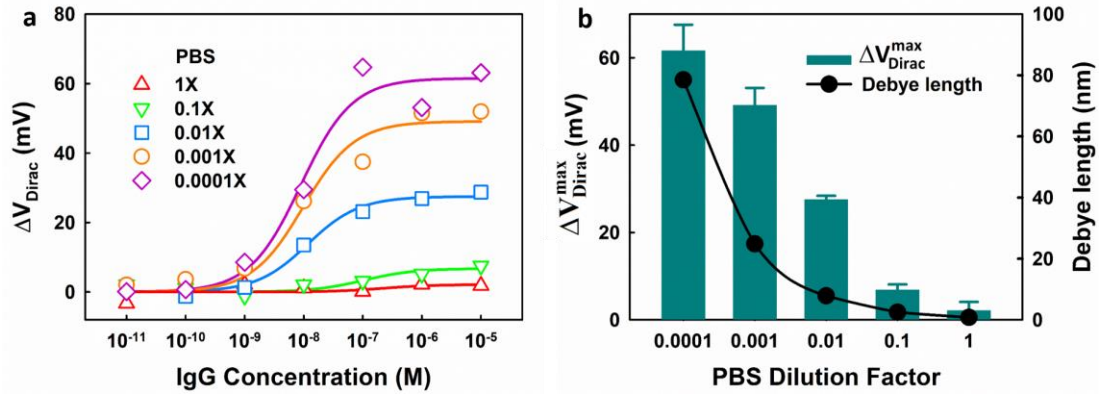


Figure 6.5 The impact of the ionic strength on the sensitivity of an EGGFET biosensor. (a) The response of the EGGFET biosensor to IgG under different diluents; (b) The maximum response ($\Delta V_{\text{Dirac}}^{\text{max}}$) of the EGGFET biosensor in different PBS diluents and the corresponding Debye length. The error bars indicate the standard errors of the estimates for the fitting. (Reprinted from [177]).

stronger modulation capability as the Debye length increases and thus stronger response can be obtained. As shown in **Figure 6.5b**, the $\Delta V_{\text{Dirac}}^{\text{max}}$ under different ionic strength are plotted in comparison with the corresponding Debye length which was calculated by equation (3),

$$\delta = \sqrt{\frac{\epsilon k T}{2 e^2 N_A C}} \quad (6-3)$$

in which ϵ is the permittivity of the electrolyte, k is the Boltzman constant, T is the temperature in kelvins, e is the elementary charge, N_A is the Avogadro number and C is the concentration of the electrolytes in mol/m^3 . The results indicate that the Debye lengths are highly dependent on the ionic strength of the electrolytes, resulting a strong impact on the sensitivity of the EGGFET biosensors.

As shown in **Figure 6.5**, higher sensitivity could be obtained with PBS with lower concentrations; however, the low concentration also introduces significant uncertainties, possibly due to 1) the

high resistance of the electrolytes of low concentrations which makes the voltage between the reference electrode and the graphene unstable; 2) the fluctuation of the potential of the Ag/AgCl pseudo-reference electrode when the concentration of Cl^- is low as discussed in section 6.3.2. The results show that $0.01\times$ PBS provides the best performance which compromises the sensitivity and measurement uncertainty.

6.4. EGGFET immunoassay

6.4.1. Standard Operation Protocol of the EGGFET immunoassay

As discussed in the previous section, the EGGFET biosensors are intrinsically sensitive to the variation of the electrolyte matrices. The matrix effect has to be properly taken into account when using EGGFET biosensor for real sample measurement. To allow the regulation of the matrix effect and obtain reliable test results, we developed a standard operation protocol of the EGGFET immunoassay as shown in **Figure 6.6**. For a better understanding of the operation of the EGGFET immunoassay, several terms used in this paper are clarified in the following: 1) the detection buffer is the electrolyte in which the transfer curves of the immunosensors are measured, 2) the washing buffer is the solution to rinse the channel and remove the nonspecifically adsorbed biomolecules.

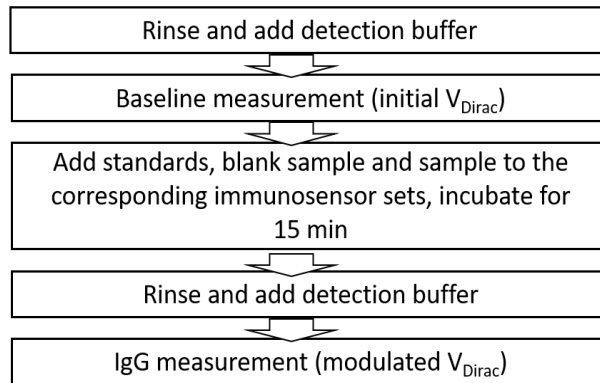


Figure 6.6 Standard operation protocol of the EGGFET immunoassay for IgG measurement. (Reprinted from [177]).

In this work, 0.01× phosphate buffer saline (PBS) was used as the detection buffer and washing buffer during the experiment unless specified otherwise.

The operation protocol of the EGGFET immunoassay is described as the following. (1) The 7 immunosensor sets were filled with detection buffer after rinsing with washing buffer for 3 times. (2) The transfer curves of the EGGFET immunosensors were measured and the initial V_{Dirac} were extracted. (3) The EGGFET immunosensors were incubated with standards, blank solution and sample for 30 minutes, according to the function assignment as shown in **Figure 6.1a**. 4) The immunosensors were rinsed with washing buffer for 3 times and then filled with detection buffer. 5) The transfer curves of the EGGFET immunosensors were measured and the modulated V_{Dirac} were extracted). We hereby emphasize the V_{Dirac} are measured in the detection buffers instead of the original samples to minimize or exclude the effect caused by the sample matrices.

6.4.2. Spike-and-recovery test

Spike-and-recovery test was used for examining the performance of the EGGFET immunoassay. The standards were prepared by dissolving human IgG (essentially salt-free, lyophilized powder, Sigma Aldrich) in 1× PBS to specific concentrations; goat serum (Sigma Aldrich) was used as the blank sample for negative control; the samples to be measured were prepared by spiking goat serum with human IgG with specific concentrations (2 nM, 5 nM, 20 nM, 50 nM, 100 nM). Following the protocol as mentioned above, the initial and modulated V_{Dirac} of EGGFET immunosensors before and after IgG binding were measured and ΔV_{Dirac} were calculated. The measured results are shown in **Figure 6.7a**. The calibration curve was obtained by fitting the responses to the standards using the Hill-Langmuir equation, and the IgG concentration of the sample was calculated based on the calibration curve. The fitting parameters and the measured concentrations of IgG are summarized in **Table 6.1**.

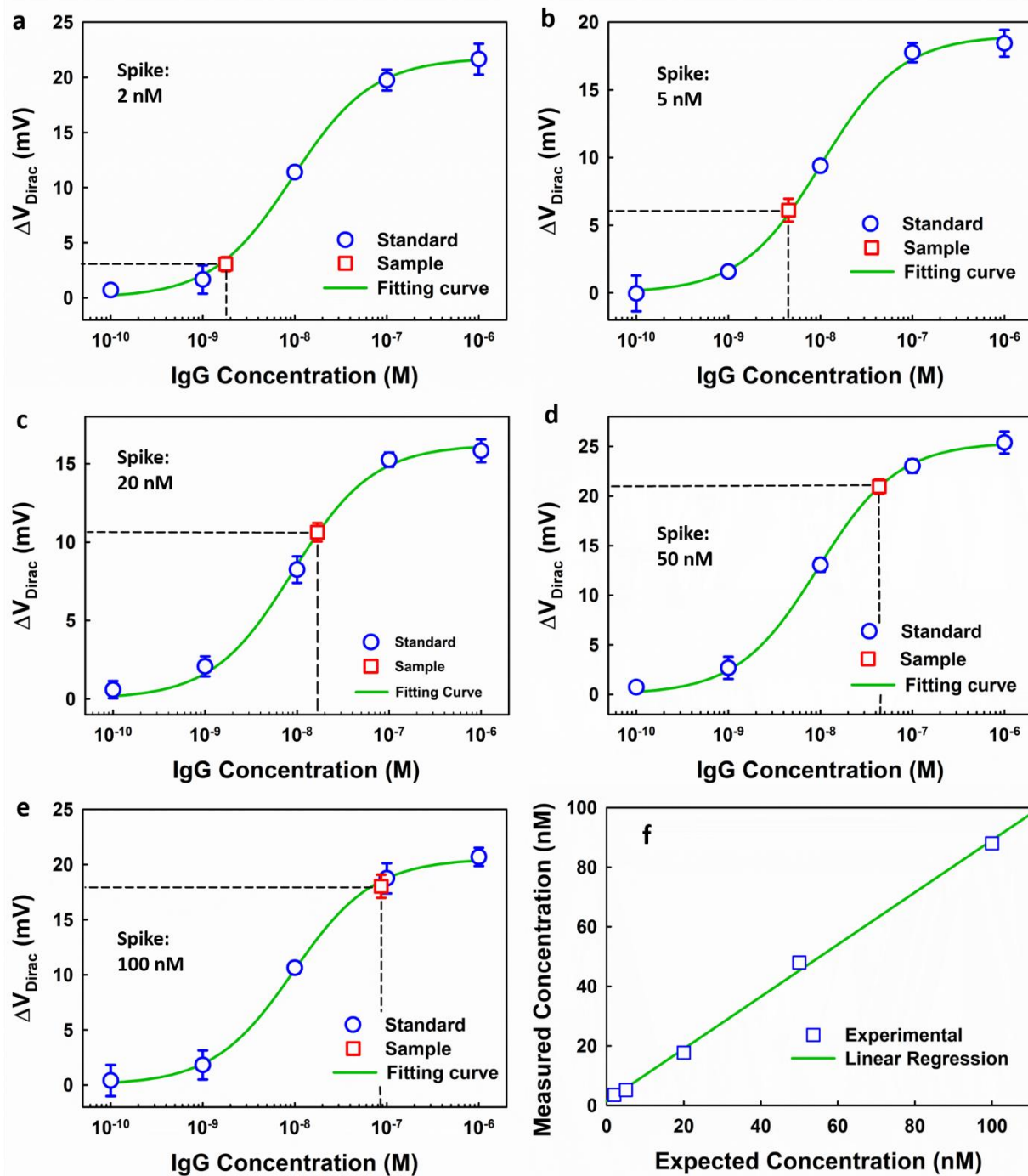


Figure 6.7 Evaluation of the EGGFET immunoassay. (a) The spike-and-recovery test of the EGGFET immunoassay for IgG detection. The error bars refer to the standard deviations of measurement results of the five parallel channels. (b) The linearity-of-dilution assessment of the EGGFET immunoassay.

Table 6-1 Summary of the fitting parameters and the measured results

Device	Spike	Measured	Recovery	$\Delta V_{\text{Dirac}}^{\text{max}}$	K_D	R^2
	nM	nM		mV	nM	
1	2	2.13	1.07	21.7	9.39	0.99
2	5	5.16	1.03	19.0	10.24	0.99
3	20	17.7	0.86	16.22	8.95	0.98
4	50	48.0	0.96	25.44	9.40	0.99
5	100	88.6	0.89	20.55	9.65	0.99

Based on the results, (1) for all the five tests, the measured results of the standards can be well fitted with the Hill-Langmuir equation, which suggests the biosensors on a single chip exhibit high uniformity in the sensitivity. The good fitting allows us to calculate the concentration of the target IgG with high confidence. (2) Satisfactory recovery rates (0.86~1.07) were obtained which suggests the immunoassay can be used for the IgG detection from complex physiological samples. The reliability of the EGGFET immunoassay was further verified by the linearity-of-dilution assessment. As shown in **Figure 6.7f**, the measured concentrations are plotted with respect to the spike concentrations. The good linearity indicates that the matrix effects have been well regulated. Reproducible results can be achieved with a satisfactory recovery rate, suggesting the feasibility of the EGGFET immunoassay for IgG detection from serum. The discrepancy between the measured results and the actual concentrations might be attributed to the constituent difference between standards and samples and can be reduced by optimizing the composition of the standards matrix. (3) There's a significant variability between different chips. For example, the maximum Dirac voltage shift $\Delta V_{\text{Dirac}}^{\text{max}}$ varies from 16.22 mV (Device 3) to 25.44 mV (Device 5). In our

experiment, we found this “chip-to-chip” variation always exist but the performance of the biosensors that are fabricated on the same chip exhibits high uniformity. This significant “chip-to-chip” variation might originate from a) the variation in the quality of the graphene being used and b) the device fabrication process. For the biosensors that are fabricated on the same chips, they were made of the same piece of graphene and went through the same fabrication process and thus exhibit relatively high uniformity. Our immunoassay takes advantage of this point and integrates the self-calibration capability, showing great potential for practical applications. The limit of detection (LOD) is estimated to be around 0.7 nM based on the measurement results and the detection range is estimated to be around 2~50 nM with a coefficient of variation (CV) of less than 20% (see Appendix 4).

We compared our immunoassay with other biosensors that have been reported for IgG detection. The development of the biosensors typically bases on the demonstrative detection of an example target and the performance of the biosensors is highly dependent on the structures and properties of targets. It is meaningless to compare the results based on different targets. For example, the detection of DNA using FET biosensors is much more efficient than the detection of the proteins due to the higher affinity between matched DNA chains and more charges on the DNA backbones. Here the biosensors that have been reported for the detection of the human immunoglobulin G (IgG) are summarized in **Table 6-2** for comparison.

Table 6-2 Summary of the biosensors for IgG detection

Ref.	Method	Detection range (M)	LOD (M)	Label free	Sample
[197]	SPR	N/A	3.7×10^{-10}	Yes	Plasma
[198]	SPR	$1.3 \sim 6.7 \times 10^{-8}$	N/A	Yes	PBS
[199]	SPR	$1 \times 10^{-10} \sim 6.67 \times 10^{-8}$	5.3×10^{-7}	Yes	Milk
[200]	Optical	$1.3 \sim 6.7 \times 10^{-5}$	1.3×10^{-5}	No	Blood
[201]	Interferometer	$5 \times 10^{-9} \sim 2 \times 10^{-7}$	3.1×10^{-9}	Yes	Serum
[202]	Interferometer	$2.7 \times 10^{-10} \sim 3.0 \times 10^{-8}$	2.7×10^{-10}	Yes	PBS
[203]	OMR	$1.7 \times 10^{-10} \sim 2.73 \times 10^{-9}$	1.7×10^{-10}	Yes	PBS
[204]	EIS	$6.7 \times 10^{-14} \sim 6.7 \times 10^{-11}$	6.7×10^{-14}	Yes	PBS
[205]	EIS	$6.7 \times 10^{-11} \sim 6.7 \times 10^{-9}$	3.3×10^{-11}	Yes	PBS
[206]	Amperometry	$2.6 \times 10^{-9} \sim 1.3 \times 10^{-7}$	1.3×10^{-9}	No	Milk
[86]	CNT-FET	$7 \times 10^{-15} \sim 7 \times 10^{-13}$	7×10^{-15}	Yes	PBS
[207]	TRGO-FET	$1.3 \times 10^{-12} \sim 1.3 \times 10^{-6}$	1.3×10^{-12}	Yes	PBS
This work	EGGFET	$2 \times 10^{-9} \sim 5 \times 10^{-8}$	7×10^{-10}	Yes	Serum

Abbreviation: EIS: electrochemical impedance spectroscopy; OMR: optical micro-ring resonator; SPR: surface plasmon resonance; TRGO: thermal reduced graphene oxide; CNT: carbon nanotube; PBS: phosphate buffered saline. Note: some units were transferred to molar using IgG molecular weight of 150kDa.

Comparing with other biosensors and other techniques, the merits of our immunoassay reside in

(1) The label-free detection capability. Comparing with other bioanalysis techniques, such as the widely used ELISA, our biosensor is label-free and could significantly simplify the operation procedures.

(2) It's based on electrical measurement and doesn't rely on complicated supporting equipment. Comparing with other biosensors, such as SPR, OMR and interferometer, the signal of our biosensor can be directly read using a simple electrical measurement device. Therefore, our biosensor and immunoassay are ready to be integrated with the portable electrical measurement device and is highly promising for point-of-care biomedical applications.

(3) The capability for analyzing real physiological samples. The performance of the biosensors is mainly challenged by the capability to deal with complex physiological samples. Currently, the reports on the FET-based biosensors are mostly proof-of-concept demonstration by measuring in purified buffers, e.g. in reference [86] and [207], PBS is used as the buffer for IgG detection. Our EGGFET immunoassay actually provides a strategy to enable their application for real sample measurement.

It's worth noting that the sensitivity of our EGGFET immunoassay is not the highest among all the reported biosensors. In particular, the LOD is lower than the reported FET biosensor based on CNT [86] and TRGO [207]. However, the determination of the LOD and detection range is highly subjective due to the lack of the uniform criterions for the determination of these parameters (as discussed in Appendix 4). For example, the LOD of the TRGO-FET biosensor is determined by the noise level which yields around 2 ng/mL [207], however the determination of the noise level (10.8% resistance increase) is not specified. The LOD of the CNT-FET biosensor is claimed to be 7 fM in [86], however the determination of the LOD is not specified in the reports. Furthermore,

the LOD and the detection range is mainly determined by the affinity between the bioreceptors and the target analytes. The lower K_D the bioreceptor has, the detection range of the biosensor is of lower concentration. For example, the K_D of the Fab fragment for IgG employed in [86] should be around 10^{-14} M to yield a detection range of picomolar (pM) to femtomolar (fM). Our biosensor exhibits a detection of 2-50 nM is mainly determined by the dissociation constant K_D of the IgG aptamer we used, which is around 10 nM. Lower LOD can be obtained by using bioreceptors with lower K_D .

In summary, the EGGFET immunoassay exhibits high reliability for the detection of analytes from physiological samples due to 1) the high uniformity in the sensitivity of the sensing channels in a single chip; 2) the well regulation of the matrix effects and the operation procedure; 3) the statistical validation of the measured results using multiple parallel EGGFET immunosensors. The performance can be further improved by optimizing the operation parameters, such as the composition/pH of the detection buffer. This assay can also be used for detecting other biomolecules by functionalizing graphene channels with their corresponding bioreceptors. It's worth noting that the operation parameters should be adjusted depending on the physical and physiological properties of the target biomolecules, e.g. the pH of the buffer should be adjusted based on the isoelectric point (pI) of the target proteins. Compared with traditional immunoassay techniques, such as the commercial ELISA, the EGGFET immunoassay is label-free and easy to use. It doesn't rely on specific signal collecting equipment and can be easily integrated into electrical measurement and sample delivery systems, suggesting its great prospect for point-of-care applications.

6.5. Conclusion

In this chapter, matrix effects of electrolytes were investigated for electrolyte-gated graphene biosensor, the results show that the composition, pH, and ionic strength of the electrolyte have considerable impact on the characteristics and performance of EGGFET due to the polarization-induced interaction at the interface between electrolyte and graphene. The study on the matrix effect on the EGGFET biosensors provides a more in-depth understanding in the characteristics, optimization, and application of the EGGFET biosensors. An EGGFET immunoassay was further demonstrated to allow well regulation of the matrix effects and being able to detect analyte from physiological samples, which has the potential for practical application. Considering the label-free detection capability and ease of operation, the EGGFET immunoassay has great prospect for point-of-care biomedical applications.

Chapter 7. Capacitance Behavior of the Electrolyte-graphene Interface and the Carrier Statistics in Graphene

Understanding the “device physics” of an electronic device is of critical importance for its design and applications. Different from the traditional metal-oxide-semiconductor field effect transistors (MOSFET), in EGGFET, the gate voltage is applied on the electrolytes and the electrolyte-graphene interface serves as the gate dielectric. In this chapter, the capacitance behavior of the electrolyte-graphene interface and the transport behavior in the graphene channel are studied. The results suggest that the electrolyte-graphene interface exhibits a complex constant phase element (CPE) behavior ($\frac{1}{Z} = Q_0(j\omega)^\alpha$) with both Q_0 and α dependent on the gate voltage. The capacitance of the electrical double layer (EDL) capacitance and the quantum capacitance of graphene are determined; the carrier mobilities in the graphene channel are extracted based on the measurement results. The studies give insight into the device physics of the EGGFET biosensor and are fundamental for the future improvement on the design of the EGGFET biosensors.

7.1. Introduction

7.1.1. Interfacial capacitance at the electrolyte-graphene interface

The development of the EGGFET biosensor requires an in-depth understanding on the device physics of the EGGFET, e.g., its transfer characteristics and carrier statistics, etc. The gate capacitance is of critical importance because it determines the transconductance, which is one of the key parameters characterizing the sensitivity of the EGGFET biosensors [31]. Different from the traditional metal-oxide-semiconductor field effect transistors (MOSFET), in EGGFET, the gate voltage is applied on the electrolyte and the electrolyte-graphene interface serves as the gate dielectric. Therefore, it is of particular interest to study the capacitance behavior of the electrolyte-graphene interface.

The total capacitance of the electrolyte-graphene interface is governed by two factors: the capacitance of the electrical double layer (EDL) (C_{EDL}) and the quantum capacitance (C_{Q}) of the graphene channel [208]. Considering the series arrangement of these two capacitors, the total capacitance (C_{total}) of the electrolyte-graphene interface can be calculated as [208,209]

$$\frac{1}{C_{\text{total}}} = \frac{1}{C_{\text{EDL}}} + \frac{1}{C_{\text{Q}}} \quad (7-1)$$

The EDL arises from the accumulation of counterions at the electrolyte-graphene interface which gives rise to an electrostatic layer that compensates the charges in the graphene channel [210]. The capacitance of the EDL is typically in the scale of several $\mu\text{F}/\text{cm}^2$, which is much higher than the capacitance of a typical silicon dioxide (SiO_2) dielectric layer (several nF/cm^2) [92,210]. As a result, the EGGFET exhibits much higher transconductance when operated in the electrolyte-gated mode than in the back-gated mode [92]. Typically, EDL doesn't behave as an ideal capacitor, but is considered as the so-called constant phase element (CPE) [211], whose impedance (Z) has the form of

$$Z = \frac{1}{Q_0(j\omega)^\alpha} \quad (7-2)$$

where Q_0 has the numerical value of the admittance at $\omega = 1 \text{ rad/s}$. The unit of Q_0 is $\text{S} \cdot \text{s}^\alpha$. Different from the ideal capacitors whose impedance always have a phase angle of -90° , the phase angle of a CPE's impedance is $-90^\circ \cdot \alpha$ ($0 < \alpha < 1$). Till now there is no particular theory that can well explain the CPE behavior of the EDL; several possible explanations include the surface roughness of the electrodes [212], the inhomogeneous distribution of the reaction rates on the surface of the electrodes [213], the varying thickness or composition of the surface coating layer [214] and the non-uniform distribution of current on the electrode surface [215], etc. However, as pointed out by Macdonald in his textbook [216], very often the CPE can well fit the experimental data and

describe the capacitance behavior of the EDL. To better understand the capacitance behavior of the electrolyte-graphene interface, the frequency response of the interfacial capacitance is to be studied.

On the other hand, the interfacial capacitance between electrolyte and graphene is limited by the quantum capacitance (C_Q) of graphene, which arises from the low density of states in graphene [217]. Based on the linear density of states in graphene, the quantum capacitance (C_Q) of graphene is approximately linear with respect to the electrostatic potential in the graphene sheet [217]. Xia [208] first measured the quantum capacitance of the graphene electrode as a function of gate potential and after then several reports have demonstrated the voltage dependence of the quantum capacitance (C_Q) of graphene. At low gate potentials, the total capacitance (C_{total}) of the electrolyte-graphene interface is dominated by the quantum capacitance (C_Q) of graphene, which is smaller than the capacitance of EDL (C_{EDL}) [208,210]. Therefore, to better understand the capacitance behavior of the electrolyte-graphene interface, the contribution of the quantum capacitance has to be taken into account [209].

Several reports have recently studied the interfacial capacitance of graphene in various electrolytes, such as ionic liquid [208], ion-gels [195] and aqueous electrolytes [218–221]. They show the voltage dependence of the interfacial capacitance, with a minimum value (the interfacial capacitance at the Dirac point) ranging from 1 $\mu\text{F}/\text{cm}^2$ [221] to 5 $\mu\text{F}/\text{cm}^2$ [208]. However, these reports failed to display the complexity of the interfacial capacitance of graphene in aqueous electrolytes. In these reports, the interfacial capacitance was measured either at a fixed frequency assuming it behaves as an ideal capacitor [208] or over some range of frequency but ignoring the frequency dispersion [218,219]. Considering the CPE behavior of the EDL, the frequency response of the electrolyte-graphene interface is to be studied to better understand its capacitance behavior.

7.1.2. Carrier statistics in the graphene channel

Carrier mobility and density are important parameters that characterize the transport properties of semiconductors. In fact, the intrinsic high carrier mobility is one of the most exciting features of graphene for its applications in nanoelectronics biosensors [31,104]. The carrier mobility of the one-atom-layer graphene is highly dependent on the environment, e.g. the carrier mobility of graphene is compromised by the scattering from the substrates it resides on [142,160]. In EGGFET, the graphene channel is directly exposed to the highly ionized electrolyte; it is of particular interest to learn if the ions in the electrolyte would introduce extra scattering for the carriers in graphene. This is especially true when considering that the gating effect in EGGFET is achieved by the accumulation of the ions in the EDL, in which the first layer is almost directly anchored on the graphene surface.

The carrier mobility can be determined by the Hall effect or inferred from the transistor behavior. Hall effect allows direct measurement of the carrier density and the carrier mobility can be extracted based on the measured conductance [222]. Garrido [31] and Minot [223] measured the carrier density and mobilities of graphene in aqueous electrolytes using the Hall bar structure. The Hall effect measurement involves specific device configuration and measurement technique. More importantly, near the Dirac point, the estimation of the carrier density because invalid because the Hall voltage goes to zero when the number of holes and electrons is similar [31]. The field-effect measurement provides a feasible alternative to estimate carrier mobility and is compatible with our biosensor design. Many reports have studied the extraction of the carrier mobility in graphene based on the field effect measurement [165,222,224–227]. However, most of these reports are based on the back-gated graphene transistors using silicon oxide as the gate capacitor and thus fail to display the complexity of the electrolyte-gated field effect mobility. Hess [165] derived the carrier mobility in graphene from the measured transfer curve of the EGGFET and a theoretical

prediction of the gate capacitance based on the extended Poisson-Boltzmann (ePB) model. To the best of our knowledge, till now there is no report that extracts the carrier mobility based on the experimentally measured interfacial capacitance, which should provide a more accurate result. In this study, we present the extraction of the carrier mobility based on the transfer curve measurement and capacitance-voltage profiling.

In this chapter, we present a study on the capacitance behaviors of the electrolyte-graphene interface by studying its frequency response using electrochemical impedance spectroscopy (EIS). The gate voltage dependence of the interfacial capacitance is studied using capacitance-voltage (C-V) profiling; the capacitance of the EDL and the quantum capacitance of the graphene are differentiated which allows us to estimate the carrier density in the graphene. In the end, the carrier mobility in the graphene channel is extracted. 0.1 M NaF solution was used as the electrolyte for all the experiments in this chapter.

7.2. Experiments

7.2.1. EIS measurement

EIS is a frequency domain measurement technique often used to study the interfacial behavior in electrochemical systems, such as the charge transfer resistance, interfacial capacitance, etc. [228]. Briefly, if we apply a small AC voltage perturbation to an electrochemical cell and measure the output AC current (magnitude and phase shift), the impedance of the system can be obtained as a function of the applied frequency. EIS data are commonly analyzed by fitting to an equivalent electrical circuit model, in which each electrical element should have a basis in the physical electrochemistry of the system. For example, a CPE is typically involved in an electrical circuit model to describe the capacitance behavior of the EDL. In this section, we use EIS to measure the

frequency response of the electrolyte-graphene interface, which is used for the analysis of its capacitance behavior.

Circular graphene electrodes as shown in **Figure 7.1a** were used for EIS measurement. It has a graphene electrode of 500 μm in diameter that is electrically connected using a metal contact. **Figure 7.1b** shows the zoom-in view of the graphene electrode and a schematic of the cross-section is shown in **Figure 7.1c**. A photoresist layer was employed to (1) precisely define the circular area of graphene (500 μm in diameter) that was exposed to the electrolyte and (2) passivate the metal contacts. A PDMS well (not shown) with an opening of 5 mm in diameter was applied on the chip for the confinement of the electrolytes. More details about the fabrication of the graphene electrodes are given in Section 3.2.

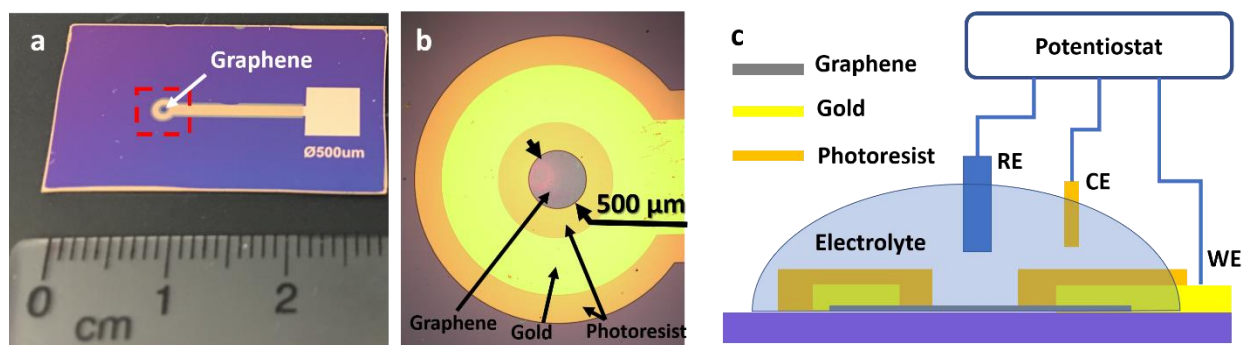


Figure 7.1 The device and the schematic diagram of the experimental setup for EIS measurement. a) A picture of the graphene electrode for EIS measurement; b) The zoom-in view of the graphene electrode as marked by the red dashed box in a); c) The cross-section schematic (not scaled) of the graphene electrode and the EIS measurement setup.

A schematic diagram of the experimental setup is shown in **Figure 7.1c**. The EIS measurements were conducted with a Gamry Interface 1000T potentiostat in a three-electrode configuration with a standard Ag/AgCl electrode as the reference electrode (RE) and a gold wire as the counter electrode (CE). The graphene electrode was connected to the working electrode (WE) of the

potentiostat. The EIS spectrum were collected over a frequency range from 20k Hz to 0.1 Hz with an AC perturbation voltage of 10 mV rms. The potential of the graphene electrode was swept from -0.5 V to +0.5 V vs REF with a step of 0.05 V.

7.2.2. Transfer curve measurement and C-V profiling

The transfer curves measure the drain current (I_d) of the graphene channel as a function of the gate voltage (V_g). The C-V profiling is a technique for measuring the gate capacitance as a function of the gate voltage (V_g). The device for the transfer curve measurement and the C-V profiling is shown in **Figure 7.2a**. Each device contains six parallel graphene channels that are electrically connected using metal contacts as the source and drain electrodes. **Figure 7.2b** shows the zoom-in view of the graphene channels which have a dimension of 75 μm in width and 150 μm in length. A photoresist layer was employed to passivate the metal contacts so that only the graphene channels were exposed to the electrolytes. A PDMS well (not shown) with an opening of 5 mm in diameter was applied on the chip for the confinement of the electrolytes. More details about the fabrication of the devices are given in Section 3.2.

The transfer curve measurements were conducted with two source measure units (SMU) in a Keithley 4200 Semiconductor Characterization System (SCS) with a standard Ag/AgCl reference electrode serving as the gate. The experimental setup is shown schematically in **Figure 7.2c**. The gate voltage (V_g) was applied using SMU2 which swept from -0.5 V to +0.5 V with steps of 1 mV and a scan rate of 10 mV/s. The drain current (I_d) is measured by SMU1 with a 10 mV load (V_{ds}). The C-V profiling was conducted with a capacitance-voltage unit (CVU) in the Keithley 4200 SCS with an AC perturbation voltage of 10 mV rms. The CVU allows two operation modes: frequency sweep and voltage sweep. Firstly, we applied constant gate voltages (V_g) and measured the impedance as a function of the frequency. Secondly, we measured the impedance as a function of the gate voltage (V_g) at fixed frequencies.

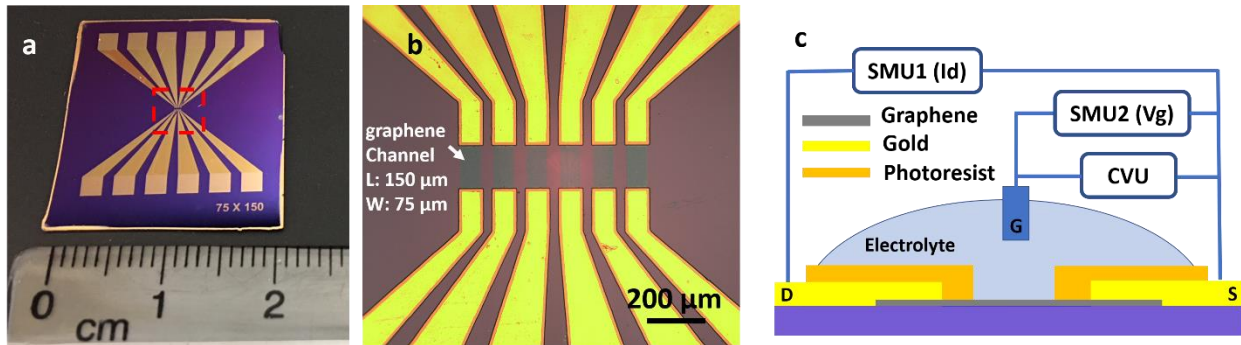


Figure 7.2 The device and the schematic diagram of the experimental setup for transfer curve measurement and C-V profiling. a) A picture of the graphene electrode for EIS measurement; b) The zoom-in view of the graphene electrode as marked by the red dashed box in a); c) The cross-section schematic (not scaled) of the graphene electrode and the EIS measurement setup.

7.3. Capacitance behavior of the electrolyte-graphene interface

Figure 7.3 shows the representative Bode plot of the graphene electrode. A capacitive regime with a phase shift of $\sim -80^\circ$ is observed at 100-1000 Hz. At frequencies lower than 100 Hz, the electrode exhibits a mixed response (capacitive and resistive) due to the current leakage. An equivalent Randles circuit model (see inset in **Figure 7.3b**) can be used to fit the measured impedance. The correspondence between the circuit elements and the electrochemical systems are listed as below:

- Rs** - The series resistance, including the access resistance, electrolyte resistance, etc.;
- CPE** - The interfacial capacitance at the electrolyte-graphene interface;
- Zf** - The faradaic impedance, which causes the leakage current;
- Zw** - The Warburg impedance, which is attributed to the diffusion-limited faradaic reaction.

The fitting yields a CPE with $Q_0 = 3.8 \times 10^{-9} \text{ S} \cdot \text{s}^\alpha$ and $\alpha = 0.89$ which corresponds to the capacitive regime with a phase shift of around -80° in the frequency range of 100 – 1000Hz (**Figure 7.3b**), which suggests that the electrolyte-graphene interface behaves as a CPE rather than an ideal

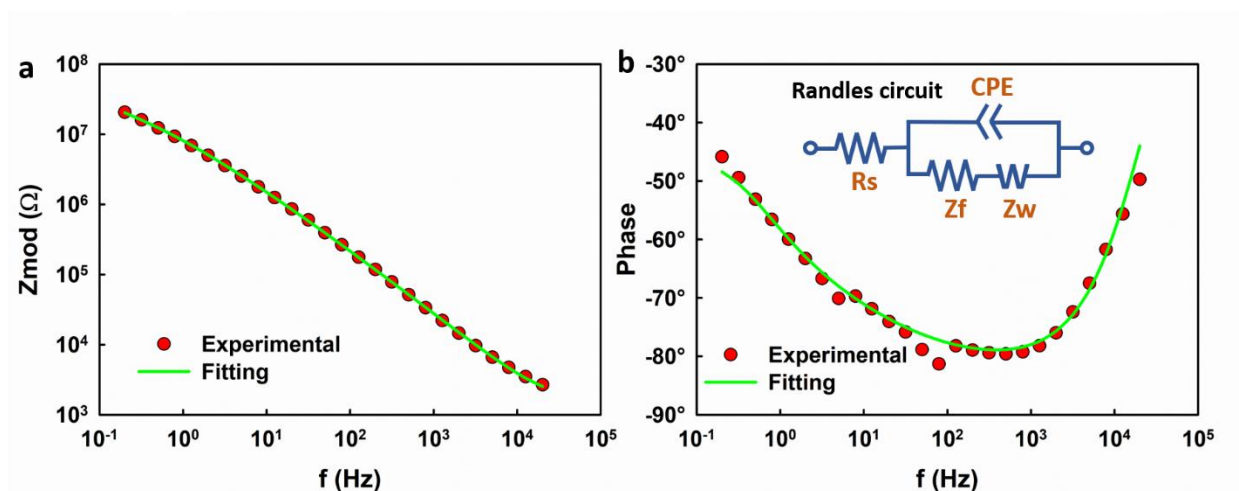


Figure 7.3 Representative Bode plot of the graphene electrode and the fitting curve using the Randles circuit shown in the inset of (b).

capacitor. A similar result was reported by [209] in which a capacitive regime with a phase shift of around -85° was observed. Using the Randles circuit model, we analyzed the impedance of the graphene electrode at different gate voltages. The fitting results of Q_0 and α are plotted with respect to the gate voltage (V_g) in **Figure 7.4**. Q_0 exhibits an ambipolar behavior with a minimum of $3.0 \times 10^{-9} \text{ S} \cdot \text{s}^\alpha$ at $V_g \approx +0.2 \text{ V}$ and increases on both sides of the minimum value. Noting that the Q_0 is numerically equal to the capacitance at $f=1 \text{ Hz}$, the result is expected considering the V_g dependence of the quantum capacitance in the graphene as discussed above. What surprises us is that α also exhibits an ambipolar behavior with respect to the gate potential, which is unique for typical EDL.

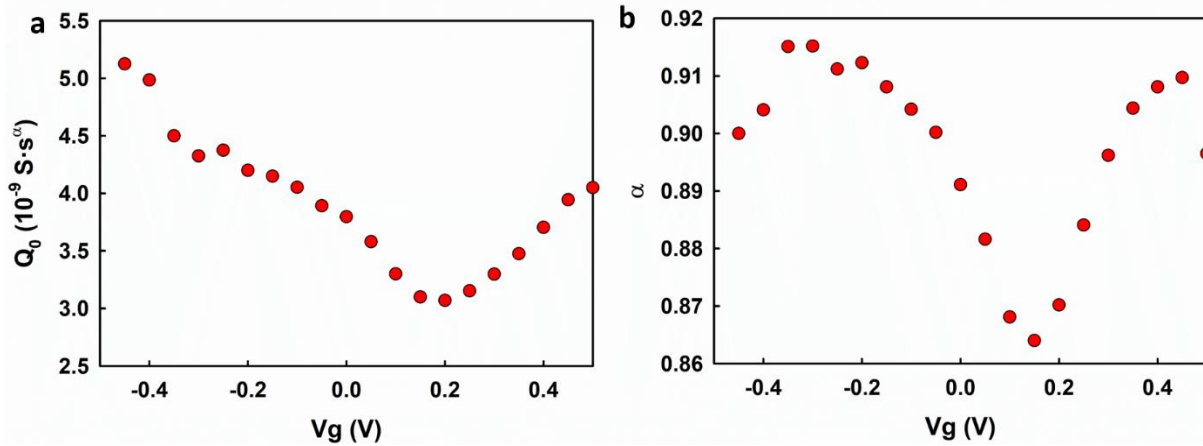


Figure 7.4 Fitting results using the Randles circuit model.

Even though the Randles circuit model can well reproduce impedance spectrum (as shown in **Figure 7.3**), it might also introduce high uncertainties to the fitting result because it involves too many fitting parameters, which could possibly lead to the observed V_g -dependence of α . To rule out this possibility, we analyzed the measured impedance spectrum using a simplified electrical circuit model which consists of a resistor and a CPE in series arrangement as shown in the inset of **Figure 7.5**. For convenience, the simplified model is called the Rs-CPE model. The Rs-CPE model

is based on the analysis of the out of phase elements (Z'') of the impedance spectrum in the capacitive region. In the absence of charge transfer induced by Faradaic reactions at the electrolyte-graphene interface, Z_f and Z_w can be removed leading to the simplified R_s -CPE circuit whose impedance can be calculated as

$$Z = R_s + \frac{1}{Q_0(j\omega)^\alpha} \quad (7-3)$$

The out-of-phase (Z'') component is

$$Z'' = \frac{-\sin\left(\frac{\pi\alpha}{2}\right)}{Q_0\omega^\alpha} \quad (7-4)$$

We get

$$\log(-Z'') = \log\left(\frac{\sin\left(\frac{\pi\alpha}{2}\right)}{(2\pi)^\alpha Q_0}\right) - \alpha \log f \quad (7-5)$$

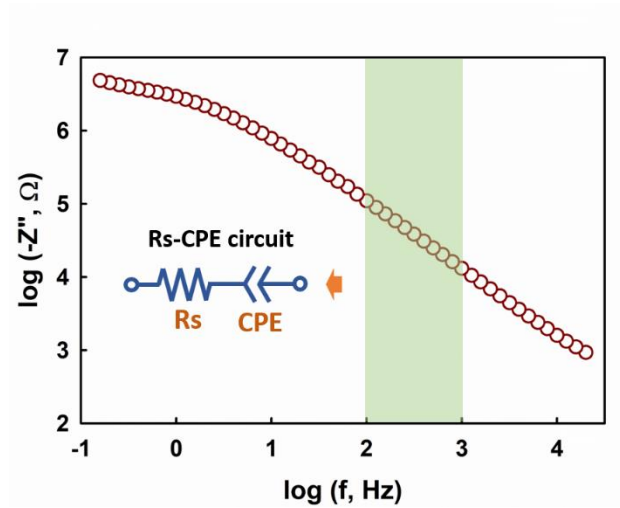


Figure 7.5 A representative plot showing $\log(-Z'')$ with respect to $\log(f)$. The inset shows the R_s -CPE circuit model.

According to equation 7-5, if we plot $\log(-Z'')$ with respect to $\log f$, a linear relationship would be expected, and the slope would be $-\alpha$. The Q_0 can thereby be calculated based on the intercept $\log\left(\frac{\sin(\frac{\pi\alpha}{2})}{(2\pi)^\alpha Q_0}\right)$ at $f=1$ Hz. As shown in **Figure 7.5**, $\log(-Z'')$ exhibits good linearity with respect to $\log f$ at frequencies. We applied linear regression analysis in the frequency range of 100-1000 Hz; the fitting results of Q_0 and α are shown in **Figure 7.6** with respect to the gate potential (V_g). Both Q_0 and α exhibit dependence on the gate potential (V_g), which is in accordance with the fitting results using the Randles circuit model. Based on the fitting results using the two different models, we claim the observed V_g dependence of α is not caused by the experimental error, but rather an intrinsic property of the electrolyte-graphene interface.

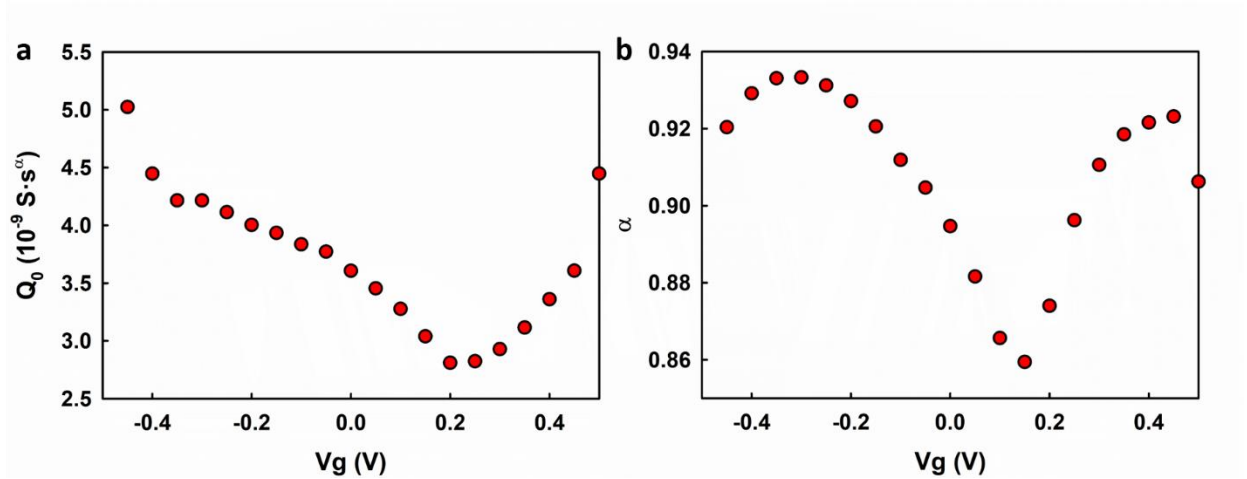


Figure 7.6 Fitting results using the Rs-CPE circuit model as a function of the gate voltage

To the best of our knowledge, the dependence of α on V_g has not been reported till now. We speculate this unique phenomenon could be attributed to the low density of states in graphene near the Dirac point which makes α sensitive to the imperfections in the graphene. As is reported previously [208,229], the properties of graphene is highly subject to the imperfections in it, such as the charged impurities, lattice defects and dopants, etc. These imperfections could be considered as local sites with density of states that are different from these in the “good” graphene sites. Considering the single-atom-layer structure and low density of states of graphene at low energy level, such imperfections might have a significant impact on the capacitance behavior of the graphene electrodes. A schematic diagram depicting this effect is shown in **Figure 7.7**. When the gate potential is low (**Figure 7.7a**), e.g. near the Dirac point, the carrier density in the graphene is low and the capacitance is limited; these imperfections dominate the capacitance behavior of the graphene electrode, which gives rise to the smaller α values. When the gate potential in graphene is driven away from the Dirac point (**Figure 7.7b**), the carrier density in graphene is high and the

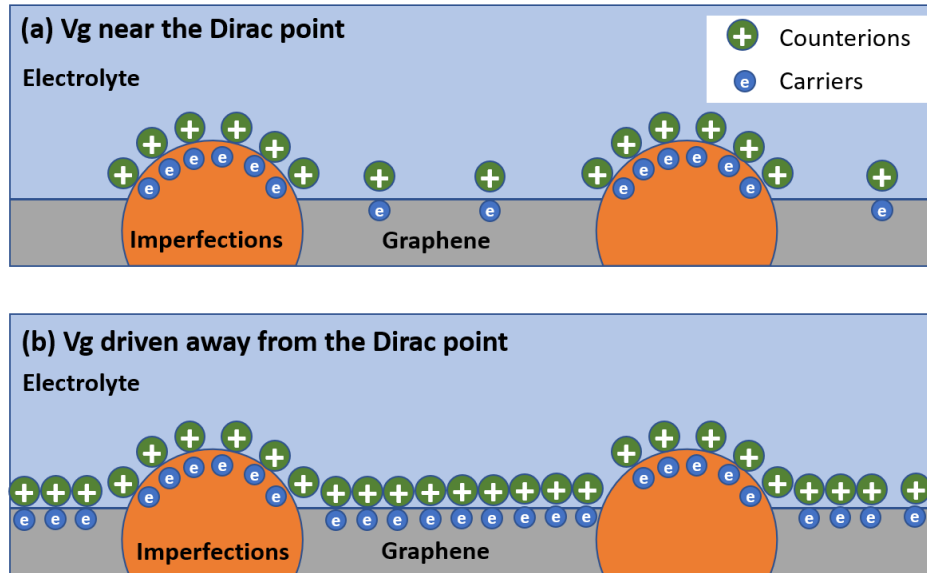


Figure 7.7 Schematic diagram showing the impact of the imperfection sites on the capacitance behavior of the electrolyte-graphene interface.

imperfections are “submerged” by the carriers in the graphene lattice; as a result, these imperfection states exhibits smaller impact on the interfacial capacitance behavior and a higher α is observed.

7.4. Determination of C_{EDL} and C_Q

For an ideal capacitor, the capacitance can be calculated based on the imaginary part (Z'') of the measured impedance at any frequency using equation

$$C = \frac{1}{2\pi f(-Z'')} \quad (7-6)$$

However, as discussed above, the electrolyte-graphene interface behaves as a CPE rather than an ideal capacitor, which gives rises to a frequency dispersion of the calculated capacitance. In this

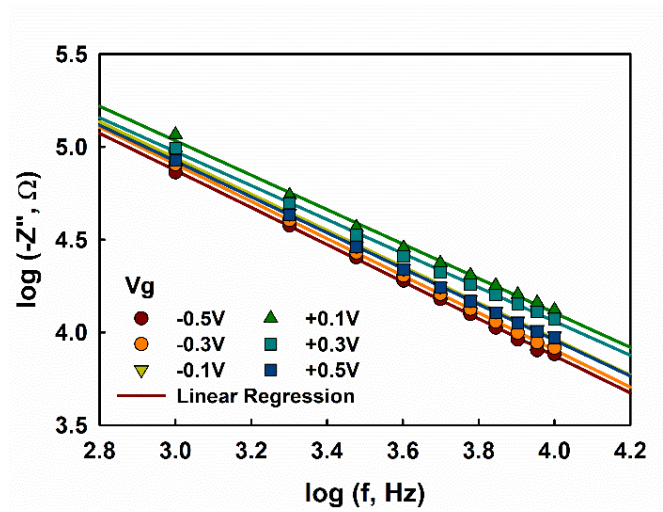


Figure 7.8 A representative plot showing $\log(-Z'')$ with respect to $\log(f)$ at different gate voltages.

dissertation, Q_0 , which is numerically equal to the capacitance at $f = 1$ Hz, is chosen as the interfacial capacitance of the electrolyte-graphene interface. We first measured the frequency response of the graphene channels at fixed voltages (V_g). As shown in **Figure 7.8**, good linearity

with slopes approximating but less than one ($\alpha \lesssim 1$) is observed at all V_g , which suggests that the interface between the electrolyte and the graphene channel works in a capacitive regime in this frequency range (1k-10k Hz) according to equation 7-5.

For C-V profiling, we prefer to measure the capacitance in a continuous voltage range. Therefore, we measured the impedance of the graphene at selected frequencies (1k, 2k, 3k, 4k, 6k, 8k, 10k Hz) while sweeping the V_g from -0.5V to 0.5V with steps of 1 mV. The results are shown in **Figure 7.9**. According to equation 5-5, we applied linear regression analysis of $\log(-Z'')$ with respect to $\log f$; Q_0 and α were extracted based on the intercept at $f = 1$ Hz and the slope using equation 7-5, respectively. As shown in **Figure 7.10**, both Q_0 and α show dependence on V_g , which is in accordance with the unique CPE behavior of the electrolyte-graphene interface as discussed above.

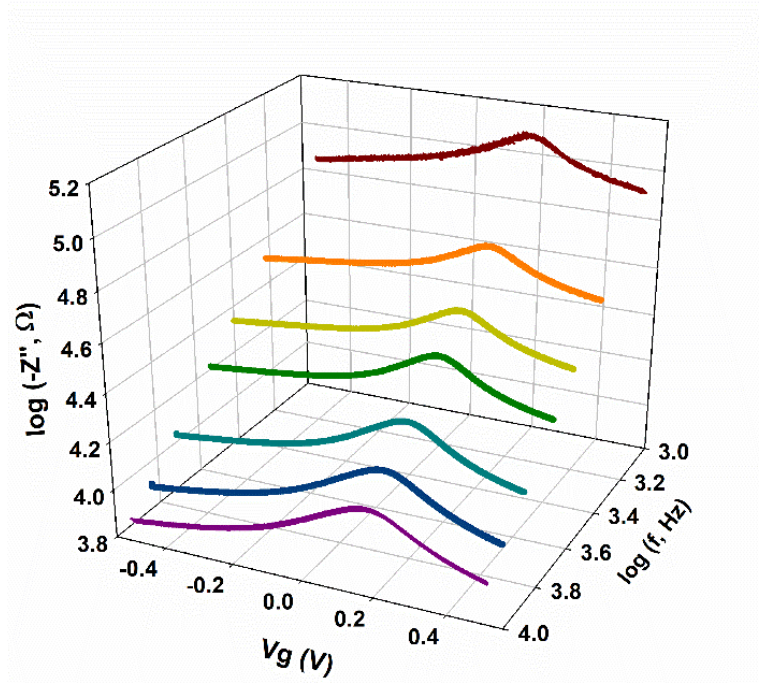


Figure 7.9 The C-V profiling of the EGGFET at different frequencies.

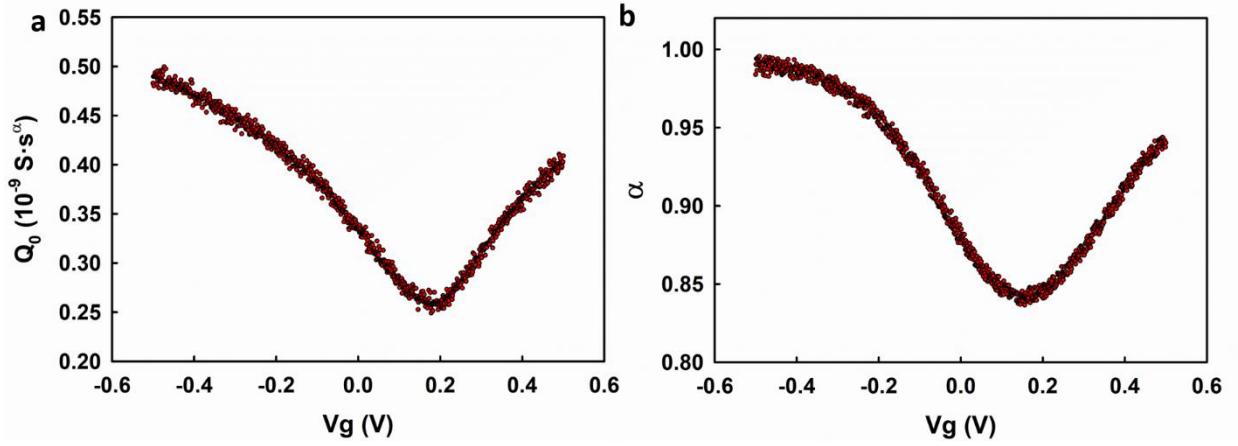


Figure 7.10 Fitting results based on the C-V profiling.

Fang [217] derived the quantum capacitance (C_Q) of graphene as a function of the local electrostatic potential (V_{ch}) (see Appendix 5):

$$C_Q = \frac{2e^3}{\pi(\hbar v_F)^2} V_{ch} \quad (7-7)$$

in which e is the elementary charge; \hbar is the reduced Planck's constant; $v_F \sim 10^8 \text{ cm/s}$ is the Fermi velocity of carriers in graphene. According to equation 7-7, the C_Q should be zero at the Dirac point for ideal graphene, which would lead to an overall interfacial capacitance of zero at the Dirac point. The non-zero minimum interfacial capacitance observed in **Figure 7.10a** could be attributed to the imperfections in the real graphene, which could introduce local density-of-states and residue carriers and cause the deviation of the capacitance near the Dirac point. It has been reported that the charged impurities could cause local potential fluctuations and carrier puddles in graphene [229,230]. Xia [208] included these residual carriers and built a quantitative model for the quantum capacitance of non-perfect graphene.

Considering (see Appendix 5)

$$n \cong \left(\frac{eV_{ch}}{\hbar v_F \sqrt{\pi}} \right)^2 \quad (7-8)$$

Equation 7-7 reduces to

$$C_Q = \frac{2e^2}{\sqrt{\pi}\hbar v_F} \sqrt{n} \quad (7-9)$$

Xia took an approximation that the total carrier density in graphene is

$$n_{total} = n_g + n_{res} \quad (7-10)$$

in which n_g is the gate voltage induced carrier density; n_{res} is the residue carrier density introduced by the imperfections. The quantum capacitance C_Q can thereby be given as

$$C_Q = \frac{2e^2}{\hbar v_F \sqrt{\pi}} (n_g + n_{res})^{1/2} \quad (7-11)$$

Considering the series arrange of the EDL capacitance and the quantum capacitance, the total interfacial capacitance (C_{total}) can be calculated based on equation 7-1. Till now we have built a model for the electrolyte-graphene interface that integrates the EDL capacitance and the quantum capacitance of graphene. For simplicity, we name it Model 1 (inset of **Figure 7.11**). We replotted the measured interfacial capacitance (C_{total}) with respect to the Dirac point in **Figure 7.11** and the results were fitted using the Model 1. The detailed fitting method is given in Appendix 5. The

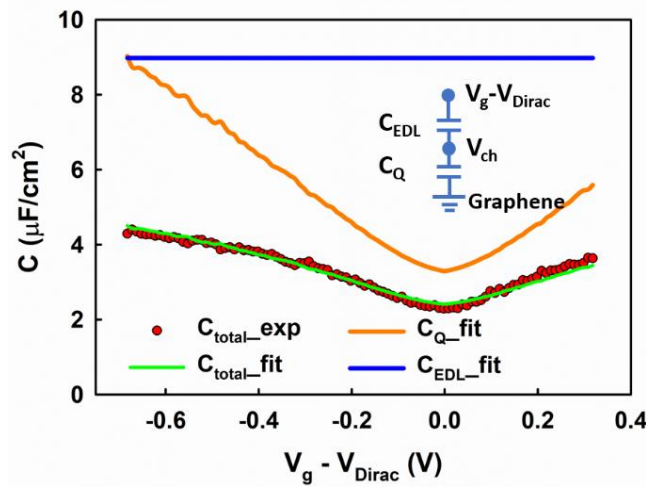


Figure 7.11 Fitting results based on the model as shown in the inset.

capacitance of the EDL (C_{EDL}) and the residual carrier density (n_{res}) are assumed to be constant over the measured voltage range. The quantum capacitance of the graphene is calculated based on the fitting results and plotted in **Figure 7.11** (orange line). Based on the fitting results, the interfacial capacitance at the electrolyte-graphene interface is limited by the quantum capacitance (C_g) in the low voltage range measured, which is in accordance with previous reports [208,221]. As shown in **Figure 7.11**, the experimental result can be roughly fitted with this model. However, there is some systematic deviation between the fitted result and the experimental result. For example, at the low voltage range, the fitting results in a slight overestimation of the interfacial capacitance. It's worth noting that the similar deviation is also observed in Xia's report [208]. A better fitting can be obtained by adding a compensating capacitance (C_{comp}) in parallel with the interfacial capacitance of graphene (Model 2, see inset of **Figure 7.12**). As shown in **Figure 7.12**, the new model can better reproduce the experimental results in the whole voltage range. The compensating capacitance might be attributed to the following causes: (1) The “leakage

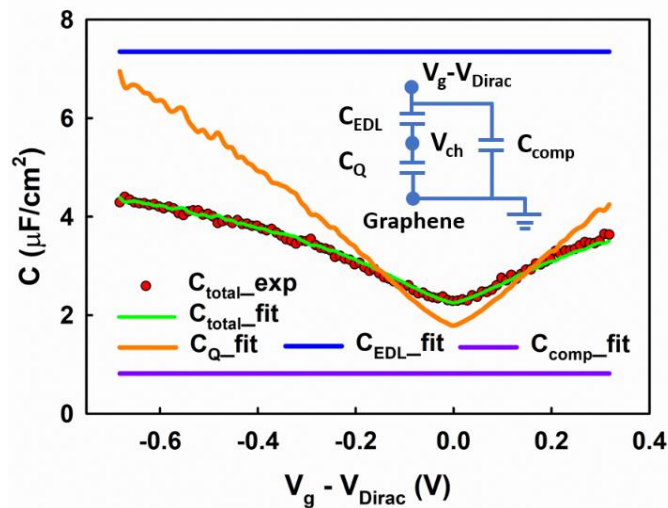


Figure 7.12 Fitting results based on the model 2 which includes a compensating capacitance.

capacitance” of the metal contacts (source and drain electrodes). Even though the metal contacts have been passivated by a photoresist layer, its area exposed to the electrolyte (around 0.025 cm^2 estimated based on **Figure 7.2**) is still much larger than that of the graphene (around $1.125 \times 10^{-4} \text{ cm}^2$, **Figure 7.2b**). Therefore, it might generate considerable parasite capacitance. (2) The imperfect sites in graphene. As mentioned previously, there are inevitable imperfections in graphene, e.g. impurities, defects and dopants. These imperfections might present different density of states comparing with the perfect graphene, and therefore behave as an extra capacitor which is in parallel with the remaining graphene sites. In addition, the compensating capacitance might be responsible for the observed gate voltage dependence of α as discussed in Section 7.3. Nevertheless, the origin of this compensating capacitance is still to be studied.

A comparison between the fitting results using the two models is given in **Table 7.1**. The compensating capacitance is fitted to be $0.82 \text{ } \mu\text{F}/\text{cm}^2$ (normalized with respect to the area of the graphene channel), which is fairly high comparing the total capacitance and would have significant impact on the fitting results. Ignoring the compensating capacitance causes the overestimation of the residue carrier density n_{res} , which is an importance parameter for the extraction of the carrier mobility. The compensating capacitance also causes a slight difference among the fitted C_{EDL} .

Table 7-1 Comparison of the fitting result based on the two models

Parameters	Units	Model 1	Model 2
C_{EDL}	$\mu\text{F}/\text{cm}^2$	8.98	7.35
n_{res}	cm^{-2}	1.36×10^{12}	3.39×10^{11}
C_{comp}	$\mu\text{F}/\text{cm}^2$	0	0.82

Based on the previous analysis, the following conclusions are obtained. (1) The total interfacial capacitance at the electrolyte-graphene interface is limited by the quantum capacitance of graphene

at low potential and exhibit a voltage-dependence. (2) the EDL capacitance is around $7.35 \mu\text{F}/\text{cm}^2$, which is close to the experimental result from [221]. The value is lower than the interfacial capacitance for metal electrodes (typically around $20 \mu\text{F}/\text{cm}^2$) [219,231], which could be possibly attributed to the dielectric saturation of water near the surface of the highly charged graphene [210]. (3) the fitting yields a residue carrier density $n_{\text{res}} = 1.36 \times 10^{12} \text{ cm}^{-2}$, which is comparable to previous reports [229,232].

Overall, the theoretical model could well explain our measured interfacial capacitance of the graphene electrode; the EDL capacitance (C_{EDL}) and the quantum capacitance (C_Q) are determined using the model. Comparing with previous reports, in which the C_{EDL} was set to be a specific value, e.g. $20 \mu\text{F}/\text{cm}^2$ [208,219], our multi-factor curve fitting method takes C_{EDL} as a variable fitting parameters which should provide more accurate results.

7.5. Carrier mobility in graphene

The conductivity of the graphene channel is mainly determined by the drift of the carriers which is given as

$$\sigma = en\mu_e + ep\mu_h \quad (7-12)$$

in which σ is the sheet conductivity of graphene; n and p are the density of electrons and holes, respectively; μ_e and μ_h are the mobility of electrons and holes, respectively. The carrier mobilities can be extracted based on the sheet conductivity σ and the carrier densities (n and p), which can be determined by the transfer curve measurement and the C-V profiling, respectively.

The sheet conductivity σ of the graphene channel is calculated as

$$\sigma = \frac{I_d}{V_{ds}} \cdot \frac{L}{W} \quad (7-13)$$

where I_d is the drain current; V_{ds} is the voltage applied between the source and drain; W and L are the width and length of the graphene channel, respectively. The measured sheet conductivity σ can be compromised by the access resistance (R_{access}), including the contact resistance ($R_{contact}$) between the metal and the graphene and the resistance of the source and drain electrode.

To evaluate the impact of the access resistance, we applied a transmission line measurement (TLM). The device used for TLM is shown in **Figure 7.13a**. It consists of five graphene channels with different aspect ratios ($\frac{L}{W}$). The total resistance R_{total} is given as

$$R_{total} = \rho_{graphene} \left(\frac{L}{W} \right) + R_{access} \quad (7-14)$$

in which $\rho_{graphene}$ is the sheet resistivity of the graphene. We measured the transfer curves of each graphene channel and the results are shown in **Figure 7.13b**. According to equation, at a given voltage, R_{total} should be linear with respect to the aspect ratio $\frac{L}{W}$; the slope can be referred as the sheet resistivity of the graphene $\rho_{graphene}$ and the intercept at $\frac{L}{W} = 0$ is the access resistance R_{access} . As shown in **Figure 7.13c**, good linearity is observed. We applied linear regression analysis to the R_{total} with respect to $\frac{L}{W}$ and the $\rho_{graphene}$ and R_{access} are plotted in **Figure 7.13d**. The $\rho_{graphene}$ ranges from 0.7 k Ω/\square to 3.5 k Ω/\square as a function of the gate voltage V_g , which is around 5-7 times of the R_{access} . It's worth noting that the access resistance also exhibits dependence on the gate voltage. It can be attributed to the contact resistance between the metal and the graphene; in the vicinity of the Dirac point, the carrier density in the graphene is low which leads to a high resistance at the metal-graphene junction.

The aspect ratio of the graphene channel was set to be 2 in our devices because 1) it provides a graphene channel resistance that is around 10 orders higher than the access resistance and the contribution of the access resistance can be ignored; 2) it provides a practical resistance range for electrical measurement (the current is in the range of several μA for a voltage load of 10 mV). We

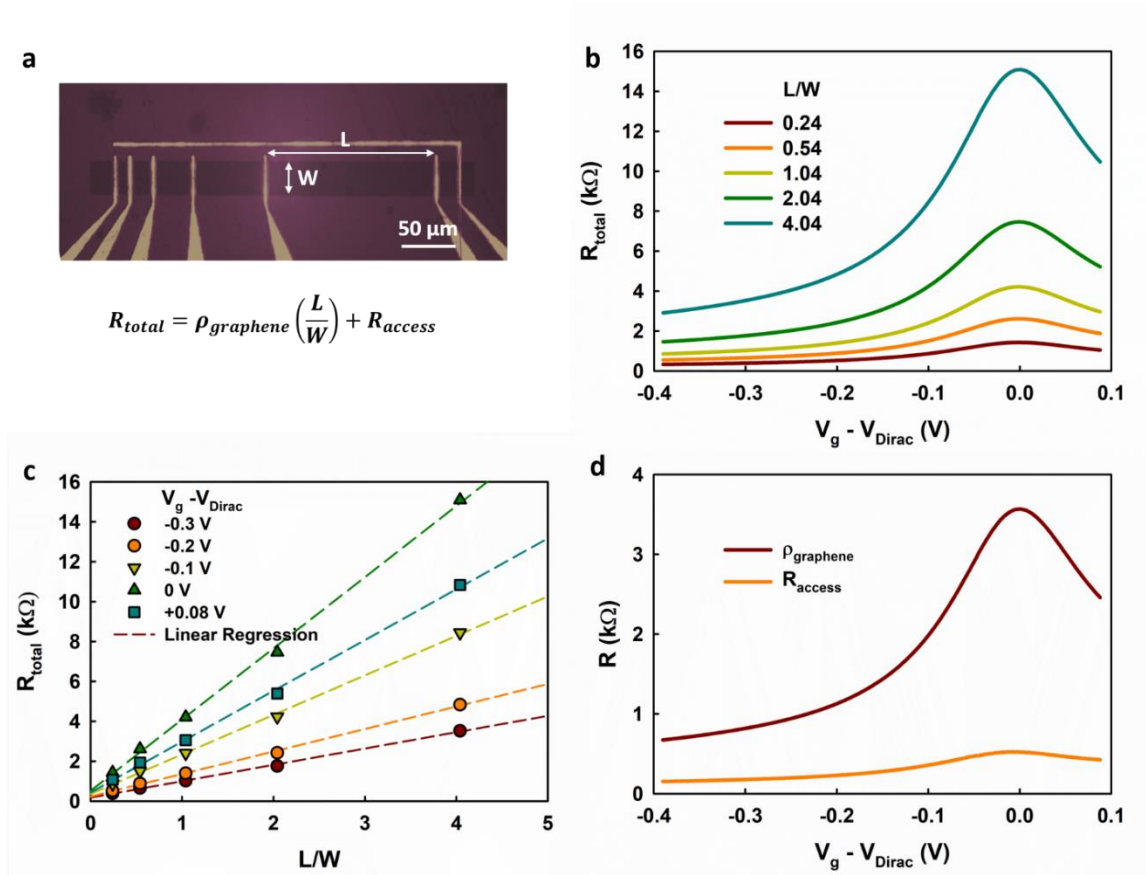


Figure 7.13 Transmission line measurement of the sheet conductivity of graphene and the access resistance. (a) The device for TLM study. (b) The transfer curves of each channel with different aspect ratio. (c). The linear regression analysis of the resistance measurement with respect to the aspect ratio. (d) The extracted sheet resistivity of graphene and the access resistance.

measured the transfer curves of the EGGFET device and the sheet conductivity (σ) is calculated using equation 7-14. The results are shown in **Figure 7.14**.

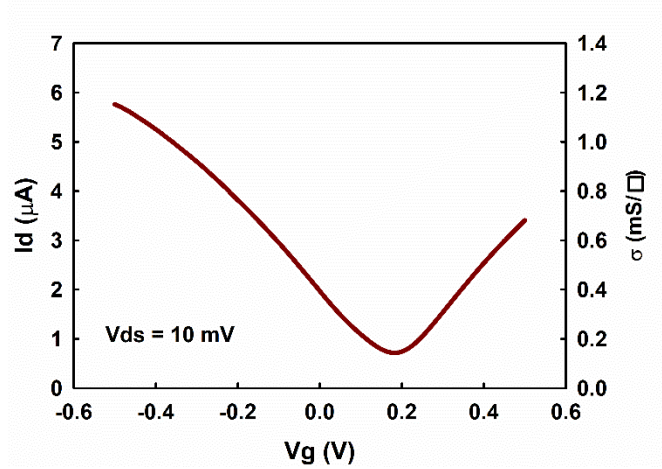


Figure 7.14 The transfer curve of the EGGFET and the extracted sheet conductivity of the graphene channel

The carrier densities (n and p) were extracted based on the C-V profiling analysis as discussed in the previous section using equation 7-10. Based on the mass-action law [224], we add a correction to the overall carrier density

$$np = n_i^2 \quad (7-15)$$

in which n_i is the residue carrier density n_{res} . As a result, the carrier density can be calculated as

$$n_{total} = \frac{n_{res}^2}{(n_{res} + n_g)} + n_{res} + n_g \quad (7-16)$$

and shown in **Figure 7.15**.

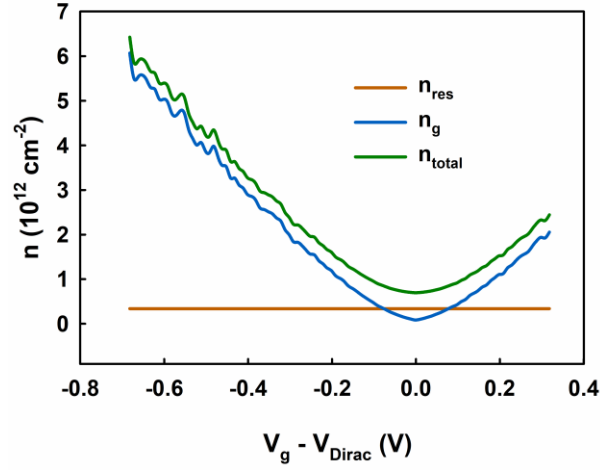


Figure 7.15 The extracted carrier density based on the fitting results obtained in Figure 7.12.

The carrier mobilities were calculated based on equation 7-12 and plotted with respect to the carrier density as shown in **Figure 7.16**. Overall, the carrier mobility is much lower than the theoretical predictions of the ideal graphene ($\sim 2 \times 10^5 \text{ cm}^2 \text{V}^{-1} \text{s}^{-1}$) [40]. The calculated carrier mobility shows a similar dependence on the carrier density as the results given in reference [224] (**Figure 7.17a**). The mobility peaks at $\sim 1700 \text{ cm}^2 \text{V}^{-1} \text{s}^{-1}$ and $2000 \text{ cm}^2 \text{V}^{-1} \text{s}^{-1}$, for holes and electrons, respectively,

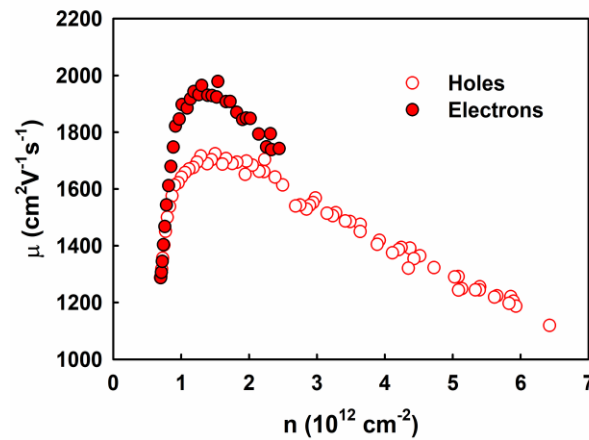


Figure 7.16 The extracted carrier mobility with respect to the carrier density.

and decreases at carrier density higher than $\sim 1.5 \times 10^{12} \text{ cm}^{-2}$. The transition suggests that the dominating scattering mechanism changes from coulomb to phonon scatterings at higher densities [224]. However, the calculated carrier mobility is lower than the results reported in [224], which could be attributed to the quality of the graphene or the scattering from the dissolved ions in the electrolytes. Our results are different from the results measured by the Hall effect [31,223] (**Figure 7.17b**). This is because the Hall effect cannot measure the residue carrier density and thus will cause the overestimation of the carrier mobility near the Dirac point. In our case, the residue carrier density can be obtained based on the analysis of the interfacial capacitance and thus should provide more accurate estimation of the carrier mobility.

The measurement of the conductivity σ and carrier mobility μ allow us to analyze the dominating scattering mechanisms in the graphene. According to the self-consistent theory [229], the charged impurity scattering is responsible for most of the observed transport behavior in graphene. These charged impurities could reside on the substrate or be trapped at the graphene-substrate interface

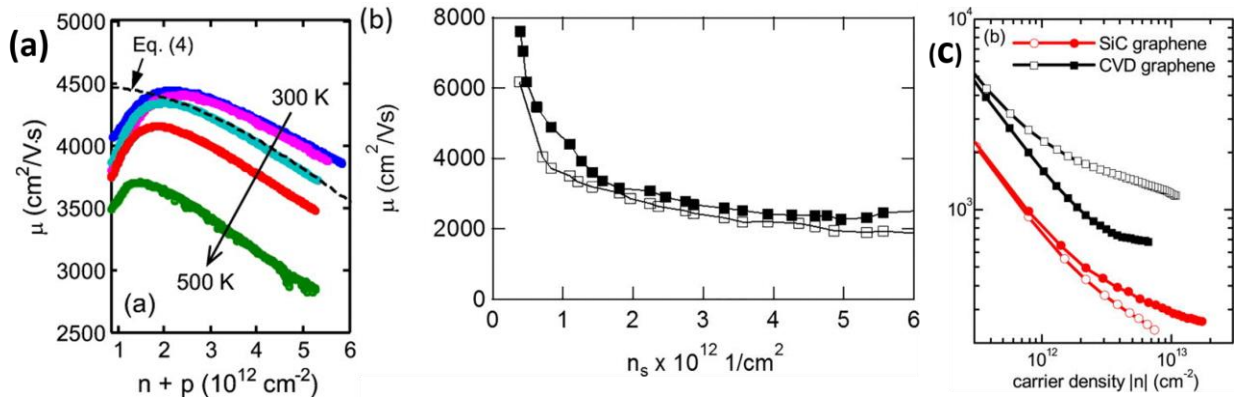


Figure 7.17 Carrier mobility in graphene reported in previous reports. (a) The carrier mobility extracted based on the back-gated graphene FET structure [224]. (b) The measurement results based on Hall effect [223]. (c) The measurement results based on EGGFET structure and theoretically predicted carrier density [165].

during the transfer of the graphene. The typical concentration of charged impurities on SiO₂ substrate is around 10^{12} cm^{-2} and is known to dominate the transport properties of other extensively studied 2D systems [233,234]. In EGGFET, the graphene is directly exposed to the electrolytes and counterions accumulate at the electrolyte-graphene interface. There's a possibility that the ions will introduce extra Coulomb scattering for the carriers in graphene [223]. We compared our measurement results to previous works on dry, SiO₂-supported graphene [40,235]. Since we find similar μ in our electrolyte-gated, SiO₂-supported graphene, we speculate that the charged impurity on the SiO₂ substrate are likely the dominating scattering source in both a dry environment and an aqueous electrolyte environment. This is consistent with the finding in ref [223] and [236] which claim that the SiO₂ substrate has a much greater effect on μ than the dissolved ions in the aqueous electrolyte.

Based on the discussion above, an obvious strategy to improve the carrier mobility is to eliminate the charged impurities on the substrates. According to the self-consistent theory, reducing the impurity concentration to 10^{10} cm^{-2} could increase the carrier mobility to extremely high value of $\sim 2 \times 10^5 \text{ cm}^2/\text{V}\cdot\text{s}$ [234]. A study [237] suggests that using hexagonal boron nitride (h-BN) as the substrate, the carrier mobility in graphene can be improved to be $1.7 \times 10^5 \text{ cm}^2/\text{V}\cdot\text{s}$. For the development of the EGGFET biosensor, the higher carrier mobility would give rise to higher sensitivity. Therefore, choosing the proper substrates with lower charged impurities will significantly improve the performance of the EGGFET biosensors.

7.6. Conclusion

In this chapter, we studied the capacitance behavior of the electrolyte-graphene interface by measuring the frequency response using EIS. The results suggest that the electrolyte-graphene interface exhibits a complex constant phase element (CPE) behavior ($\frac{1}{Z} = Q_0(j\omega)^\alpha$) with both Q_0

and α dependent on the gate voltage. The capacitance of the electrical double layer (CPE) capacitance and the quantum capacitance of graphene are determined; the carrier mobilities in the graphene channel are extracted based on the measurement results. The results suggest that the performance of the EGGFET biosensors is highly compromised by the imperfections in the graphene lattice and scattering introduced by the substrates, which is instructive for the future design of the EGGFET biosensors with improved performance.

Chapter 8. Conclusion and Outlook

In this dissertation, we present studies on the electrolyte-gated graphene field effect transistor (EGGFET) biosensor and its application for the label-free detection of biomarkers.

First, we studied the thermal degradation of the PMMA residue on the transfer CVD graphene and presented an electrolytic cleaning method which is demonstrated to be effective to remove the post-annealing residues. The study revealed the generation of the post-annealing residues due to the elimination of the methoxycarbonyl side chains in PMMA during thermal annealing. These post-annealing residues are believed to be absorbed on graphene via the π - π interaction between the conjugated unsaturated carbon segments and graphene and are difficult to remove by further annealing in non-oxidative atmosphere due to their thermal and chemical stability. The electrolytic cleaning method is shown to be effective to remove these post-annealing residue, resulting in cleaning, residue-free surface, which is critical to obtain reliable devices. The study should be instructive for the improvement on transfer of the CVD graphene, which is important for its application in not only biosensors, but also in a wider range.

The performance of the EGGFET biosensor is demonstrated by the successful detection of human immunoglobulin G (IgG) using IgG-aptamer as the bioreceptor. The operation principle is attributed to the electrostatic gating effect of the positively charged IgG molecules that are absorbed on the graphene channel which can modulates the doping level of graphene and cause the negative shifts of the transfer curves. Negative shift of the transfer curve of the EGGFET biosensors was observed upon IgG adsorption and the gate voltage with the minimum conductivity (V_{Dirac}) is used for the quantitative measurement of IgG concentration. The EGGFET biosensor is also capable of real-time measurement of IgG by monitoring the drain current at a fixed gate voltage. Continuous decrease of the drain current was observed as the IgG concentration increases,

which is in accordance with the negative shift of the transfer curves. The selectivity of the EGGFET biosensor is tested by measuring its response to possible interfering targets. This proof-of-concept study implies that the EGGFET biosensor is a feasible platform for the label-free detection of biomarkers.

One of the challenges for the applications of the EGGFET biosensors is the complexity of the physiological samples. In EGGFET biosensors, the graphene channels are directly exposed to the electrolytes, which makes it highly sensitive to the variations in the electrolytes matrices. We studied the impact of the electrolytes on the Dirac voltage of the EGGFET biosensors by varying the composition, the ionic strength and the pH. The response of the EGGFET biosensors is found to be susceptible to these variations which might lead to high uncertainty or even false results. We presented an EGGFET immunoassay which allows well regulation of the matrix effects. The performance of the EGGFET immunoassay is demonstrated by the detection of human IgG from serum based on spike-and-recovery tests. The detection range of the EGGFET immunoassay for IgG detection from serum is estimated to be around 2-50 nM with a coefficient of variation (CV) of less than 20% and the limit of detection is estimated to be 0.7 nM. The EGGFET immunoassay is label-free, easy to use and ready to be integrated with simple electrical measurement units and thus have a great potential as the next generation immunoassay techniques

In the end, we present a study on the device physics of the EGGFET biosensors, which is important for the design and improvement of the nanoelectronics devices. Different from the metal-oxide-semiconductor field effect transistors (MOSFET), the gate voltage is applied on the electrolyte and the electrical double layer (EDL) at the electrolyte-graphene interface serves as the gate dielectric in EGGFET. We studied the capacitance behavior of the electrolyte-graphene interface; the results suggest that the electrolyte-graphene interface exhibits a complex constant phase element (CPE)

behavior ($\frac{1}{Z} = Q_0(j\omega)^\alpha$) with both Q_0 and α varying as functions of the gate voltage. The EDL capacitance and the quantum capacitance are determined which allows us to extract the carrier density and mobility in graphene.

To improve the performance of the EGGFET biosensor and realize the practical applications, the device design of the EGGFET biosensor should be optimized. For example, SiO_2 is typically used as the substrate for the graphene channel; however, the charged impurities on the surface of SiO_2 can significantly reduce the carrier mobility in graphene by Coulomb scattering. This will cause the loss of the sensitivity of the EGGFET biosensors. Studies indicate that the scattering is much lower using hexagonal boron nitride (h-BN) as the substrate for graphene (**Figure 8.1**). Therefore, it would be promising to improve the performance of the EGGFET biosensors using h-BN as the substrate for the graphene channel.

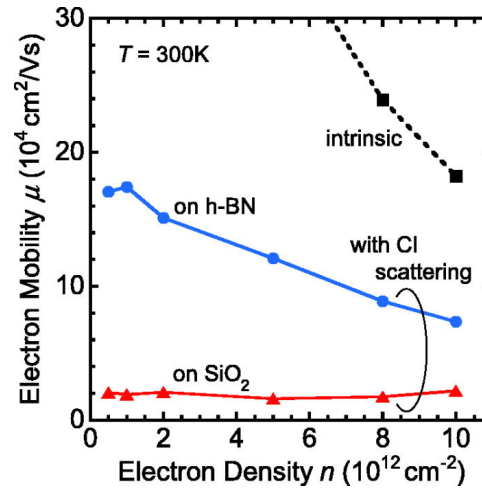


Figure 8.1 Computed electron mobility in graphene on different substrates.

In addition, the integration of the EGGFET biosensor with the fast-developing microfluidics might bring new opportunities to enable its practical application. Our lab developed an integrated lateral flow device (LFD) which applied the capillary forces with functionalized polymer-based microfluidics as a strategy to realize a portable, simplified, and self-powered LFD (**Figure 8.2**)

[134]. The LFD can realize the blood separation without external equipment for flow initiation and control. It would be interesting to integrate the developed EGGFET biosensors with the LFD, which is promising for point-of-care blood analysis. The developed EGGFET biosensor was embedded in the LFD and human IgG was detected directly from plasma (**Figure 8.3**).

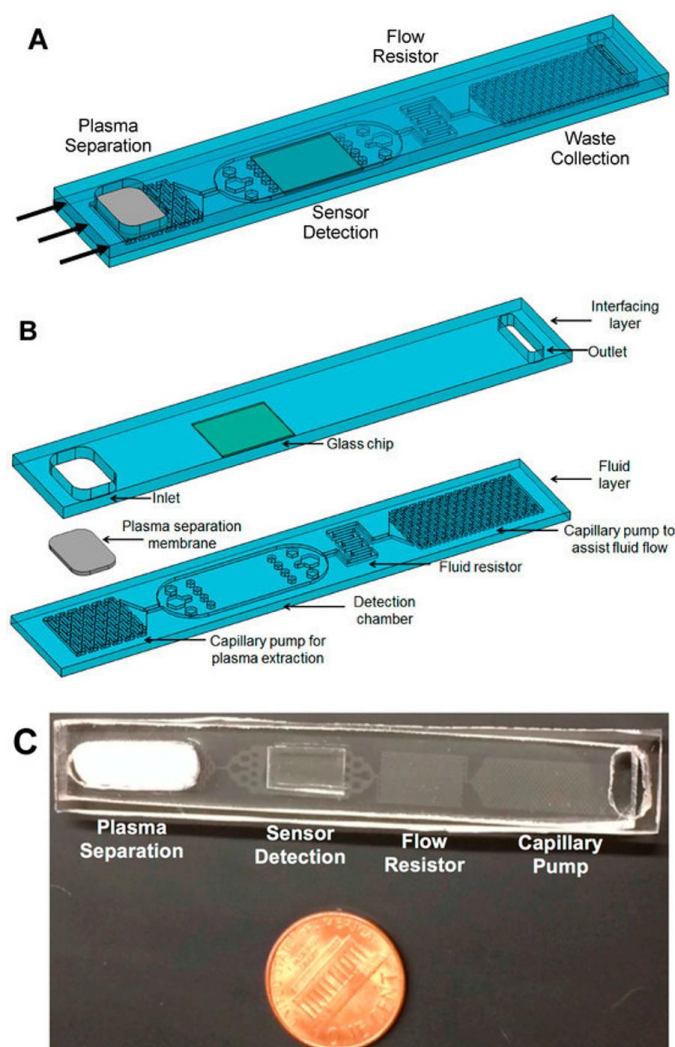


Figure 8.2 (A) Schematic diagram of the assembled lateral flow device (LFD) for blood separation and flow control. (B) Schematic diagram shows the interfacial layer and the microfluidics capillary pump. (C) A picture shows the fabricated LFD.

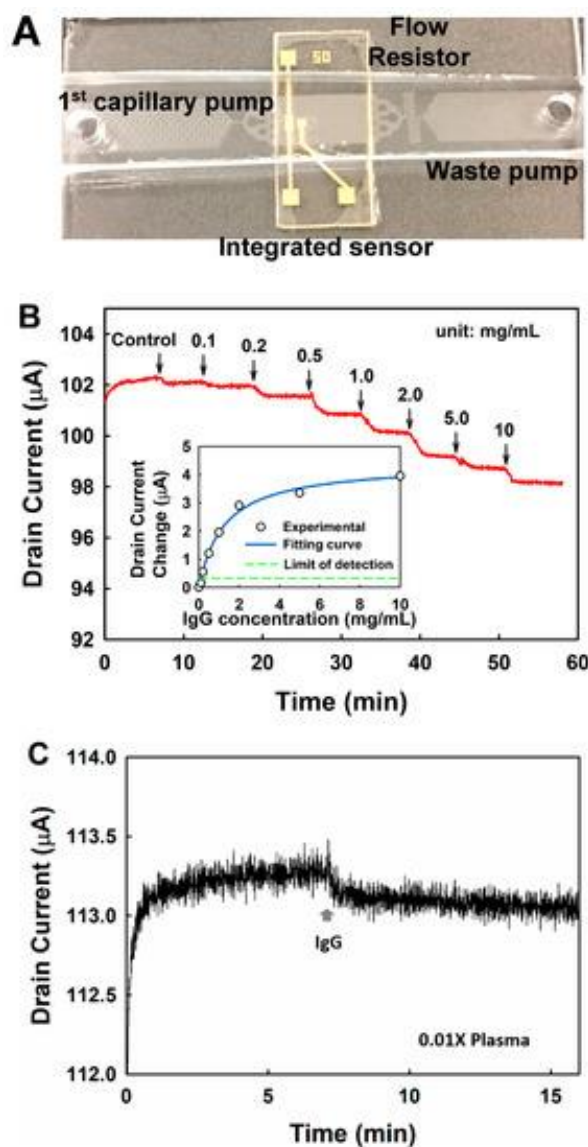


Figure 8.3 Real-time detection of IgG using nanoelectronics sensor integrated with the LFD. (A) A representative picture shows a fabricated LFD integrated with a nanoelectronics biosensor; (B) Continuous measurement of the drain current as responding to the addition of IgG with increasing concentrations; (C) The detection of IgG directly from human plasma.

Appendix

Appendix 1. Characterization of the functionalization of graphene

XPS and Raman spectroscopy were used for the characterization of the functionalization of graphene. The samples for characterization are glass slides with transferred CVD graphene on them and the characterizations were performed after each functionalization step. As shown in **Figure A1a**, the bare graphene exhibits a single C1s peak which indicates that cleaning graphene was obtained. After the immobilization of PBASE, new C1s peak at 289.5 eV and N1s peak at 402 eV arise which are attributed to the O-N-C=O in the *N*-Hydroxysuccinimide (NHS) group in the PBASE [238]. After conjugation with aptamer, strong C1s peaks at 288 eV and 286.5 eV and N1s peak at 400.5 eV arise which are common in DNA [239]. These peaks are intensified after blocking with BSA which are typically for protein functional groups [240].

A standard Raman spectrum was obtained after graphene transfer (**Figure A1b**). After PBASE immobilization, new peak arises just by the G peak on the right side which is assignable to the resonance introduced by the pyrene-graphene stacking [241]. The enhancement of the D peak at 1380 cm^{-1} is due to the disorder arising from π - π orbital hybridization [241]. After conjugation with aptamer, the two peaks are further intensified and a broad band appears at around 2900 cm^{-1} which is also reported by [242]. But the assignment of these peaks is still to be studied. Normally the broad band at around 2900 cm^{-1} is assigned to the aliphatic C-H stretching.

The transfer characteristics of the GFET were measured after each functionalization process. As shown in **Figure A1c**, significant positive shift was observed after functionalization and blocking due to the p-doping effect of pyrene group [243] and negatively charged BSA [244]. After incubating with $1\mu\text{M}$ IgG, the transfer curve was shifted negatively which suggests the positive charge of IgG and its n-doping effect on graphene.

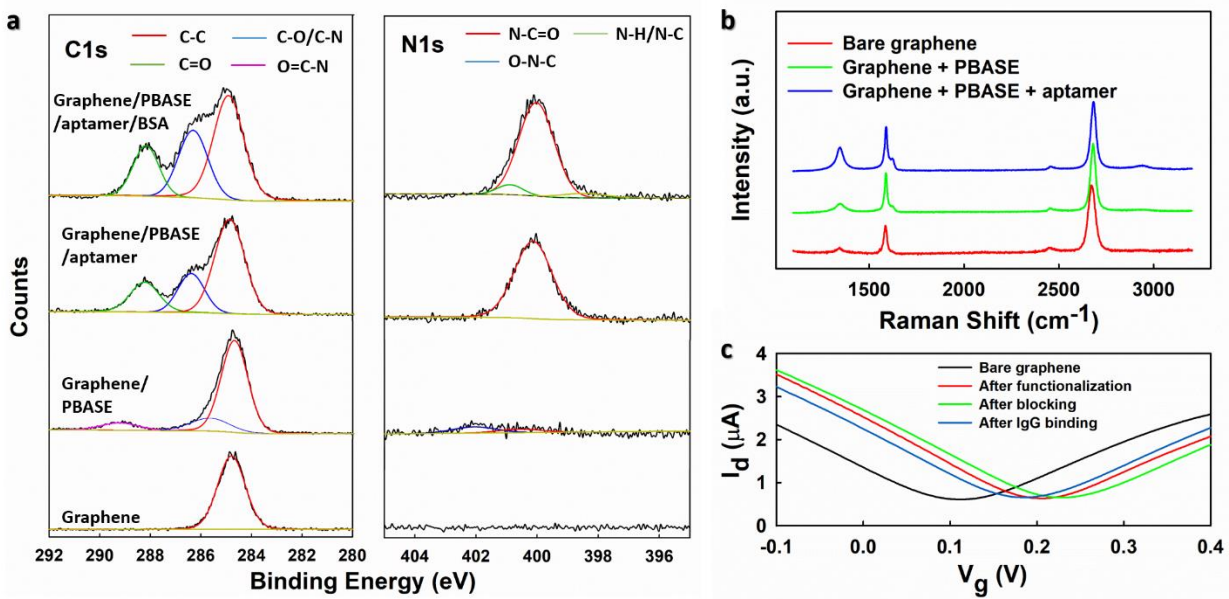


Figure A1. Characterization of graphene upon functionalization. (a) C1s and N1s XPS spectrum.

(b) Raman spectrum. (c) Transfer curves measured in 0.01X PBS with $V_{ds} = 0.01$ V.

Appendix.2 Determination of the Dirac Voltage

The determination of the V_{Dirac} from the transfer curves was conducted using Excel. The original transfer curve is shown in **Figure A2a**. The slope of the drain current I_d vs the gate voltage V_g was calculated using the SLOPE function (**Figure A2b**). The slope was calculated over 7 data points to reduce noise. Since the slope goes thru zero at the Dirac voltage, we plotted the V_g vs the slope for the data near the zero crossing and then fitted the small piece of data (20 points) with a straight line using the LINEST function (**Figure A2c**). The LINEST function provides the slope, intercept

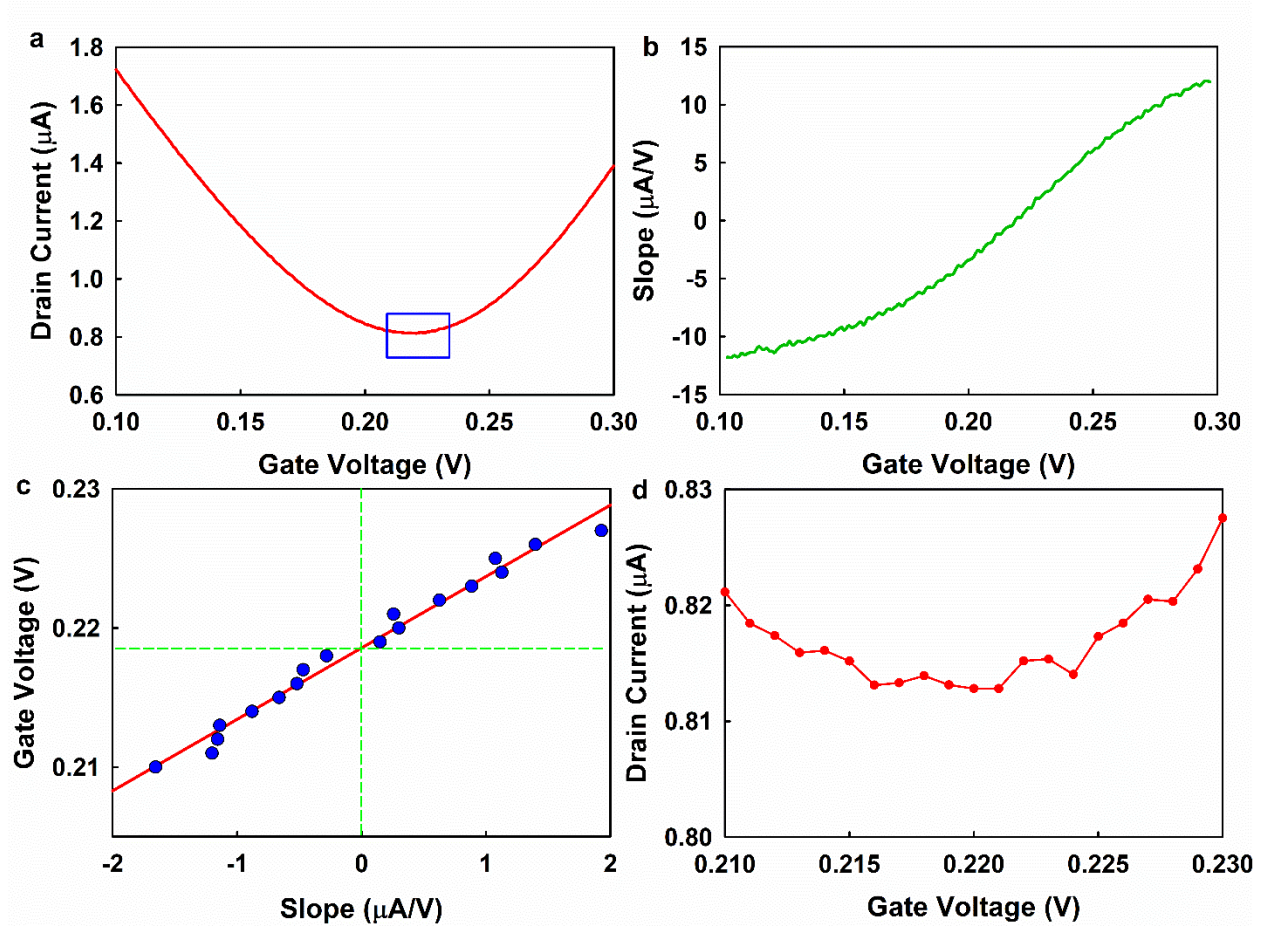


Figure A2 Derivation of the V_{Dirac} from the transfer curves. a) the original transfer curve (I_d vs V_g).

b) the slope of I_d vs V_g . c) V_g vs slope and the linear regression near. d) Enlarge view of the transfer curve as indicated by the box in a).

and their standard deviations. The intercept is the Dirac voltage and the standard deviation of the intercept is the uncertainty in the Dirac voltage.

The linear regression analysis allows more precise determination of the Dirac voltage with an uncertainty of less than 0.2 mV. The direct determination of the Dirac voltage by locating the minimum I_d generates uncertainty of several millivolt due to the noise in the measured drain current (as shown in **Figure A2d**). In the example as demonstrated in **Figure A2**, the Dirac voltage determined by linear regression of the V_g vs the slope is +0.21856 V with an uncertainty of 0.00017 V, while the V_g with the minimum I_d is +0.220 V.

Appendix 3. Optimization of the operation parameters

The hysteresis of the transfer curves of GFET upon reversal of the sweeping direction has been previously reported [245]. Our experiments indicate that the hysteresis also happens in EGGFET and have a direct impact on the detection precision for EGGFET based biosensors (**Figure A3a**). The hysteresis shows great dependence on the gate voltage sweeping rate and range. As shown in **Figure A3b**, the hysteresis can be effectively reduced at scan rate lower than 10 mV/s. All the transfer curves were obtained at gate voltage sweep rate of 10 mV/s unless otherwise specified.

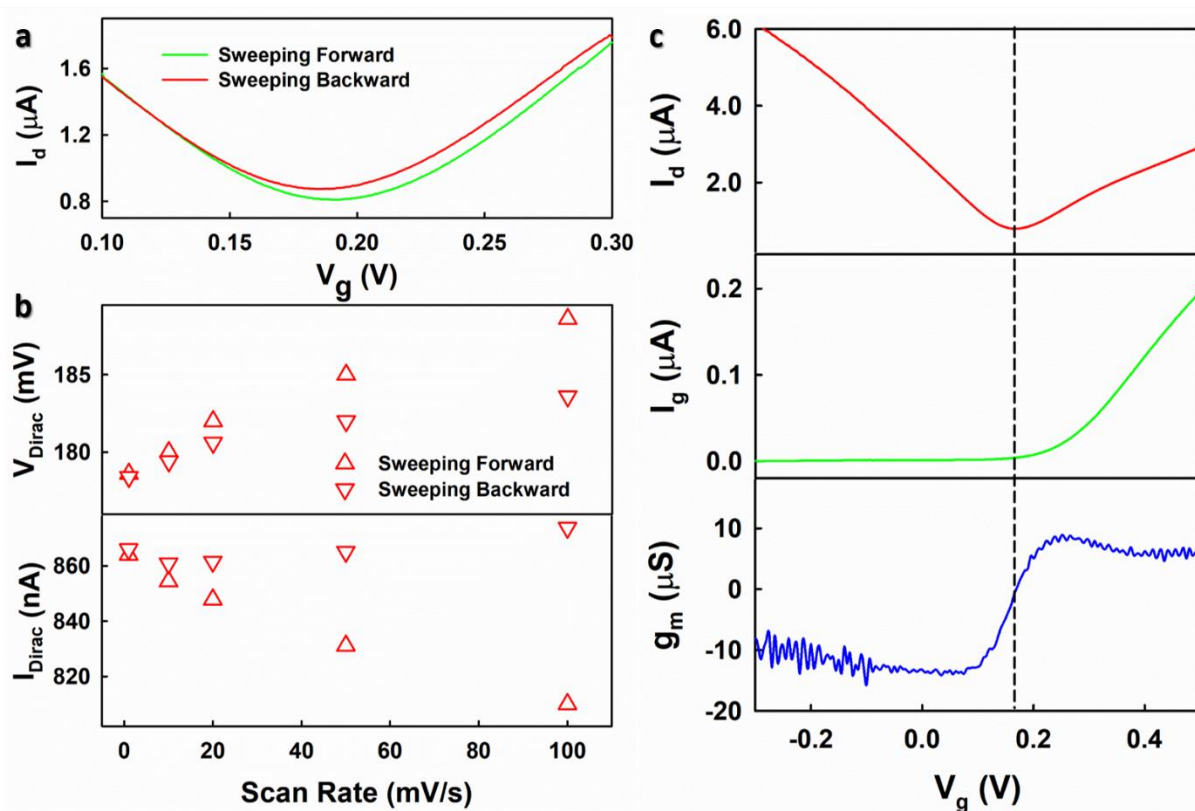


Figure A3 Optimization of the operation parameters of the EGGFET biosensor. a) Hysteresis of the forward and backward transfer curves measured with scan rate of 100 mV/s. b) The V_{Dirac} and I_{Dirac} (minimum drain current) of the forward and backward transfer curves at different scan rates. c) The transfer curve (I_d), leakage current (I_g) and transconductance (g_m) of the EGGFET measured in 0.01X PBS.

We propose the hysteresis is caused by the lagging of the ions movement in response to the gate voltage change.

To maximize the modulation capability of the V_g , V_{ds} was set to be 0.01 V which is smaller relative to the V_g sweeping range and yields I_d of several microamperes. The leakage current (I_g) was measured and leakage current was observed at $V_g > +0.2V$ (in 0.01X PBS with standard Ag/AgCl reference electrode) which is attributed to the electrochemical reduction of water (**Figure A3c**). To avoid the change of the electrolyte composition caused by water reduction, the V_g sweeping range should be kept away from the water reduction potential. Our devices work well in the range of $V_g < +0.5$ V; as shown in **Figure A3c**, even though the leakage current might cause some distortion of the transfer curves at high V_g , it won't have significant impact on the measurement of the V_{Dirac} . One of the key parameters characterizing the sensitivity of the FET biosensors is the transconductance (g_m). As shown in **Figure A3c**, the maximum g_m was obtained at around 0.1 V and 0.3 V. V_g of 0 V was used for the continuous measurement of I_d for the detection of IgG because the sensitivity of the biosensor is the highest near 0V (maximum g_m) and the biosensor gives the most stable response in this range.

Appendix 4. Determination of the detection range

As a bioanalytical device, the performance of the biosensor is normally characterized by the sensitivity, limit of detection (LOD), limit of quantification (LOQ), detection range, selectivity, reliability, etc. For the practical application of biosensors, especially for point of care biomedical applications, other factors must also be considered, such as production cost, operation difficulty, supportive facilities requirement, etc. In addition, the capabilities for real-time detection and multiple-target analysis are also anticipated for biosensors which distinguish them from traditional bioanalytical techniques. Among them, LOD, selectivity and detection range are referred to as the benchmarks for biosensors. Here the LOD and detection range are derived based on the duplicate measurement using the EGGFET immunosensors assay.

Determination of LOD

LOD is the lowest quantity of a substance that can be distinguished from the absence of the substance within a stated confidence limit [246]. There has often been a lack of criterion on the determination of LOD which leads to variable results [247]. Several methods have been used to define LOD, such as visual definition, calculation from the signal-to-noise ratio, calculation from the standard deviation of the blank, and calculation from the calibration line at low concentrations, etc. [247]. There is a preference to find the linear range of calibration curve and the LOD is determined by:

$$c_L = k\sigma/b \quad (\text{A-1})$$

where c_L is the LOD, σ is the standard deviation of the blank, b is the slope of the calibration curve. The magnitude of the k value is chosen so that a certain confidence level can be achieved. The IUPAC recommends that the k value should be 3 which corresponds to a confidence level of about 90% for limited measurements. However, our results indicate that the response of the EGGFET

biosensor is not linear to the concentration of the IgG but regulated by the Hill equation (**Figure A4**). Although at low concentration range, the calibration curve is approximately linear; yet the determination of the linear range would introduce ambiguity and complexity. As a result, the LOD is determined by calculating the IgG concentration which corresponds to ΔV_{Dirac} of 3 times of the standard deviation of the blank measurement:

$$c_L = \frac{3\sigma K_D}{\Delta V_{\text{Dirac}}^{\text{max}} - 3\sigma} \quad (\text{A-2})$$

For the measurement shown in **Figure A4**, the standard deviation of blank is around 0.4 mV, which yields a LOD of around 0.7 nM. This method finds the LOD based on the intrinsic fitting equation, avoids defining the linear range which introduces unnecessary ambiguity and should be applicable for the bioanalysis in which the equilibrium follows the Hill equation instead of linearity.

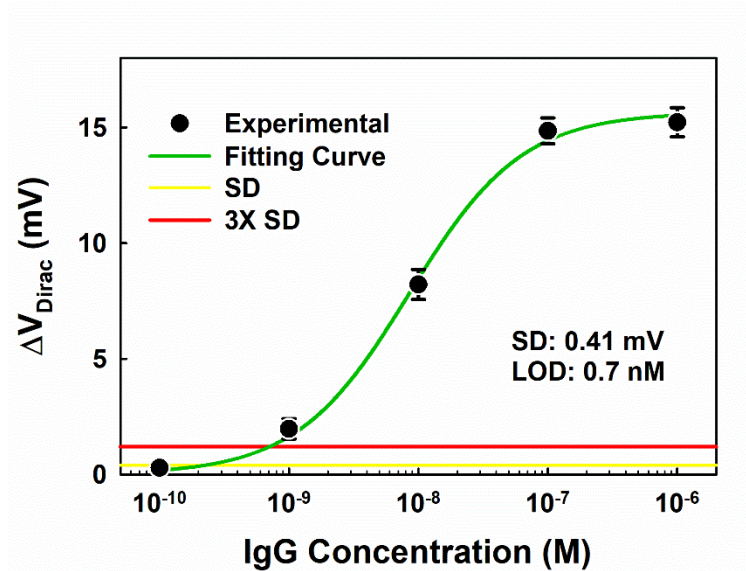


Figure A4 The determination of the LOD.

Detection range

The detection range is the concentration range that can be reliably measured by the biosensor. Similar with LOD, there is a lack of criterion for the determination of the detection range [248]. Here we determine the detection range of the EGGFET biosensors based on the relative standard deviation (RSD) of the concentration estimates. Firstly, the response is fitted using the Hill equation as shown in **Figure A5a**. The slope of the fitting curve is derived as shown in **Figure**

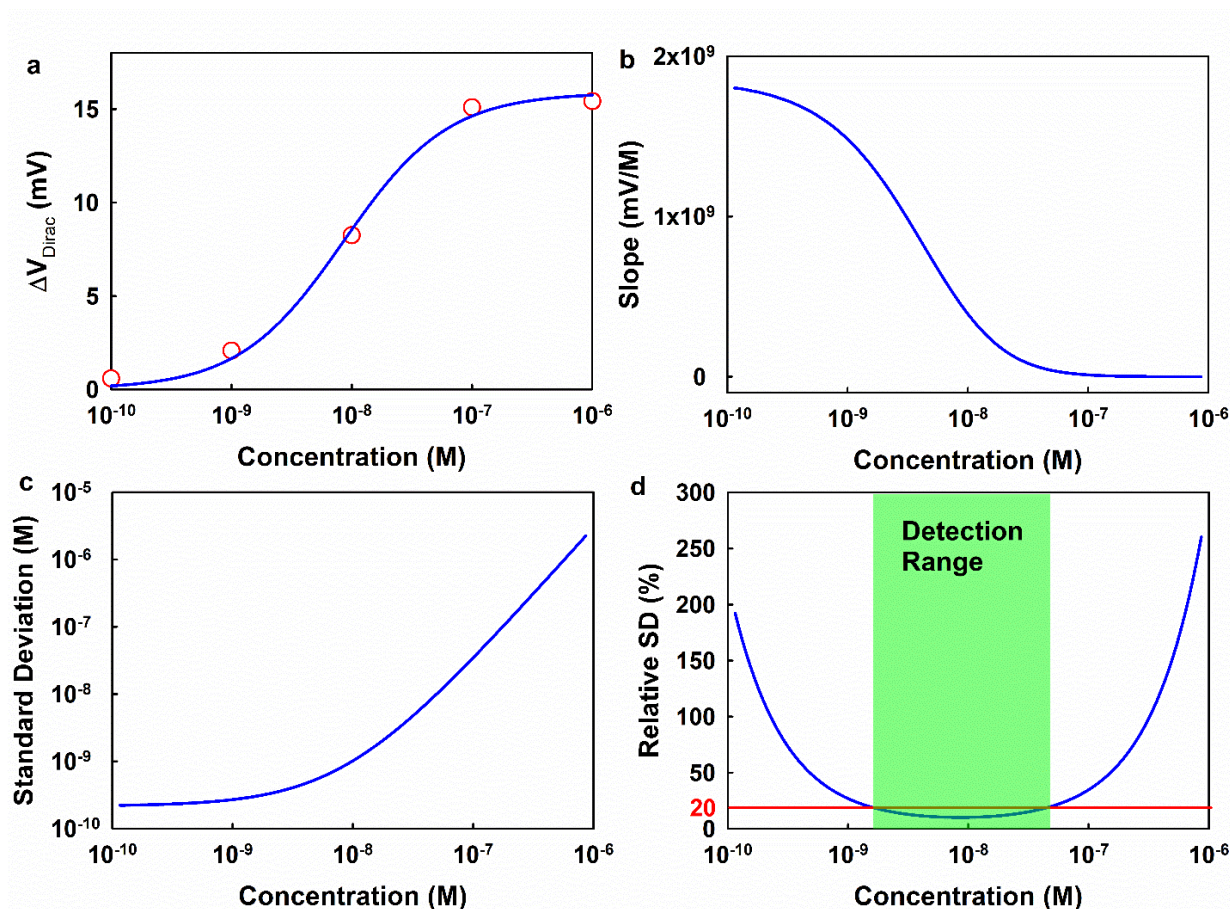


Figure A5 Determination of the detection range of the EGGFET biosensor for IgG detection. a) the fitting curve of the measurement results; b) the slope of the fitting curve; c) the SD of the concentration estimates; d) the RSD of the concentration estimated with respect to the concentration.

A5b. The standard deviation (SD) of the concentration estimated (**Figure A5c**) is calculated by dividing the SD of measurement (0.4 mV) by the slope. The RSD is the ratio of the SD to the estimated concentration and plotted in **Figure A5d**. For bioanalysis, such as ELISA, a coefficient of variance (CV) of 20% is empirically accepted. Therefore, the detection range of the EGGFET biosensor is determined to be around 2 ~ 50 nM which corresponds to $RSD < 20\%$ as shown in **Figure A5d**. This method determines the detection range based on the concentration estimates instead of the measurement reading, generates results with certain precision. It is applicable for bioanalysis that is regulated by nonlinear equation.

Appendix 5 Quantum capacitance of graphene

The dispersion of mobile π electrons in graphene in the first Brillouin Zone (BZ) is given by

$$E(k) = s\hbar v_F |k|$$

The linear density of states (DOS) in graphene is

$$\rho(E) = \frac{g_s g_v}{2\pi(\hbar v_F)^2} |E|$$

The carrier density can thereby be calculated as

$$n = \int_0^\infty \rho(E) f(E) dE$$

where $f(E)$ is the Fermi-Dirac distribution function given by $f(E) = (1 + \exp[(E - E_F)/kT])^{-1}$.

Using the dimensionless variables $u = E/kT$ and $\eta = E_F/kT$, the carrier density can be calculated as:

$$n = \frac{2}{\pi} \left(\frac{kT}{\hbar v_F} \right)^2 \mathcal{J}_1(+\eta)$$

and

$$p = \frac{2}{\pi} \left(\frac{kT}{\hbar v_F} \right)^2 \mathcal{J}_1(-\eta)$$

where $\mathcal{J}_j(\eta) = 1/\Gamma(j+1) \int_0^\infty u^j / (1 + e^{(u-\eta)}) du$ is the Fermi-Dirac integral with $j = 1$ and

$\Gamma(\dots)$ is the gamma function.

The intrinsic carrier concentration is given by

$$n_i = \frac{\pi}{6} \left(\frac{kT}{\hbar v_F} \right)^2$$

$$n_i = \frac{2}{\pi} \left(\frac{kT}{\hbar v_F} \right)^2 \mathcal{J}_1(0) = \frac{2}{\pi} \left(\frac{kT}{\hbar v_F} \right)^2 \cdot \frac{\pi^2}{12}$$

The carrier density can be rewritten as

$$n = n_i \mathcal{J}_1(+\eta) / \mathcal{J}_1(0)$$

and

$$p = n_i \mathcal{J}_1(-\eta) / \mathcal{J}_1(0)$$

Respectively.

The total carrier density can be written as

$$Q = e(p - n)$$

The quantum capacitance for graphene $C_Q = \partial Q / \partial V_{ch}$ can be calculated as

$$C_Q = \frac{2e^2 kT}{\pi(\hbar v_F)^2} \ln \left[2 \left(1 + \cosh \frac{eV_{ch}}{kT} \right) \right]$$

$$\begin{aligned} C_Q &= \frac{\partial Q}{\partial V_{ch}} \\ &= \frac{en_i}{\mathcal{J}_1(0)} \left[\frac{\partial \mathcal{J}_1\left(\frac{eV_{ch}}{kT}\right)}{\partial V_{ch}} - \frac{\partial \mathcal{J}_1\left(-\frac{eV_{ch}}{kT}\right)}{\partial V_{ch}} \right] \\ &= \frac{en_i}{\mathcal{J}_1(0)} \frac{e}{kT} \left[\mathcal{J}_0\left(\frac{eV_{ch}}{kT}\right) + \mathcal{J}_0\left(-\frac{eV_{ch}}{kT}\right) \right] \\ &= \frac{2e^2 kT}{\pi(\hbar v_F)^2} \left[\ln \left(1 + e^{\frac{eV_{ch}}{kT}} \right) + \ln \left(1 + e^{-\frac{eV_{ch}}{kT}} \right) \right] \\ &= \frac{2e^2 kT}{\pi(\hbar v_F)^2} \ln \left(2 + e^{\frac{eV_{ch}}{kT}} + e^{-\frac{eV_{ch}}{kT}} \right) \\ &= \frac{2e^2 kT}{\pi(\hbar v_F)^2} \ln \left[2 \left(1 + \cosh \frac{eV_{ch}}{kT} \right) \right] \end{aligned}$$

Under the condition $eV_{ch} \gg kT$, it reduces to

$$C_Q = \frac{2e^2 eV_{ch}}{\pi(\hbar v_F)^2}$$

Recall

$$\mathcal{J}_1(+\eta) = -Li_2(-e^\eta)$$

where $Li_2(-e^x)$ is the polylogarithm.

Note that

$$\eta = \frac{eV_{ch}}{kT}.$$

For $-1 \text{ V} < V_{ch} < +1 \text{ V}$, $-38.7 < \eta < 38.7$. In this range, $-Li_2(-e^\eta) \cong \eta^2/2$ (**Figure A6**).

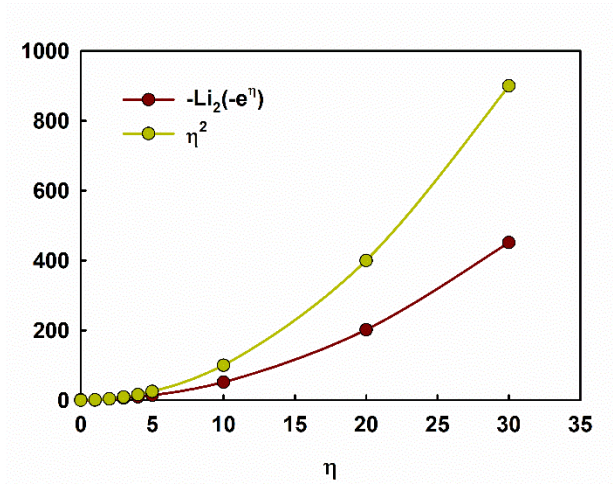


Figure A6 The plot showing $-Li_2(-e^\eta) \cong \eta^2/2$

Therefore,

$$\mathcal{J}_1(+\eta) \cong \frac{\eta^2}{2} = \frac{1}{2} \left(\frac{eV_{ch}}{kT} \right)^2$$

We obtain

$$n = \frac{2}{\pi} \left(\frac{kT}{\hbar v_F} \right)^2 \mathcal{J}_1(+\eta) \cong \left(\frac{eV_{ch}}{\sqrt{\pi} \hbar v_F} \right)^2$$

The quantum capacitance can thereby be written accordingly

$$C_Q = \frac{2e^2}{\pi \hbar v_F} \cdot \sqrt{n}$$

Considering the residue carriers induced by the imperfections in graphene,

$$C_Q = \frac{2e^2}{\pi \hbar v_F} \cdot \sqrt{n_g + n_{res}}$$

A customized Matlab code was used to fit the measurement results.

Input parameters:

data.mat	Experimental results
V_bias	$V_g - V_{Dirac}$, the gate potential shifted with respect to the Dirac point;
Ctotal_exp	C_{total} , measurement results of the total capacitance at the electrolyte-graphene interface

Output parameters:

fp	fitting parameters
fp(1) = C_{EDL} ;	
fp(2) = n_{res} ;	

```
%Code starts
```

```
save 'data.mat' % save the data for function @Ctotal use
fp0 = [0.06 1e16]; % set initial values for the fitting parameters.
[fp] = fminsearch(@Ctotal, fp0); % search minimum value of function @Ctotal.
disp(fp); % display fitting results.
```

```
function [ds]=Ctotal(fp)
load 'data.mat' % load the data
elech = 1.602e-19;
hbar = 1.055e-34;
vf = 1e6;
kB = 1.38e-23;
T = 300;
% save the data for function @Ctotal use
V_ch = abs(V_bias) - Ctotal_exp .* abs(V_bias) ./ fp(1); % calculate V_ch
for n = 1:datasize
eta(n,1) = elech/(kB*T)* V_ch(n,1);
polylogarithm(n,1)= polylog(2,-1*exp(eta(n,1)));
end
```

```
% calculate the polylogarithm and assign the results.
n_ind = ((kB * T / (hbar * vf)) .^2) * (2 / pi) .* (polylogarithm * -1);
% calculate the gate-induced carrier density.
Cq_fit = 2 * elech^2/(hbar*vf*sqrt(pi)).*sqrt(n_ind + fp(2));
% calculate the quantum capacitance.
Ctotal_fit = 1./(1/fp(1)+1./(Cq_fit));
% calculate the total interfacial capacitance.
ds = (Ctotal_fit - Ctotal_exp).^2;
ds = sum(ds);
% return the least square.
end
% Code end.
```

BIBLIOGRAPHY

- [1] Siddiqui M R, AlOthman Z A and Rahman N 2017 Analytical techniques in pharmaceutical analysis: A review *Arab. J. Chem.* **10** S1409–21
- [2] Van Emon J ., Gerlach C . and Bowman K 1998 Bioseparation and bioanalytical techniques in environmental monitoring *J. Chromatogr. B. Biomed. Sci. App.* **715** 211–28
- [3] Spooner N, Cape S, Hayes R, Kaur S, Kolman J, Lowes S, Summerfield S, Wilson A and Woolf E 2016 Issues facing the bioanalytical community: summary of round table discussions *Bioanalysis* **8** 2189–93
- [4] Bellan L M, Wu D and Langer R S 2011 Current trends in nanobiosensor technology *Wiley Interdiscip. Rev. Nanomed. Nanobiotechnol.* **3** 229–46
- [5] Monošík R, Stred'anský M and Šturdík E 2012 Biosensors - classification, characterization and new trends *Acta Chim. Slovaca* **5**
- [6] Turner A P F 2013 Biosensors: sense and sensibility *Chem. Soc. Rev.* **42** 3184
- [7] Bhalla N, Jolly P, Formisano N and Estrela P 2016 Introduction to biosensors *Essays Biochem.* **60** 1–8
- [8] Nič M, Jirát J, Košata B, Jenkins A and McNaught A 2009 biosensor *IUPAC Compendium of Chemical Terminology* (Research Triangle Park, NC: IUPAC)
- [9] Qlark L C J 1956 MONITOR AND CONTROL OF BLOOD AND TISSUE OXYGEN TENSIONS. *ASAIO J.* **2**

- [10] Mehrotra P 2016 Biosensors and their applications – A review *J. Oral Biol. Craniofacial Res.* **6** 153–9
- [11] Clark L C and Lyons C 2006 ELECTRODE SYSTEMS FOR CONTINUOUS MONITORING IN CARDIOVASCULAR SURGERY *Ann. N. Y. Acad. Sci.* **102** 29–45
- [12] Yoo E-H and Lee S-Y 2010 Glucose Biosensors: An Overview of Use in Clinical Practice *Sensors* **10** 4558–76
- [13] Teles F and Fonseca L 2008 Trends in DNA biosensors *Talanta* **77** 606–23
- [14] Johnson B N and Mutharasan R 2014 Biosensor-based microRNA detection: techniques, design, performance, and challenges *The Analyst* **139** 1576
- [15] Leca-Bouvier B and Blum L J 2005 Biosensors for Protein Detection: A Review *Anal. Lett.* **38** 1491–517
- [16] Lippa P B, Sokoll L J and Chan D W 2001 Immunosensors—principles and applications to clinical chemistry *Clin. Chim. Acta* **314** 1–26
- [17] Holzinger M, Le Goff A and Cosnier S 2014 Nanomaterials for biosensing applications: a review *Front. Chem.* **2**
- [18] Zhang A and Lieber C M 2016 Nano-Bioelectronics *Chem. Rev.* **116** 215–57
- [19] Liu S and Guo X 2012 Carbon nanomaterials field-effect-transistor-based biosensors *NPG Asia Mater.* **4** e23

- [20] Hu P, Zhang J, Li L, Wang Z, O'Neill W and Estrela P 2010 Carbon Nanostructure-Based Field-Effect Transistors for Label-Free Chemical/Biological Sensors *Sensors* **10** 5133–59
- [21] Zheng P, Li M, Jurevic R, Cushing S K, Liu Y and Wu N 2015 A gold nanohole array based surface-enhanced Raman scattering biosensor for detection of silver(I) and mercury(II) in human saliva *Nanoscale* **7** 11005–12
- [22] Rhiannan Forsyth, Anitha Devadoss and Owen Guy 2017 Graphene Field Effect Transistors for Biomedical Applications: Current Status and Future Prospects *Diagnostics* **7** 45
- [23] Schöning M J and Poghossian A 2002 Recent advances in biologically sensitive field-effect transistors (BioFETs) *The Analyst* **127** 1137–51
- [24] Park J, Nguyen H H, Woubit A and Kim M 2014 Applications of Field-Effect Transistor (FET)-Type Biosensors *Appl. Sci. Conver. Technol.* **23** 61–71
- [25] Bergveld P 1970 Development of an Ion-Sensitive Solid-State Device for Neurophysiological Measurements *IEEE Trans. Biomed. Eng.* **BME-17** 70–1
- [26] Chen K-I, Li B-R and Chen Y-T 2011 Silicon nanowire field-effect transistor-based biosensors for biomedical diagnosis and cellular recording investigation *Nano Today* **6** 131–54
- [27] Shen M-Y, Li B-R and Li Y-K 2014 Silicon nanowire field-effect-transistor based biosensors: From sensitive to ultra-sensitive *Biosens. Bioelectron.* **60** 101–11

- [28] Lu N, Gao A, Zhou H, Wang Y, Yang X, Wang Y and Li T 2016 Progress in Silicon Nanowire-Based Field-Effect Transistor Biosensors for Label-Free Detection of DNA *Chin. J. Chem.* **34** 308–16
- [29] Allen B L, Kichambare P D and Star A 2007 Carbon Nanotube Field-Effect-Transistor-Based Biosensors *Adv. Mater.* **19** 1439–51
- [30] Andronescu C and Schuhmann W 2017 Graphene-based field effect transistors as biosensors *Curr. Opin. Electrochem.*
- [31] Dankerl M, Hauf M V, Lippert A, Hess L H, Birner S, Sharp I D, Mahmood A, Mallet P, Veuillen J-Y, Stutzmann M and Garrido J A 2010 Graphene Solution-Gated Field-Effect Transistor Array for Sensing Applications *Adv. Funct. Mater.* **20** 3117–24
- [32] He Q, Wu S, Yin Z and Zhang H 2012 Graphene-based electronic sensors *Chem. Sci.* **3** 1764
- [33] Bhuyan M S A, Uddin M N, Islam M M, Bipasha F A and Hossain S S 2016 Synthesis of graphene *Int. Nano Lett.* **6** 65–83
- [34] Chen M, Haddon R C, Yan R and Bekyarova E 2017 Advances in transferring chemical vapour deposition graphene: a review *Mater Horiz*
- [35] Xu G, Zhang Y, Duan X, Balandin A A and Wang K L 2013 Variability Effects in Graphene: Challenges and Opportunities for Device Engineering and Applications *Proc. IEEE* **101** 1670–88

- [36] Castro Neto A H, Guinea F, Peres N M R, Novoselov K S and Geim A K 2009 The electronic properties of graphene *Rev. Mod. Phys.* **81** 109–62
- [37] Novoselov K S, Geim A K, Morozov S V, Jiang D, Katsnelson M I, Grigorieva I V, Dubonos S V and Firsov A A 2005 Two-dimensional gas of massless Dirac fermions in graphene *Nature* **438** 197–200
- [38] Baringhaus J, Ruan M, Edler F, Tejeda A, Sicot M, Taleb-Ibrahimi A, Li A-P, Jiang Z, Conrad E H, Berger C, Tegenkamp C and de Heer W A 2014 Exceptional ballistic transport in epitaxial graphene nanoribbons *Nature* **506** 349–54
- [39] Novoselov K S 2004 Electric Field Effect in Atomically Thin Carbon Films *Science* **306** 666–9
- [40] Chen J-H, Jang C, Xiao S, Ishigami M and Fuhrer M S 2008 Intrinsic and extrinsic performance limits of graphene devices on SiO₂ *Nat. Nanotechnol.* **3** 206–9
- [41] Kuzmenko A B, van Heumen E, Carbone F and van der Marel D 2008 Universal Optical Conductance of Graphite *Phys. Rev. Lett.* **100**
- [42] Lee C, Wei X, Kysar J W and Hone J 2008 Measurement of the Elastic Properties and Intrinsic Strength of Monolayer Graphene *Science* **321** 385–8
- [43] Wallace P R 1947 The Band Theory of Graphite *Phys. Rev.* **71** 622–34
- [44] Viculis L M 2003 A Chemical Route to Carbon Nanoscrolls *Science* **299** 1361–1361
- [45] Geim A K and Novoselov K S 2007 The rise of graphene *Nat. Mater.* **6** 183–91

- [46] Yi M and Shen Z 2015 A review on mechanical exfoliation for the scalable production of graphene *J Mater Chem A* **3** 11700–15
- [47] Huang Y, Sutter E, Shi N N, Zheng J, Yang T, Englund D, Gao H-J and Sutter P 2015 Reliable Exfoliation of Large-Area High-Quality Flakes of Graphene and Other Two-Dimensional Materials *ACS Nano* **9** 10612–20
- [48] Goler S, Piazza V, Roddaro S, Pellegrini V, Beltram F and Pingue P 2011 Self-assembly and electron-beam-induced direct etching of suspended graphene nanostructures *J. Appl. Phys.* **110** 064308
- [49] Hernandez Y, Nicolosi V, Lotya M, Blighe F M, Sun Z, De S, McGovern I T, Holland B, Byrne M, Gun'Ko Y K, Boland J J, Niraj P, Duesberg G, Krishnamurthy S, Goodhue R, Hutchison J, Scardaci V, Ferrari A C and Coleman J N 2008 High-yield production of graphene by liquid-phase exfoliation of graphite *Nat. Nanotechnol.* **3** 563–8
- [50] Knieke C, Berger A, Voigt M, Taylor R N K, Röhl J and Peukert W 2010 Scalable production of graphene sheets by mechanical delamination *Carbon* **48** 3196–204
- [51] Yu Q, Lian J, Siriponglert S, Li H, Chen Y P and Pei S-S 2008 Graphene segregated on Ni surfaces and transferred to insulators *Appl. Phys. Lett.* **93** 113103
- [52] Li X, Cai W, An J, Kim S, Nah J, Yang D, Piner R, Velamakanni A, Jung I, Tutuc E, Banerjee S K, Colombo L and Ruoff R S 2009 Large-Area Synthesis of High-Quality and Uniform Graphene Films on Copper Foils *Science* **324** 1312–4

- [53] Zhang Y, Zhang L and Zhou C 2013 Review of Chemical Vapor Deposition of Graphene and Related Applications *Acc. Chem. Res.* **46** 2329–39
- [54] Muñoz R and Gómez-Aleixandre C 2013 Review of CVD Synthesis of Graphene: Review of CVD Synthesis of Graphene *Chem. Vap. Depos.* **19** 297–322
- [55] Bae S, Kim H, Lee Y, Xu X, Park J-S, Zheng Y, Balakrishnan J, Lei T, Ri Kim H, Song Y I, Kim Y-J, Kim K S, Özyilmaz B, Ahn J-H, Hong B H and Iijima S 2010 Roll-to-roll production of 30-inch graphene films for transparent electrodes *Nat. Nanotechnol.* **5** 574–8
- [56] Yan Z, Peng Z and Tour J M 2014 Chemical Vapor Deposition of Graphene Single Crystals *Acc. Chem. Res.* **47** 1327–37
- [57] Chen C-C, Kuo C-J, Liao C-D, Chang C-F, Tseng C-A, Liu C-R and Chen Y-T 2015 Growth of Large-Area Graphene Single Crystals in Confined Reaction Space with Diffusion-Driven Chemical Vapor Deposition *Chem. Mater.* **27** 6249–58
- [58] Song Y, Pan D, Cheng Y, Wang P, Zhao P and Wang H 2015 Growth of large graphene single crystal inside a restricted chamber by chemical vapor deposition *Carbon* **95** 1027–32
- [59] Miseikis V, Convertino D, Mishra N, Gemmi M, Mashoff T, Heun S, Haghighian N, Bisio F, Canepa M, Piazza V and Coletti C 2015 Rapid CVD growth of millimetre-sized single crystal graphene using a cold-wall reactor *2D Mater.* **2** 014006
- [60] Geng D, Wang H and Yu G 2015 Graphene Single Crystals: Size and Morphology Engineering *Adv. Mater.* **27** 2821–37

- [61] Xu X, Zhang Z, Dong J, Yi D, Niu J, Wu M, Lin L, Yin R, Li M, Zhou J, Wang S, Sun J, Duan X, Gao P, Jiang Y, Wu X, Peng H, Ruoff R S, Liu Z, Yu D, Wang E, Ding F and Liu K 2017 Ultrafast epitaxial growth of metre-sized single-crystal graphene on industrial Cu foil *Sci. Bull.* **62** 1074–80
- [62] Li X, Zhu Y, Cai W, Borysiak M, Han B, Chen D, Piner R D, Colombo L and Ruoff R S 2009 Transfer of Large-Area Graphene Films for High-Performance Transparent Conductive Electrodes *Nano Lett.* **9** 4359–63
- [63] Kang J, Shin D, Bae S and Hong B H 2012 Graphene transfer: key for applications *Nanoscale* **4** 5527
- [64] Reina A, Son H, Jiao L, Fan B, Dresselhaus M S, Liu Z and Kong J 2008 Transferring and Identification of Single- and Few-Layer Graphene on Arbitrary Substrates *J. Phys. Chem. C* **112** 17741–4
- [65] Sun J, Finklea H O and Liu Y 2017 Characterization and electrolytic cleaning of poly(methyl methacrylate) residues on transferred chemical vapor deposited graphene *Nanotechnology* **28** 125703
- [66] Liang X, Sperling B A, Calizo I, Cheng G, Hacker C A, Zhang Q, Obeng Y, Yan K, Peng H, Li Q, Zhu X, Yuan H, Hight Walker A R, Liu Z, Peng L and Richter C A 2011 Toward Clean and Crackless Transfer of Graphene *ACS Nano* **5** 9144–53
- [67] Her M, Beams R and Novotny L 2013 Graphene transfer with reduced residue *Phys. Lett. A* **377** 1455–8

- [68] Jia K, Luo J, Hu R, Zhan J, Cao H, Su Y, Zhu H, Xie L, Zhao C, Chen D and Ye T 2016 Evaluation of PMMA Residues as a Function of Baking Temperature and a Graphene Heat-Free-Transfer Process to Reduce Them *ECS J. Solid State Sci. Technol.* **5** P138–41
- [69] Shivaraman S, Barton R A, Yu X, Alden J, Herman L, Chandrashekhara M, Park J, McEuen P L, Parpia J M, Craighead H G and Spencer M G 2009 Free-Standing Epitaxial Graphene *Nano Lett.* **9** 3100–5
- [70] Aristov V Y, Urbanik G, Kummer K, Vyalikh D V, Molodtsova O V, Preobrajenski A B, Zakharov A A, Hess C, Hänke T, Büchner B, Vobornik I, Fujii J, Panaccione G, Ossipyan Y A and Knupfer M 2010 Graphene Synthesis on Cubic SiC/Si Wafers. Perspectives for Mass Production of Graphene-Based Electronic Devices *Nano Lett.* **10** 992–5
- [71] Yazdi G, Iakimov T and Yakimova R 2016 Epitaxial Graphene on SiC: A Review of Growth and Characterization *Crystals* **6** 53
- [72] Kumar P V, Bardhan N M, Chen G-Y, Li Z, Belcher A M and Grossman J C 2016 New insights into the thermal reduction of graphene oxide: Impact of oxygen clustering *Carbon* **100** 90–8
- [73] Park S, An J, Potts J R, Velamakanni A, Murali S and Ruoff R S 2011 Hydrazine-reduction of graphite- and graphene oxide *Carbon* **49** 3019–23
- [74] Shao Y, Wang J, Engelhard M, Wang C and Lin Y 2010 Facile and controllable electrochemical reduction of graphene oxide and its applications *J Mater Chem* **20** 743–8

- [75] Saini D 2016 Synthesis and functionalization of graphene and application in electrochemical biosensing *Nanotechnol. Rev.* **5**
- [76] Boukhvalov D W and Katsnelson M I 2009 Chemical functionalization of graphene *J. Phys. Condens. Matter* **21** 344205
- [77] Georgakilas V, Otyepka M, Bourlinos A B, Chandra V, Kim N, Kemp K C, Hobza P, Zboril R and Kim K S 2012 Functionalization of Graphene: Covalent and Non-Covalent Approaches, Derivatives and Applications *Chem. Rev.* **112** 6156–214
- [78] Wang Y, Li Z, Wang J, Li J and Lin Y 2011 Graphene and graphene oxide: biofunctionalization and applications in biotechnology *Trends Biotechnol.* **29** 205–12
- [79] Anon 2016 Nanobiosensors: Next Generation Point-of-Care Biomedical Devices for Personalized Diagnosis *J. Anal. Bioanal. Tech.* **7**
- [80] Mohanty N and Berry V 2008 Graphene-Based Single-Bacterium Resolution Biodevice and DNA Transistor: Interfacing Graphene Derivatives with Nanoscale and Microscale Biocomponents *Nano Lett.* **8** 4469–76
- [81] Drummond T G, Hill M G and Barton J K 2003 Electrochemical DNA sensors *Nat. Biotechnol.* **21** 1192–9
- [82] Ley R E, Turnbaugh P J, Klein S and Gordon J I 2006 Microbial ecology: Human gut microbes associated with obesity *Nature* **444** 1022–3

- [83] Dong X, Shi Y, Huang W, Chen P and Li L-J 2010 Electrical Detection of DNA Hybridization with Single-Base Specificity Using Transistors Based on CVD-Grown Graphene Sheets *Adv. Mater.* **22** 1649–53
- [84] Chen T-Y, Loan P T K, Hsu C-L, Lee Y-H, Tse-Wei Wang J, Wei K-H, Lin C-T and Li L-J 2013 Label-free detection of DNA hybridization using transistors based on CVD grown graphene *Biosens. Bioelectron.* **41** 103–9
- [85] Lin C-T, Loan P T K, Chen T-Y, Liu K-K, Chen C-H, Wei K-H and Li L-J 2013 Label-Free Electrical Detection of DNA Hybridization on Graphene using Hall Effect Measurements: Revisiting the Sensing Mechanism *Adv. Funct. Mater.* **23** 2301–7
- [86] Cai B, Wang S, Huang L, Ning Y, Zhang Z and Zhang G-J 2014 Ultrasensitive Label-Free Detection of PNA–DNA Hybridization by Reduced Graphene Oxide Field-Effect Transistor Biosensor *ACS Nano* **8** 2632–8
- [87] Zheng C, Huang L, Zhang H, Sun Z, Zhang Z and Zhang G-J 2015 Fabrication of Ultrasensitive Field-Effect Transistor DNA Biosensors by a Directional Transfer Technique Based on CVD-Grown Graphene *ACS Appl. Mater. Interfaces* **7** 16953–9
- [88] Xu G, Abbott J, Qin L, Yeung K Y M, Song Y, Yoon H, Kong J and Ham D 2014 Electrophoretic and field-effect graphene for all-electrical DNA array technology *Nat. Commun.* **5** 4866
- [89] Ping J, Vishnubhotla R, Vrudhula A and Johnson A T C 2016 Scalable Production of High-Sensitivity, Label-Free DNA Biosensors Based on Back-Gated Graphene Field Effect Transistors *ACS Nano* **10** 8700–4

- [90] Saltzgaber G, Wojcik P M, Sharf T, Leyden M R, Wardini J L, Heist C A, Adenuga A A, Remcho V T and Minot E D 2013 Scalable graphene field-effect sensors for specific protein detection *Nanotechnology* **24** 355502
- [91] Pei X, Zhang B, Tang J, Liu B, Lai W and Tang D 2013 Sandwich-type immunosensors and immunoassays exploiting nanostructure labels: A review *Anal. Chim. Acta* **758** 1–18
- [92] Ohno Y, Maehashi K, Yamashiro Y and Matsumoto K 2009 Electrolyte-Gated Graphene Field-Effect Transistors for Detecting pH and Protein Adsorption *Nano Lett.* **9** 3318–22
- [93] Okamoto S, Ohno Y, Maehashi K, Inoue K and Matsumoto K 2012 Immunosensors Based on Graphene Field-Effect Transistors Fabricated Using Antigen-Binding Fragment *Jpn. J. Appl. Phys.* **51** 06FD08
- [94] Ohno Y, Maehashi K, Inoue K and Matsumoto K 2011 Label-Free Aptamer-Based Immunoglobulin Sensors Using Graphene Field-Effect Transistors *Jpn. J. Appl. Phys.* **50** 070120
- [95] Mao S, Lu G, Yu K, Bo Z and Chen J 2010 Specific Protein Detection Using Thermally Reduced Graphene Oxide Sheet Decorated with Gold Nanoparticle-Antibody Conjugates *Adv. Mater.* **22** 3521–6
- [96] Mao S, Yu K, Chang J, Steeber D A, Ocola L E and Chen J 2013 Direct Growth of Vertically-oriented Graphene for Field-Effect Transistor Biosensor *Sci. Rep.* **3**

- [97] He Q, Sudibya H G, Yin Z, Wu S, Li H, Boey F, Huang W, Chen P and Zhang H 2010 Centimeter-Long and Large-Scale Micropatterns of Reduced Graphene Oxide Films: Fabrication and Sensing Applications *ACS Nano* **4** 3201–8
- [98] Teixeira S, Burwell G, Castaing A, Gonzalez D, Conlan R S and Guy O J 2014 Epitaxial graphene immunosensor for human chorionic gonadotropin *Sens. Actuators B Chem.* **190** 723–9
- [99] Lei Y-M, Xiao M-M, Li Y-T, Xu L, Zhang H, Zhang Z-Y and Zhang G-J 2017 Detection of heart failure-related biomarker in whole blood with graphene field effect transistor biosensor *Biosens. Bioelectron.* **91** 1–7
- [100] Zhou L, Mao H, Wu C, Tang L, Wu Z, Sun H, Zhang H, Zhou H, Jia C, Jin Q, Chen X and Zhao J 2017 Label-free graphene biosensor targeting cancer molecules based on non-covalent modification *Biosens. Bioelectron.* **87** 701–7
- [101] Nehra A and Pal Singh K 2015 Current trends in nanomaterial embedded field effect transistor-based biosensor *Biosens. Bioelectron.* **74** 731–43
- [102] Huang Y, Dong X, Shi Y, Li C M, Li L-J and Chen P 2010 Nanoelectronic biosensors based on CVD grown graphene *Nanoscale* **2** 1485
- [103] Xie H, Li Y-T, Lei Y-M, Liu Y-L, Xiao M-M, Gao C, Pang D-W, Huang W-H, Zhang Z-Y and Zhang G-J 2016 Real-Time Monitoring of Nitric Oxide at Single-Cell Level with Porphyrin-Functionalized Graphene Field-Effect Transistor Biosensor *Anal. Chem.* **88** 11115–22

- [104] Jiang S, Cheng R, Wang X, Xue T, Liu Y, Nel A, Huang Y and Duan X 2013 Real-time electrical detection of nitric oxide in biological systems with sub-nanomolar sensitivity *Nat. Commun.* **4**
- [105] Huang Y, Dong X, Liu Y, Li L-J and Chen P 2011 Graphene-based biosensors for detection of bacteria and their metabolic activities *J. Mater. Chem.* **21** 12358
- [106] Kwon O S, Lee S H, Park S J, An J H, Song H S, Kim T, Oh J H, Bae J, Yoon H, Park T H and Jang J 2013 Large-Scale Graphene Micropattern Nano-biohybrids: High-Performance Transducers for FET-Type Flexible Fluidic HIV Immunoassays *Adv. Mater.* **25** 4177–85
- [107] Ang P K, Li A, Jaiswal M, Wang Y, Hou H W, Thong J T L, Lim C T and Loh K P 2011 Flow Sensing of Single Cell by Graphene Transistor in a Microfluidic Channel *Nano Lett.* **11** 5240–6
- [108] Hasegawa M, Hirayama Y, Ohno Y, Maehashi K and Matsumoto K 2014 Characterization of reduced graphene oxide field-effect transistor and its application to biosensor *Jpn. J. Appl. Phys.* **53** 05FD05
- [109] Rashid A D, Ruslinda A R, Fatin M F, Hashim U and Arshad M K 2016 Fabrication and characterization on reduced graphene oxide field effect transistor (RGOFET) based biosensor p 020076
- [110] Kim D-J, Sohn I Y, Jung J-H, Yoon O J, Lee N-E and Park J-S 2013 Reduced graphene oxide field-effect transistor for label-free femtomolar protein detection *Biosens. Bioelectron.* **41** 621–6

- [111] Chen T-Y, Loan P T K, Hsu C-L, Lee Y-H, Tse-Wei Wang J, Wei K-H, Lin C-T and Li L-J 2013 Label-free detection of DNA hybridization using transistors based on CVD grown graphene *Biosens. Bioelectron.* **41** 103–9
- [112] Tehrani Z, Burwell G, Azmi M A M, Castaing A, Rickman R, Almarashi J, Dunstan P, Beigi A M, Doak S H and Guy O J 2014 Generic epitaxial graphene biosensors for ultrasensitive detection of cancer risk biomarker *2D Mater.* **1** 025004
- [113] Ang P K, Chen W, Wee A T S and Loh K P 2008 Solution-Gated Epitaxial Graphene as pH Sensor *J. Am. Chem. Soc.* **130** 14392–3
- [114] Herbut I F 2009 Explanation for the isotropy of the Dirac cone in graphene *Phys. Rev. B* **79**
- [115] Asmar M M and Ulloa S E 2014 Spin-Orbit Interaction and Isotropic Electronic Transport in Graphene *Phys. Rev. Lett.* **112**
- [116] Stern E, Wagner R, Sigworth F J, Breaker R, Fahmy T M and Reed M A 2007 Importance of the Debye Screening Length on Nanowire Field Effect Transistor Sensors *Nano Lett.* **7** 3405–9
- [117] Reiner-Rozman C, Larisika M, Nowak C and Knoll W 2015 Graphene-based liquid-gated field effect transistor for biosensing: Theory and experiments *Biosens. Bioelectron.* **70** 21–7
- [118] Ohno Y, Maehashi K and Matsumoto K 2010 Label-Free Biosensors Based on Aptamer-Modified Graphene Field-Effect Transistors *J. Am. Chem. Soc.* **132** 18012–3

- [119] Ping J, Xi J, Saven J G, Liu R and Johnson A T C 2017 Quantifying the effect of ionic screening with protein-decorated graphene transistors *Biosens. Bioelectron.* **89** 689–92
- [120] Kulkarni G S and Zhong Z 2012 Detection beyond the Debye Screening Length in a High-Frequency Nanoelectronic Biosensor *Nano Lett.* **12** 719–23
- [121] Fu W, Feng L, Mayer D, Panaitov G, Kireev D, Offenhäusser A and Krause H-J 2016 Electrolyte-Gated Graphene Ambipolar Frequency Multipliers for Biochemical Sensing *Nano Lett.* **16** 2295–300
- [122] Gao N, Gao T, Yang X, Dai X, Zhou W, Zhang A and Lieber C M 2016 Specific detection of biomolecules in physiological solutions using graphene transistor biosensors *Proc. Natl. Acad. Sci.* **113** 14633–8
- [123] Gao N, Zhou W, Jiang X, Hong G, Fu T-M and Lieber C M 2015 General Strategy for Biodetection in High Ionic Strength Solutions Using Transistor-Based Nanoelectronic Sensors *Nano Lett.* **15** 2143–8
- [124] Chan C-Y, Yan F and Yang M 2016 Chemical vapor deposition grown graphene DNA field-effect transistor biosensor with gold nanoparticles signal amplification (IEEE) pp 290–3
- [125] Gutés A, Hsia B, Sussman A, Mickelson W, Zettl A, Carraro C and Maboudian R 2012 Graphene decoration with metal nanoparticles: Towards easy integration for sensing applications *Nanoscale* **4** 438–40

- [126] Tarasov A, Tsai M-Y, Flynn E M, Joiner C A, Taylor R C and Vogel E M 2015 Gold-coated graphene field-effect transistors for quantitative analysis of protein–antibody interactions *2D Mater.* **2** 044008
- [127] Sackmann E K, Fulton A L and Beebe D J 2014 The present and future role of microfluidics in biomedical research *Nature* **507** 181–9
- [128] Gravesen P, Branebjerg J and Jensen O S 1993 Microfluidics-a review *J. Micromechanics Microengineering* **3** 168–82
- [129] Choi K, Kim J-Y, Ahn J-H, Choi J-M, Im M and Choi Y-K 2012 Integration of field effect transistor-based biosensors with a digital microfluidic device for a lab-on-a-chip application *Lab. Chip* **12** 1533
- [130] Bouhadda I, De Sagazan O and Le Bihan F 2015 Field effect transistor with integrated microfluidic channel as pH sensor *Microsyst. Technol.* **21** 289–94
- [131] Lin C-L, Kang Y-W, Chang K-W, Chang W-H, Wang Y-L and Lee G-B 2014 AN integrated microfluidic system using field-effect transistors for CRP detection (IEEE) pp 150–3
- [132] Choi S, Goryll M, Sin L Y M, Wong P K and Chae J 2011 Microfluidic-based biosensors toward point-of-care detection of nucleic acids and proteins *Microfluid. Nanofluidics* **10** 231–47

- [133] Kumar S, Kumar S, Ali M A, Anand P, Agrawal V V, John R, Maji S and Malhotra B D 2013 Microfluidic-integrated biosensors: Prospects for point-of-care diagnostics *Biotechnol. J.* **8** 1267–79
- [134] Betancur V, Sun J, Wu N and Liu Y 2017 Integrated Lateral Flow Device for Flow Control with Blood Separation and Biosensing *Micromachines* **8** 367
- [135] Stern E, Vacic A, Rajan N K, Criscione J M, Park J, Ilic B R, Mooney D J, Reed M A and Fahmy T M 2010 Label-free biomarker detection from whole blood *Nat. Nanotechnol.* **5** 138–42
- [136] Lin Y-C, Lu C-C, Yeh C-H, Jin C, Suenaga K and Chiu P-W 2012 Graphene Annealing: How Clean Can It Be? *Nano Lett.* **12** 414–9
- [137] Borin Barin G, Song Y, de Fátima Gimenez I, Souza Filho A G, Barreto L S and Kong J 2015 Optimized graphene transfer: Influence of polymethylmethacrylate (PMMA) layer concentration and baking time on graphene final performance *Carbon* **84** 82–90
- [138] Chen Y, Gong X-L and Gai J-G 2016 Progress and Challenges in Transfer of Large-Area Graphene Films *Adv. Sci.* **3** 1500343
- [139] Pirkle A, Chan J, Venugopal A, Hinojos D, Magnuson C W, McDonnell S, Colombo L, Vogel E M, Ruoff R S and Wallace R M 2011 The effect of chemical residues on the physical and electrical properties of chemical vapor deposited graphene transferred to SiO₂ *Appl. Phys. Lett.* **99** 122108

- [140] Dan Y, Lu Y, Kybert N J, Luo Z and Johnson A T C 2009 Intrinsic Response of Graphene Vapor Sensors *Nano Lett.* **9** 1472–5
- [141] Wang Y, Zheng Y, Xu X, Dubuisson E, Bao Q, Lu J and Loh K P 2011 Electrochemical Delamination of CVD-Grown Graphene Film: Toward the Recyclable Use of Copper Catalyst *ACS Nano* **5** 9927–33
- [142] Cheng Z, Zhou Q, Wang C, Li Q, Wang C and Fang Y 2011 Toward Intrinsic Graphene Surfaces: A Systematic Study on Thermal Annealing and Wet-Chemical Treatment of SiO₂ - Supported Graphene Devices *Nano Lett.* **11** 767–71
- [143] Hong J, Park M K, Lee E J, Lee D, Hwang D S and Ryu S 2013 Origin of New Broad Raman D and G Peaks in Annealed Graphene *Sci. Rep.* **3**
- [144] Gong C, Floresca H C, Hinojos D, McDonnell S, Qin X, Hao Y, Jandhyala S, Mordì G, Kim J, Colombo L, Ruoff R S, Kim M J, Cho K, Wallace R M and Chabal Y J 2013 Rapid Selective Etching of PMMA Residues from Transferred Graphene by Carbon Dioxide *J. Phys. Chem. C* **117** 23000–8
- [145] Ferrari A C and Basko D M 2013 Raman spectroscopy as a versatile tool for studying the properties of graphene *Nat. Nanotechnol.* **8** 235–46
- [146] Ahn Y, Kim J, Ganorkar S, Kim Y-H and Kim S-I 2016 Thermal annealing of graphene to remove polymer residues *Mater. Express* **6** 69–76
- [147] Ferrari A C and Robertson J 2000 Interpretation of Raman spectra of disordered and amorphous carbon *Phys. Rev. B* **61** 14095–107

- [148] Holland B J and Hay J N 2001 The kinetics and mechanisms of the thermal degradation of poly(methyl methacrylate) studied by thermal analysis-Fourier transform infrared spectroscopy *Polymer* **42** 4825–35
- [149] Ferriol M, Gentilhomme A, Cochez M, Oget N and Mieloszynski J L 2003 Thermal degradation of poly(methyl methacrylate) (PMMA): modelling of DTG and TG curves *Polym. Degrad. Stab.* **79** 271–81
- [150] Choi W, Seo Y-S, Park J-Y, Kim K B, Jung J, Lee N, Seo Y and Hong S 2015 Effect of Annealing in Ar/H₂ Environment on Chemical Vapor Deposition-Grown Graphene Transferred With Poly (Methyl Methacrylate) *IEEE Trans. Nanotechnol.* **14** 70–4
- [151] Jang C W, Kim J H, Kim J M, Shin D H, Kim S and Choi S-H 2013 Rapid-thermal-annealing surface treatment for restoring the intrinsic properties of graphene field-effect transistors *Nanotechnology* **24** 405301
- [152] Jia Y, Gong X, Peng P, Wang Z, Tian Z, Ren L, Fu Y and Zhang H 2016 Toward High Carrier Mobility and Low Contact Resistance: Laser Cleaning of PMMA Residues on Graphene Surfaces *Nano-Micro Lett.* **8** 336–46
- [153] Lin Y-C, Jin C, Lee J-C, Jen S-F, Suenaga K and Chiu P-W 2011 Clean Transfer of Graphene for Isolation and Suspension *ACS Nano* **5** 2362–8
- [154] Cuthberston J W 1955 Electrolytic cleaning and polishing *J. Inst. Electr. Eng.* **1** 601–2

- [155] Wu Z, Chen H, Dong Y, Mao H, Sun J, Chen S, Craig V S J and Hu J 2008 Cleaning using nanobubbles: Defouling by electrochemical generation of bubbles *J. Colloid Interface Sci.* **328** 10–4
- [156] Sun X, Wu J, Chen Z, Su X and Hinds B J 2013 Fouling Characteristics and Electrochemical Recovery of Carbon Nanotube Membranes *Adv. Funct. Mater.* **23** 1500–6
- [157] Chen H, Mao H, Wu L, Zhang J, Dong Y, Wu Z and Hu J 2009 Defouling and cleaning using nanobubbles on stainless steel *Biofouling* **25** 353–7
- [158] Ni Z H, Wang H M, Luo Z Q, Wang Y Y, Yu T, Wu Y H and Shen Z X 2009 The effect of vacuum annealing on graphene *J. Raman Spectrosc.* **41** 479–83
- [159] Ostrowski J H J and Eaves J D 2014 The Tunable Hydrophobic Effect on Electrically Doped Graphene *J. Phys. Chem. B* **118** 530–6
- [160] Fan X F, Zheng W T, Chihai V, Shen Z X and Kuo J-L 2012 Interaction between graphene and the surface of SiO₂ *J. Phys. Condens. Matter* **24** 305004
- [161] Chen J-H, Ishigami M, Jang C, Hines D R, Fuhrer M S and Williams E D 2007 Printed Graphene Circuits *Adv. Mater.* **19** 3623–7
- [162] Tiberj A, Rubio-Roy M, Paillet M, Huntzinger J-R, Landois P, Mikolasek M, Contreras S, Sauvajol J-L, Dujardin E and Zahab A-A 2013 Reversible optical doping of graphene *Sci. Rep.* **3**
- [163] Cao P, Varghese J O, Xu K and Heath J R 2012 Visualizing Local Doping Effects of Individual Water Clusters on Gold(111)-Supported Graphene *Nano Lett.* **12** 1459–63

- [164] Ishikawa R, Bando M, Morimoto Y and Sandhu A 2011 Doping graphene films via chemically mediated charge transfer *Nanoscale Res. Lett.* **6** 111
- [165] Hess L H, Hauf M V, Seifert M, Speck F, Seyller T, Stutzmann M, Sharp I D and Garrido J A 2011 High-transconductance graphene solution-gated field effect transistors *Appl. Phys. Lett.* **99** 033503
- [166] Gitlin I, Carbeck J D and Whitesides G M 2006 Why Are Proteins Charged? Networks of Charge–Charge Interactions in Proteins Measured by Charge Ladders and Capillary Electrophoresis *Angew. Chem. Int. Ed.* **45** 3022–60
- [167] Linse S, Brodin P, Johansson C, Thulin E, Grundström T and Forsén S 1988 The role of protein surface charges in ion binding *Nature* **335** 651–2
- [168] Hedrick J L and Smith A J 1968 Size and charge isomer separation and estimation of molecular weights of proteins by disc gel electrophoresis *Arch. Biochem. Biophys.* **126** 155–64
- [169] Zhang P and Liu Y 2017 DC biased low-frequency insulating constriction dielectrophoresis for protein biomolecules concentration *Biofabrication* **9** 045003
- [170] Burton S . and Harding D R . 1998 Hydrophobic charge induction chromatography: salt independent protein adsorption and facile elution with aqueous buffers *J. Chromatogr. A* **814** 71–81
- [171] Tan Y H, Liu M, Nolting B, Go J G, Gervay-Hague J and Liu G 2008 A Nanoengineering Approach for Investigation and Regulation of Protein Immobilization *ACS Nano* **2** 2374–84

- [172] Khawli L A, Goswami S, Hutchinson R, Kwong Z W, Yang J, Wang X, Yao Z, Sreedhara A, Cano T, Tesar D B, Nijem I, Allison D E, Wong P Y, Kao Y-H, Quan C, Joshi A, Harris R J and Motchnik P 2010 Charge variants in IgG1: Isolation, characterization, in vitro binding properties and pharmacokinetics in rats *mAbs* **2** 613–24
- [173] Byon H R and Choi H C 2006 Network Single-Walled Carbon Nanotube-Field Effect Transistors (SWNT-FETs) with Increased Schottky Contact Area for Highly Sensitive Biosensor Applications *J. Am. Chem. Soc.* **128** 2188–9
- [174] Chen R J, Choi H C, Bangsaruntip S, Yenilmez E, Tang X, Wang Q, Chang Y-L and Dai H 2004 An Investigation of the Mechanisms of Electronic Sensing of Protein Adsorption on Carbon Nanotube Devices *J. Am. Chem. Soc.* **126** 1563–8
- [175] Tang X, Bansaruntip S, Nakayama N, Yenilmez E, Chang Y and Wang Q 2006 Carbon Nanotube DNA Sensor and Sensing Mechanism *Nano Lett.* **6** 1632–6
- [176] Gui E L, Li L-J, Zhang K, Xu Y, Dong X, Ho X, Lee P S, Kasim J, Shen Z X, Rogers J A and Mhaisalkar 2007 DNA Sensing by Field-Effect Transistors Based on Networks of Carbon Nanotubes *J. Am. Chem. Soc.* **129** 14427–32
- [177] Jianbo Sun and Yuxin Liu 2018 Matrix Effect Study and Immunoassay Detection Using Electrolyte-Gated Graphene Biosensor *Micromachines* **9** 142
- [178] Moriya R, Yamaguchi T, Inoue Y, Sata Y, Morikawa S, Masubuchi S and Machida T 2015 Influence of the density of states of graphene on the transport properties of graphene/MoS₂/metal vertical field-effect transistors *Appl. Phys. Lett.* **106** 223103

- [179] Kim B-K, Jeon E-K, Kim J-J and Lee J-O 2010 Positioning of the Fermi Level in Graphene Devices with Asymmetric Metal Electrodes *J. Nanomater.* **2010** 1–5
- [180] Xu H, Zhang Z, Xu H, Wang Z, Wang S and Peng L-M 2011 Top-Gated Graphene Field-Effect Transistors with High Normalized Transconductance and Designable Dirac Point Voltage *ACS Nano* **5** 5031–7
- [181] Rumyantsev S, Liu G, Shur M S, Potyrailo R A and Balandin A A 2012 Selective Gas Sensing with a Single Pristine Graphene Transistor *Nano Lett.* **12** 2294–8
- [182] Kim J P, Lee B Y, Hong S and Sim S J 2008 Ultrasensitive carbon nanotube-based biosensors using antibody-binding fragments *Anal. Biochem.* **381** 193–8
- [183] Zhang B, Li Q and Cui T 2012 Ultra-sensitive suspended graphene nanocomposite cancer sensors with strong suppression of electrical noise *Biosens. Bioelectron.* **31** 105–9
- [184] Hess L H, Jansen M, Maybeck V, Hauf M V, Seifert M, Stutzmann M, Sharp I D, Offenhäusser A and Garrido J A 2011 Graphene Transistor Arrays for Recording Action Potentials from Electrogenic Cells *Adv. Mater.* **23** 5045–9
- [185] Cheng Z, Hou J, Zhou Q, Li T, Li H, Yang L, Jiang K, Wang C, Li Y and Fang Y 2013 Sensitivity Limits and Scaling of Bioelectronic Graphene Transducers *Nano Lett.* **13** 2902–7
- [186] Cai B, Huang L, Zhang H, Sun Z, Zhang Z and Zhang G-J 2015 Gold nanoparticles-decorated graphene field-effect transistor biosensor for femtomolar MicroRNA detection *Biosens. Bioelectron.* **74** 329–34
- [187] Kellum J 2000 Determinants of blood pH in health and disease *Crit. Care* **4** 6–14

- [188] Heller I, Chatoor S, Männik J, Zevenbergen M A G, Dekker C and Lemay S G 2010 Influence of Electrolyte Composition on Liquid-Gated Carbon Nanotube and Graphene Transistors *J. Am. Chem. Soc.* **132** 17149–56
- [189] Williams C D, Dix J, Troisi A and Carbone P 2017 Effective Polarization in Pairwise Potentials at the Graphene–Electrolyte Interface *J. Phys. Chem. Lett.* **8** 703–8
- [190] Cole D J, Ang P K and Loh K P 2011 Ion Adsorption at the Graphene/Electrolyte Interface *J. Phys. Chem. Lett.* **2** 1799–803
- [191] Guinea F and Walet N 2016 Interaction between point charges, dipoles and graphene layers *ArXiv160508429 Cond-Mat* arXiv:1605.08429
- [192] Chen F, Xia J, Ferry D K and Tao N 2009 Dielectric Screening Enhanced Performance in Graphene FET *Nano Lett.* **9** 2571–4
- [193] Chen F, Xia J and Tao N 2009 Ionic Screening of Charged-Impurity Scattering in Graphene *Nano Lett.* **9** 1621–5
- [194] Xia J L, Chen F, Wiktor P, Ferry D K and Tao N J 2010 Effect of Top Dielectric Medium on Gate Capacitance of Graphene Field Effect Transistors: Implications in Mobility Measurements and Sensor Applications *Nano Lett.* **10** 5060–4
- [195] Kim C-H and Frisbie C D 2014 Determination of Quantum Capacitance and Band Filling Potential in Graphene Transistors with Dual Electrochemical and Field-Effect Gates *J. Phys. Chem. C* **118** 21160–9

- [196] Shinwari M W, Zhitomirsky D, Deen I A, Selvaganapathy P R, Deen M J and Landheer D 2010 Microfabricated Reference Electrodes and their Biosensing Applications *Sensors* **10** 1679–715
- [197] Ertürk G, Uzun L, Tümer M A, Say R and Denizli A 2011 Fab fragments imprinted SPR biosensor for real-time human immunoglobulin G detection *Biosens. Bioelectron.* **28** 97–104
- [198] Bakhmachuk A, Gorbatiuk O, Rachkov A, Dons'koi B, Khristosenko R, Ushenin I, Peshkova V and Soldatkin A 2017 Surface Plasmon Resonance Investigations of Bioselective Element Based on the Recombinant Protein A for Immunoglobulin Detection *Nanoscale Res. Lett.* **12**
- [199] Indyk H and Filonzi E 2003 Determination of immunoglobulin G in bovine colostrum and milk by direct biosensor SPR-immunoassay *J. AOAC Int.* **86** 386–93
- [200] Bonanno L M and DeLouise L A 2007 Whole blood optical biosensor *Biosens. Bioelectron.* **23** 444–8
- [201] Melnik E, Bruck R, Müellner P, Schlederer T, Hainberger R and Lämmerhofer M 2016 Human IgG detection in serum on polymer based Mach-Zehnder interferometric biosensors *J. Biophotonics* **9** 218–23
- [202] Schmitt K, Schirmer B, Hoffmann C, Brandenburg A and Meyrueis P 2007 Interferometric biosensor based on planar optical waveguide sensor chips for label-free detection of surface bound bioreactions *Biosens. Bioelectron.* **22** 2591–7

- [203] Ramachandran A, Wang S, Clarke J, Ja S J, Goad D, Wald L, Flood E M, Knobbe E, Hryniewicz J V, Chu S T, Gill D, Chen W, King O and Little B E 2008 A universal biosensing platform based on optical micro-ring resonators *Biosens. Bioelectron.* **23** 939–44
- [204] Tsugimura K, Ohnuki H, Endo H, Tsuya D and Izumi M 2016 Protein-G-based human immunoglobulin G biosensing by electrochemical impedance spectroscopy *Jpn. J. Appl. Phys.* **55** 02BE06
- [205] Qi H, Wang C and Cheng N 2010 Label-free electrochemical impedance spectroscopy biosensor for the determination of human immunoglobulin G *Microchim. Acta* **170** 33–8
- [206] Campanella L, Martini E, Pintore M and Tomassetti M 2009 Determination of Lactoferrin and Immunoglobulin G in Animal Milks by New Immunosensors *Sensors* **9** 2202–21
- [207] Mao S, Lu G, Yu K, Bo Z and Chen J 2010 Specific Protein Detection Using Thermally Reduced Graphene Oxide Sheet Decorated with Gold Nanoparticle-Antibody Conjugates *Adv. Mater.* **22** 3521–6
- [208] Xia J, Chen F, Li J and Tao N 2009 Measurement of the quantum capacitance of graphene *Nat. Nanotechnol.* **4** 505–9
- [209] Drieschner S, Guimerà A, Cortadella R G, Viana D, Makrygiannis E, Blaschke B M, Vieten J and Garrido J A 2017 Frequency response of electrolyte-gated graphene electrodes and transistors *J. Phys. Appl. Phys.* **50** 095304
- [210] Sharma P and Mišković Z L 2014 Capacitance of graphene in aqueous electrolytes: The effects of dielectric saturation of water and finite size of ions *Phys. Rev. B* **90**

- [211] Butt H-J, Graf K and Kappl M 2013 *Physics and chemistry of interfaces* (Weinheim, Germany: Wiley-VCH Verlag GmbH & Co. KGaA)
- [212] Mulder W H, Sluyters J H, Pajkossy T and Nyikos L 1990 Tafel current at fractal electrodes *J. Electroanal. Chem. Interfacial Electrochem.* **285** 103–15
- [213] Kim C-H, Pyun S-I and Kim J-H 2003 An investigation of the capacitance dispersion on the fractal carbon electrode with edge and basal orientations *Electrochimica Acta* **48** 3455–63
- [214] Schiller C A and Strunz W 2001 The evaluation of experimental dielectric data of barrier coatings by means of different models *Electrochimica Acta* **46** 3619–25
- [215] Jorcin J-B, Orazem M E, Pébère N and Tribollet B 2006 CPE analysis by local electrochemical impedance spectroscopy *Electrochimica Acta* **51** 1473–9
- [216] Barsoukov E and Macdonald J R 2005 *Impedance spectroscopy: theory, experiment, and applications* (Hoboken, N.J: Wiley-Interscience)
- [217] Fang T, Konar A, Xing H and Jena D 2007 Carrier statistics and quantum capacitance of graphene sheets and ribbons *Appl. Phys. Lett.* **91** 092109
- [218] Ji H, Zhao X, Qiao Z, Jung J, Zhu Y, Lu Y, Zhang L L, MacDonald A H and Ruoff R S 2014 Capacitance of carbon-based electrical double-layer capacitors *Nat. Commun.* **5**
- [219] Zhong J-H, Liu J-Y, Li Q, Li M-G, Zeng Z-C, Hu S, Wu D-Y, Cai W and Ren B 2013 Interfacial capacitance of graphene: Correlated differential capacitance and in situ electrochemical Raman spectroscopy study *Electrochimica Acta* **110** 754–61

- [220] Stoller M D, Magnuson C W, Zhu Y, Murali S, Suk J W, Piner R and Ruoff R S 2011 Interfacial capacitance of single layer graphene *Energy Environ. Sci.* **4** 4685
- [221] Charles Mackin, Elaine McVay and Tomás Palacios 2018 Frequency Response of Graphene Electrolyte-Gated Field-Effect Transistors *Sensors* **18** 494
- [222] Zhong H, Zhang Z, Xu H, Qiu C and Peng L-M 2015 Comparison of mobility extraction methods based on field-effect measurements for graphene *AIP Adv.* **5** 057136
- [223] Brown M A, Crosser M S, Leyden M R, Qi Y and Minot E D 2016 Measurement of high carrier mobility in graphene in an aqueous electrolyte environment *Appl. Phys. Lett.* **109** 093104
- [224] Dorgan V E, Bae M-H and Pop E 2010 Mobility and saturation velocity in graphene on SiO₂ *Appl. Phys. Lett.* **97** 082112
- [225] Venugopal A, Chan J, Li X, Magnuson C W, Kirk W P, Colombo L, Ruoff R S and Vogel E M 2011 Effective mobility of single-layer graphene transistors as a function of channel dimensions *J. Appl. Phys.* **109** 104511
- [226] Wang L, Wang W, Xu G, Ji Z, Lu N, Li L and Liu M 2016 Analytical carrier density and quantum capacitance for graphene *Appl. Phys. Lett.* **108** 013503
- [227] Kim S, Nah J, Jo I, Shahrjerdi D, Colombo L, Yao Z, Tutuc E and Banerjee S K 2009 Realization of a high mobility dual-gated graphene field-effect transistor with Al₂O₃ dielectric *Appl. Phys. Lett.* **94** 062107

- [228] Ratnakumar B V, Smart M C and Surampudi S 2002 Electrochemical impedance spectroscopy and its applications to lithium ion cells (IEEE) pp 273–7
- [229] Adam S, Hwang E H, Galitski V M and Das Sarma S 2007 A self-consistent theory for graphene transport *Proc. Natl. Acad. Sci.* **104** 18392–7
- [230] Galitski V M, Adam S and Das Sarma S 2007 Statistics of random voltage fluctuations and the low-density residual conductivity of graphene *Phys. Rev. B* **76**
- [231] Randin J-P and Yeager E 1972 Differential capacitance study on the basal plane of stress-annealed pyrolytic graphite *J. Electroanal. Chem. Interfacial Electrochem.* **36** 257–76
- [232] Cho S and Fuhrer M S 2008 Charge transport and inhomogeneity near the minimum conductivity point in graphene *Phys. Rev. B* **77**
- [233] Ando T, Fowler A B and Stern F 1982 Electronic properties of two-dimensional systems *Rev. Mod. Phys.* **54** 437–672
- [234] Hwang E H, Adam S and Sarma S D 2007 Carrier Transport in Two-Dimensional Graphene Layers *Phys. Rev. Lett.* **98**
- [235] Wang S, Jin Z, Muhammad A, Peng S, Huang X, Zhang D and Shi J 2016 Intrinsic carrier mobility extraction based on a new quasi-analytical model for graphene field-effect transistors *J. Phys. Appl. Phys.* **49** 425103
- [236] Newaz A K M, Puzyrev Y S, Wang B, Pantelides S T and Bolotin K I 2012 Probing charge scattering mechanisms in suspended graphene by varying its dielectric environment *Nat. Commun.* **3**

- [237] Hirai H, Tsuchiya H, Kamakura Y, Mori N and Ogawa M 2014 Electron mobility calculation for graphene on substrates *J. Appl. Phys.* **116** 083703
- [238] Yang M, Teeuwen R L M, Giesbers M, Baggerman J, Arafat A, de Wolf F A, van Hest J C M and Zuilhof H 2008 One-Step Photochemical Attachment of NHS-Terminated Monolayers onto Silicon Surfaces and Subsequent Functionalization *Langmuir* **24** 7931–8
- [239] Ptasińska S, Stypczyńska A, Nixon T, Mason N J, Klyachko D V and Sanche L 2008 X-ray induced damage in DNA monitored by X-ray photoelectron spectroscopy *J. Chem. Phys.* **129** 065102
- [240] Roguska A, Pisarek M, Andrzejczuk M, Dolata M, Lewandowska M and Janik-Czachor M 2011 Characterization of a calcium phosphate–TiO₂ nanotube composite layer for biomedical applications *Mater. Sci. Eng. C* **31** 906–14
- [241] Liu Y, Yuan L, Yang M, Zheng Y, Li L, Gao L, Nerngchamnong N, Nai C T, Sangeeth C S S, Feng Y P, Nijhuis C A and Loh K P 2014 Giant enhancement in vertical conductivity of stacked CVD graphene sheets by self-assembled molecular layers *Nat. Commun.* **5** 5461
- [242] Joseph D, Seo S, Williams D R and Geckeler K E 2014 Double-Stranded DNA-Graphene Hybrid: Preparation and Anti-Proliferative Activity *ACS Appl. Mater. Interfaces* **6** 3347–56
- [243] Dong X, Fu D, Fang W, Shi Y, Chen P and Li L-J 2009 Doping Single-Layer Graphene with Aromatic Molecules *Small* **5** 1422–6
- [244] Böhme U and Scheler U 2007 Effective charge of bovine serum albumin determined by electrophoresis NMR *Chem. Phys. Lett.* **435** 342–5

- [245] Wang H, Wu Y, Cong C, Shang J and Yu T 2010 Hysteresis of Electronic Transport in Graphene Transistors *ACS Nano* **4** 7221–8
- [246] MacDougall D, Crummett W B and et al. . 1980 Guidelines for data acquisition and data quality evaluation in environmental chemistry *Anal. Chem.* **52** 2242–9
- [247] Shrivastava A and Gupta V 2011 Methods for the determination of limit of detection and limit of quantitation of the analytical methods *Chron. Young Sci.* **2** 21
- [248] Hayashi Y, Matsuda R, Maitani T, Imai K, Nishimura W, Ito K and Maeda M 2004 Precision, Limit of Detection and Range of Quantitation in Competitive ELISA *Anal. Chem.* **76** 1295–301